From atom to edge:
The influence of a magnetic field on nanoscale systems

Jesper R. Moes

From atom to edge:
the influence of a magnetic field on nanoscale systems

Van atoom tot rand: De invloed van een magneetveld op nanoschaal systemen

(met een samenvatting in het Nederlands)

Proefschrift

ter verkrijging van de graad van doctor aan de
Universiteit Utrecht
op gezag van de
rector magnificus, prof. dr. H.R.B.M. Kummeling,
ingevolge het besluit van het college voor promoties
in het openbaar te verdedigen op

vrijdag 3 mei 2024 des ochtends te 10.15 uur

door

Jesper René Moes

geboren op 15 november 1991
te Zaanstad

Promotor:

Prof. dr. D.A.M. Vanmaekelbergh
Prof. dr. I. Swart

Beoordelingscommissie:

Prof. dr. F.M.F. de Groot
Prof. dr. W.K. Kegel
Prof. dr. P.M. Koenraad
Prof. dr. C. de Morais Smith
Dr. F.T. Rabouw

Contents

Chapter 1: Introduction

"The story so far: In the beginning the Universe was created. This has made a lot of people very angry and been widely regarded as a bad move."
– Douglas Addams, The restaurant at the end of the universe.

Chapter 1: Introduction

Magnetism might, for a lot of children, be the first contact with science and scientific experimentation. Finding bar magnets and discovering how the north and south pole attract each other but the same pole repulse one another is a fascinating discovery for many, especially since these forces are invisible to the naked eye. The continued fascination of the "invisible" inspires many fields in science, from dark matter which makes up about 27% of the universe to the behaviour of single electrons in different systems.[1–4]

In this work, different "invisible" systems are investigated, even though every project described in this thesis is invisible to the naked eye, the scanning tunnelling microscope (STM) is able to visualize, manipulate and investigate systems as small as single atoms.[5]

The STM does not use light to operate, rather it uses electrons travelling between the sample and an atomically sharp tip to probe a sample, similarly to a record player. The electrons travelling from a sample to the tip house a lot of information about the topology as well as the electronic properties of the material.[5] This combination is especially very potent to research atomically local effects with incredible electronic precision.[6–8]

Over the years, the capabilities of the STM have expanded to include low-temperature, ultrahigh vacuum, evaporation of particles on the sample and much more.[5,9,10] All of these additions allow for the research of the most fundamental physics and chemistry. An important possibility is to apply a perpendicular magnetic field to the sample by means of a superconducting vector magnet, leading to scientific research on high-temperature superconductors, topological insulators and more.[11–14]

Magnetism can influence the electrons in the sample measured in the STM by, for example, Zeeman splitting or Lorentz force. Research involving magnetism has been around for centuries and led to many inventions such as magnetic screwdrivers, undulators for synchrotrons and much more. Does this mean that this "invisible" force holds no more secrets for mankind? No, there are still many researchers trying to figure out how magnetism affects the world around us. Especially on the atomic scale there is plenty of scientific research focussed on the effect of magnetism on different materials.[15,16] In this work the capabilities of the Scanning Tunnelling Microscope are combined with the mysteries of magnetism to gain insight into the influence of a magnetic field on artificial atoms, colloidally synthesized two-dimensional (2D) topological insulators and dopants in semiconductors. These different projects display the versatility of scanning tunnelling microscopy, from answering question raised in fundamental science to investigating potential new materials for electronic and spintronic devices.

1.1 Outline of this thesis

In **chapter 2** of this thesis part of the theory behind magnetism will be discussed that will clarify the chapters in the second half of this thesis. The workings of the STM and how this machine can open up the route to analysing new physics shall also be touched upon.

Chapter 3 describes the electronic properties of colloidally synthesized bismuth selenide (Bi_2Se_3) nanoplatelets. Bi_2Se_3 is known to be a topological insulator with an insulating bulk but conducting states at the boundaries, STM is used to show these conducting topological states on crystals with different thickness. When the Bi_2Se_3 crystals are thin enough the top and bottom states hybridize leaving a 2D topological insulator with an insulating centre and topological states at the edges.

The robustness of these topological edge states is investigated in **chapter 4**. Three different topics are discussed. First, structural deformities are investigated in different nanoplatelets to prove the robustness of the edge state. Secondly, platelets are investigated which are adjacent to or stacked on top of another platelet, to determine if the states of different platelets have an effect on one another. Lastly, magnetism is introduced in the sample in two ways, applying a 5 Tesla perpendicular magnetic field and evaporating paramagnetic adsorbates. Theory dictates that the topological state is not robust to magnetism and should therefore break the edge state.

Chapter 5 describes, the ability of the STM to manipulate carbon-monoxide molecules on a copper surface. This technique is used to build circular and square artificial atoms. These atoms show excellent resemblance to real atoms showing the s- and p- orbital states. By applying a magnetic field it is attempted to split the peaks of these s- and p- orbitals due to the Zeeman effect and the Lorentz force.

The final chapter, **chapter 6**, describes the research on various dopants in gallium arsenide (GaAs). The electronic structure of Silicon and Boron dopants is investigated using scanning tunnelling spectroscopy. Zinc dopants are manipulated using the STM tip to determine the possibility to create artificial lattices. Lastly, the tunnelling probability between the STM tip and a GaAs sample is investigated under influence of a perpendicular magnetic field.

Bibliography

1. Parker, B. R. *Invisible matter and the fate of the universe.* (Springer US, 2013).

2. M. Jöge, F. Calculation of dark energy and dark matter. *Int. J. Phys. Astron.* **7**, (2019).

3. Bastiaans, K. M. *et al.* Imaging doubled shot noise in a Josephson scanning tunneling microscope. *Phys. Rev. B* **100**, 104506 (2019).

4. Ge, J.-F. et al. Single-electron charge transfer into putative Majorana and trivial modes in individual vortices. *Nat. Commun.* **14**, 3341 (2023).

5. Voigtländer, B. *Scanning probe microscopy: atomic force microscopy and scanning tunneling microscopy.* (Springer Berlin Heidelberg, 2015).

6. Gardenier, T. S. *et al.* p Orbital flat band and dirac cone in the electronic honeycomb lattice. *ACS Nano* **14**, 13638–13644 (2020).

7. Franchina Vergel, N. A. *et al.* Engineering a robust flat band in III–V semiconductor heterostructures. *Nano Lett.* **21**, 680–685 (2021).

8. Verstijnen, T. J. F., Tjeertes, D., Banfi, E. G., Zhuang, Q. & Koenraad, P. M. Atomic scale analysis of N dopants in InAs. *Phys. Rev. B* **108**, 045302 (2023).

9. Kamlapure, A. *et al.* A 350mK, 9T scanning tunneling microscope for the study of superconducting thin films on insulating substrates and single crystals. *Rev. Sci. Instrum.* **84**, 123905 (2013).

10. Meng, W., Guo, Y., Hou, Y. & Lu, Q. Atomic resolution scanning tunneling microscope imaging up to 27T in a water-cooled magnet. *Nano Res.* **8,** 3898–3904 (2015).

11. Fischer, Ø., Kugler, M., Maggio-Aprile, I., Berthod, C. & Renner, C. Scanning tunneling spectroscopy of high-temperature superconductors. *Rev. Mod. Phys.* **79,** 353–419 (2007).

12. Zhao, K. *et al.* Scanning tunneling microscopy studies of topological insulators. *J. Phys. Condens. Matter* **26**, 394003 (2014).

13. Dean, C. R. *et al.* Multicomponent fractional quantum Hall effect in graphene. *Nat. Phys.* **7**, 693–696 (2011).

14. Saarikoski, H., Harju, A., Puska, M. J. & Nieminen, R. M. Vortex clusters in quantum dots. *Phys. Rev. Lett.* **93**, 116802 (2004).

15. Fan, P. *et al.* Nanoscale Manipulation of wrinkle-pinned Vortices in Iron-based superconductors. *Nano Lett.* **23**, 4541–4547 (2023).

16. Huang, X. *et al.* Observation of two-dimensional type-II superconductivity in bulk 3R-TaSe$_2$ by scanning tunneling spectroscopy. *J. Phys. Chem. Lett.* **14**, 7235–7240 (2023).

Ch.
1

Chapter 2:
Theory

This chapter will describe the general concepts which are used throughout the thesis. Since every chapter will address a different project, every chapter will also have a theory section specific to those experiments and results. There are two common denominators throughout the thesis: scanning tunnelling microscopy and magnetism. The scanning tunnelling microscope and the ability to analyse the electronic landscape of materials with high electronic resolution using scanning tunnelling spectroscopy will be explained here. As well as the second cornerstone of this thesis, magnetism. Magnetism is however a very extensive field and therefore only small parts will be touched upon in this theoretical chapter.

"I would like you to know,
When you see the simple things,
To appreciate this life,
It's not too late to learn"
–Iron Maiden, Different world (2006)

2.1 Scanning tunnelling microscopy

In this chapter, we will briefly touch upon the different physics encountered in this dissertation. However, it is out of the scope of this thesis to give a complete explanation, therefore for more detailed information we refer to the following textbooks about quantum mechanics[1], scanning tunnelling microscopy[2] and magnetism.[3]

One of the first quantum mechanical phenomena taught in an elementary quantum mechanics course is electron tunnelling. Friedrich Hund was the first to notice this, in 1927, while working on a calculation of the ground state of a double well potential. His first paper on this topic, submitted in November 1926, focussed on an outer electron moving in an atomic potential with two or more minima separated by potential barriers which were impenetrable when considering classical mechanics.[4] This penetration of a potential barrier which can only be described using quantum mechanics led to the creation of a microscope with the ability to 'see' atoms, the scanning tunnelling microscope (STM).[5]

Figure 2.1 shows a schematic of how this tunnelling effect of electrons is used to perform microscopy. A bias voltage is applied between an atomically sharp metallic tip and a conductive substrate. Once the tip and substrate are in close proximity, roughly a nanometre distance, electrons from the tip can tunnel through the vacuum into the substrate or vice-versa depending on the sign of the applied bias voltage. Once the electrons start to tunnel, a current can be measured since the loop has been closed. This current is typically kept constant using a feedback loop while the tip is raster scanned over the surface. Typical tunnel current values are in the pico-ampere to nano-ampere range. The distance between the tip and substrate and the current are related via the following formula:

$$I = I_0 \cdot 10^{-\kappa * d} \tag{2.1}$$

with I is the tunnel current with I_0 a pre-factor, κ is the decay constant and d is the distance between tip and substrate.[2] The decay constant κ depends on the work function of the substrate and the tip. The value of the decay constant κ is typically 2Å^{-1} (depending on the tip material). Equation (2.1) can be intuitively understood: when there is a larger distance between tip and substrate, fewer electrons tunnel through the vacuum, leading to a lower current and vice versa. By employing the feedback loop and keeping the current constant, logically also the distance between tip and sample is kept constant. Therefore, when something changes on the substrate, for example when the tip scans over an adatom on the surface, the distance is decreased which would lead to an increase in tunnel current. The feedback loop reacts to this and will retract the tip. By recording the tip-height for every lateral position, one obtains a

topographic STM image of the surface. Equation (2.1) predicts that the tunnel current will vary by approximately one order of magnitude when the tip-sample distance changes by 1Å. When using a tip with an atomically sharp apex, it becomes possible to resolve individual atoms in the surface. This is the first function of an STM: scanning a surface and visualizing its atomic structure (including any atomic defects or dopants) as well as atoms deposited on top of the surface.
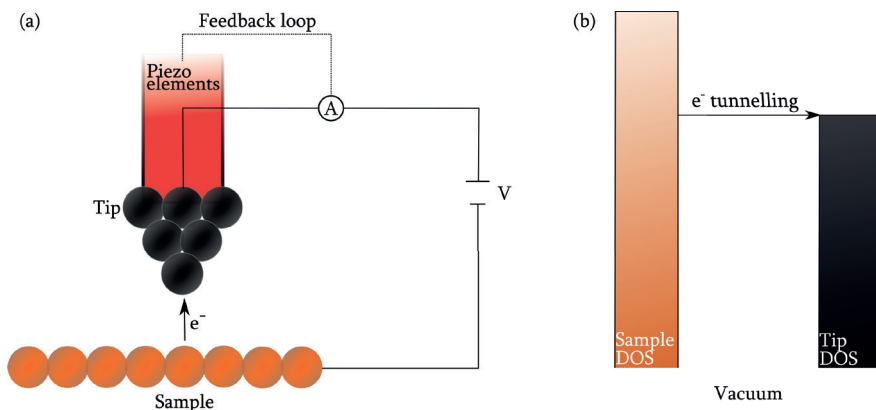
Figure 2.1:   Schematic representation of an STM setup.
(a) A bias voltage is applied to the sample (orange) in reference to the tip (black). Piezo-electric elements bring the tip in close proximity to the surface of the sample. The current is measured when electrons tunnel between tip and sample. **(b)** Schematic diagram of electrons tunnelling from the DOS of the sample through the vacuum to the tip.

To perform these kind of measurement, there are a few requirements that need to be fulfilled. First, since the distance between tip and surface is crucial for the experiments, any vibrations introduced in the system, via the ground or the air, result in noise, which significantly reduces the resolution of the images. There-fore, during operation, the measuring head which includes the STM tip and the sample are suspended using springs. The springs absorb vibrations introduced via the body of the microscope. It is shown that this technique works well for vibrations with a frequency above the resonance frequency of the spring sus-pension system (typically on the order of a few Hz). Low-frequency vibrations are reduced by using a rigid scan head, which acts as a high pass filter. To-gether, the spring suspension system and the rigid scan head, typically reduce external vibrations sufficiently to enable STM operation.[2]

There are additional techniques to further reduce noise caused by external vibrations. Using pneumatic dampers underneath the setup, vibrations coming from the floor can be reduced. Alternatively, piezo-electric modules can be used, which actively compensate vibrations coming from the floor (c.f. noise-

cancelling headphones). The advantage of the latter approach is that these elements have a strongly reduced resonance at low frequency. To further reduce unwanted vibrations, mechanical pumps are switched off and unnecessary electrical equipment is switched off during measurements or filters are introduced.[6] To enhance the stability of the measurements, the tip and sample can be cooled using liquid nitrogen and/or liquid helium. Unless otherwise specified, all measurements described in this thesis are taken at ~4.5K. Some of the work described in this thesis focusses on individual molecules. In order to visualize and measure individual molecules, the diffusion rate of molecules on the substrate needs to be sufficiently low which is also achieved by cooling down the system to ~4.5K. Lastly, the magnetic fields used in the work described in this thesis, are generated by injecting a current into a coil of superconducting material that surrounds the scan head.. Hence, the temperature of the superconducting coil and STM head should be below the critical temperature of the superconducting material.

2.2 Scanning tunnelling spectroscopy

In addition to imaging, an STM can also be used to perform scanning tunnelling spectroscopy (STS).[2] In this mode, the tip is parked above a position of interest, the feedback loop is disconnected, and the differential conductance (dI/dV) is measured as a function of voltage. It can be shown that the following relation holds:

$$\frac{dI}{dV}(V) \propto LDOS_{sample}(V) \cdot DOS_{tip} \cdot T \qquad (2.2)$$

The differential conductance depends on the local density of states (LDOS) of the sample, density of states (DOS) of the tip, and T is the transmission factor for tunnelling from a sample state to a tip state. Hence, if the DOS of the tip and the transmission factor are independent of the voltage, the $dI/dV(V)$ measured in STS is directly proportional to the local density of states of the sample.

It is possible to measure the current (I) over a voltage sweep to obtain the I/V spectrum and afterwards numerically derive the differential conductance spectrum. This technique is fast but does not yield a high signal-to-noise ratio. Superior data quality can be obtained by applying a small ac-modulation to the bias voltage and using a lock-in amplifier to directly measure the $dI/dV(V)$ signal.

Expanding on this technique, there is also the possibility to take differential conductance maps over the surface of the system of interest. Similar to an STS experiment, the feedback loop is disconnected before the measurement starts. By recording the value of the dI/dV signal at a given bias as a function of po-

sition, spatial variations of density of states at the chosen energy are directly visualized. However, scanning in constant height mode requires the tip and sample to be stable as there is no feedback loop protecting the tip and sample against changes in the tip-sample distance. Such changes lead to distorted images and potential tip crashes into the surface of the sample. Samples with large height differences or areas in which there is not enough electron tunnelling to determine the LDOS, are therefore especially vulnerable to these tip crashes. Height adjusted differential conductance mapping solves this issue. Before recording the *dI/dV* signal of a given scan line, the height variations along that line are determined by scanning in feedback. The same line is then scanned again with the feedback loop turned off, but following the measured height-profile. This mode was used for the experiments involving Bi_2Se_3 nano-platelets, which have thicknesses of multiple nanometres.

2.3 Magnetic field and spin

Hans Christian Ørsted discovered, in 1820, that an electric current flowing through a metallic wire influenced a compass nearby and made the needle deflect. He also saw that this effect was circular around the metallic wire and the effect decreased in strength with increasing wire-compass distance.[7] This experiment showed the connection between electricity and magnetism and is seen as the starting point of the field of electromagnetism. When the wire is now turned into a coil (or solenoid) a directed magnetic field can be created which is similar to a bar magnet and follows Maxwells right-hand screw rule, depicted in figure 2.2.
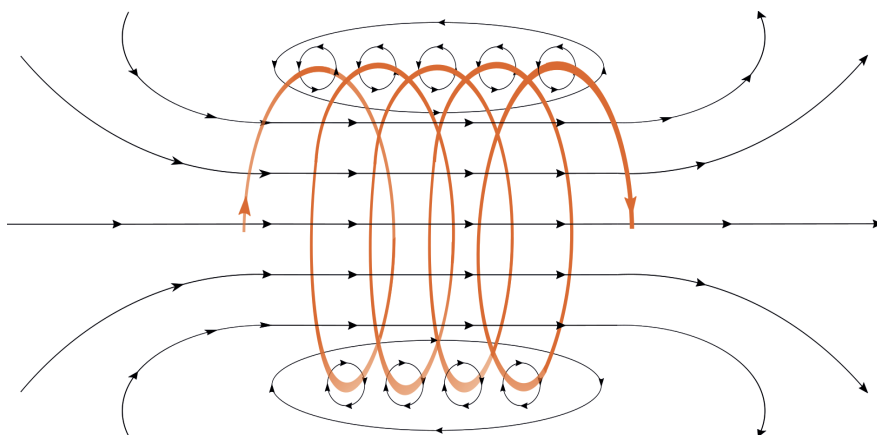
Figure 2.2: Magnetic field produced by solenoid coil, demonstrating the right hand rule.

75 years later it was Pieter Zeeman who utilized such a magnetic field while studying spectral lines of sodium.[8,9] He discovered that the spectral lines broadened under the influence of a magnetic field and eventually split into two lines. This splitting could not be explained at the time with the known physical laws. It wasn't until the beginning of the 1920s that the concept of spin was accepted as the fourth quantum number of an electron which could only have two discrete values, spin up and spin down and explained the findings of Zeeman.[10,11]

As STMs rely on electrons for the tunnelling, this effect of spin can be an important aspect while doing experiments. One of the ways to utilize the spin of the tunnelling electrons in an STM is to apply a strong magnetic field using a solenoid coil, as shown in figure 2.2. A sample can now be placed inside of this coil so that a magnetic field is applied perpendicular to the sample. In some microscopes there is also the possibility to have a magnetic field parallel to the sample however for projects described in this work, this was not the case.

The first effect of the magnetic field on the spin of electrons is the beforementioned Zeeman effect. Electrons (within an atom) reside at discrete energy levels which are quantized. The state of each electron can be described by a set of four quantum numbers: the principal quantum number n, which describes the size of the orbital and can only have integer and positive values including 0. The second quantum number l describes the orbital angular momentum and has integer values between 0 and n-1. Thirdly, m is the magnetic quantum number and can possess any integer value from -l to +l. Lastly, s is the spin quantum number which can be either +½ or -½, corresponding to spin up and spin down, respectively. The Pauli exclusion principle states that an electronic state cannot be occupied by two electrons with the same quantum numbers. Thus, each orbital will be filled with one electron with spin quantum number +½ and one with spin quantum number -½. In the absence of a magnetic field, these two states have the same energy. However, in an external magnetic field, one of the states decreases in energy, while the other state increases by the same amount. This splitting is described by:

$$\Delta E = +\frac{g \cdot \mu_B \cdot B}{h} \tag{2.3}$$

with ΔE the difference in energy, g the effective Landé factor, μ_B the Bohr magneton, h is Planck's constant and B is the strength of the magnetic field.[8,9,12]

The second magnetic field effect does not apply specifically to the spin of the electron but rather to the negative charge of the electron and its motion: the Lorentz force, which is given by the following equation:

$$\mathbf{F} = -\,e(\mathbf{v} \times \mathbf{B}) \tag{2.4}$$

With $\mathbf{F}$ the magnetic force acting on the particle, e the electron charge, $\mathbf{v}$ the velocity and $\mathbf{B}$ the applied magnetic field. As $\mathbf{v} \times \mathbf{B}$ is a vector cross product, the force acting on the electrons is directional, leading for example to the Hall effect.[13,14] The Lorentz force will predominantly have an effect when electrons are confined to a specific motion like for a two dimensional topological insulator (chapters 3 and 4) or in a quantum corral (chapter 5).

Ch.
2

Bibliography

1. Mueller, M. P. *Fundamentals of quantum chemistry: molecular spectroscopy and modern electronic structure computations.* (Springer US, 2007).

2. Voigtländer, B. *Scanning probe microscopy: atomic force Microscopy and scanning tunneling microscopy.* (Springer Berlin Heidelberg, 2015).

3. Getzlaff, M. *Fundamentals of magnetism.* (Springer, 2008).

4. Merzbacher, E. The early history of quantum tunneling. *Phys. Today* **55**, 44–49 (2002).

5. Binnig, G., Rohrer, H., Gerber, Ch. & Weibel, E. Surface studies by scanning tunneling microscopy. *Phys. Rev. Lett.* **49**, 57–61 (1982).

6. Karnopp, D. Active and semi-active vibration isolation. *J. Vib. Acoust.* **117**, 177–185 (1995).

7. Nielsen, J. R. Hans Christian Oersted—Scientist, humanist and teacher. *Am. J. Phys.* **7,** 10–22 (1939).

8. Landé, A. *Über den anomalen Zeemanefekt.* (1921).

9. Zeeman, P. Radiating atoms in magnetic fields. *J. Frankl. Inst.* **199**, 585–596 (1925).

10. Uhlenbeck, G. E. & Goudsmit, S. Ersetzung der hypothese vom unmechanischen zwang durch eine forerung bezüglich des inneren verhaltens jedes einzelnen elekrons. *Naturwissenschaften* **13,** 953–954 (1925).

11. Commins, E. D. Electron spin and its history. *Annu. Rev. Nucl. Part. Sci.* **62**, 133–157 (2012).

12. Ball, D. *Physical chemistry.* (Cengage Learning, 2002).

13. Dunlap, R. A. *Electrons in solids: contemporary topics.* (Morgan & Claypool publishers, 2019).

14. Hook, J. R. & Hall, H. E. *Solid state physics.* (Wiley, 1991).

Chapter 3:
Characterization of edge states in Bi$_2$Se$_3$ nanoplatelets

Due to tremendous advances in synthetic chemistry, one now has full control over the dimensions and surface chemistry of colloidal nanocrystals. This has resulted in these materials being used in opto-electronic applications, e.g. displays. The question now is, can these crystals also form a platform for quantum materials, in which electronic coherence is key? In this chapter, we investigate the electronic properties of colloidally synthesized, two-dimensional Bi$_2$Se$_3$ crystals, with uniform thickness and limited lateral dimensions. STM is used to study the evolution of a three-dimensional topological insulator to the technologically important case of two-dimensional materials. It is shown that for 4,5 and 6 quintuple layers (QLs), we observe an edge state of ~8 nm width around the entire crystal. For 3QL thick crystals however the edge state is ill-defined and shows different behaviour per crystal.

Ab-initio theory and a low energy continuum model confirm that crystals with thicknesses of 4 or 5QL have a non-trivial band structure with a one-dimensional quantum state at the edge. The calculations do not fully agree on the state of crystals of 3 and 6QL, with ab-initio theory finding that $Z_2 = 0$ for crystals, 3QL in thickness and $Z_2 = 1$ for crystals, 6QL in thickness but the low energy model finds the opposite. The processability and dimensional control of colloidal topological insulator nanocrystals opens a unique window to devices with a large density of addressable quantum states.

"All you need is a chip and a chair"
– Joe Stapleton

3.1: Introduction

The field of topological insulators (TIs) has seen an increase in interest in recent years. The quantum states present at the boundaries of TIs are protected by band topology and may find applications in electronic and spintronic devices. Most of the research on topological insulators has been performed with macroscopic crystals (bulk, layers and sheets).[1–3] Lithography techniques have been used to create nanoscale materials required for device application. It would, however, also be interesting to be able to colloidally synthesize TIs, as this would create more control over the vertical and lateral dimensions. It has been shown that this control in parameters can be used to create crystals with tuneable absorption and emission spectra. These nanocrystals have thus been used in opto-electronic industry as phosphors in LEDs,[4] photodetectors[5] and luminescent solar concentrators.[6,7] The question now is whether these kind of nanocrystals can also be tuned in such a way that enables control over coherent electronic states. In this chapter, the electronic properties of colloidally synthesized Bi_2Se_3 nanoplatelets (NPLs) are investigated using STM. The observed characteristics are then explained using two theoretical models. The details on the synthesis of the NPLs as well as the details on the theoretical models can be found in the paper this chapter was based on.
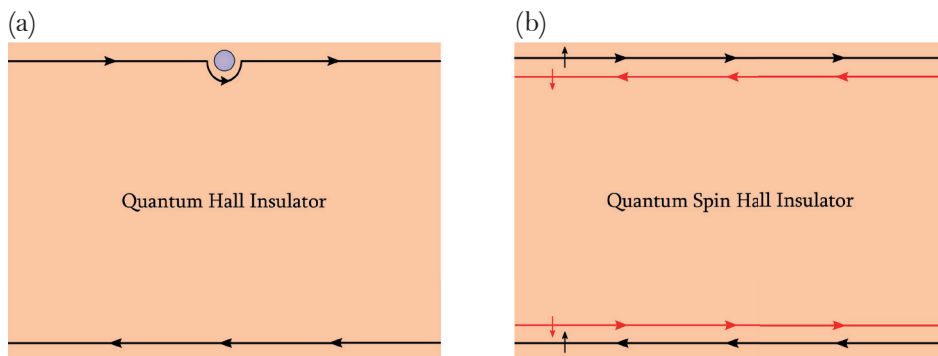
3.2: Quantum (spin) Hall insulators

Topological insulators are materials with unique electronic characteristics. The bulk of the material is an insulator whereas the boundaries (surface or edges) are conducting. For a 3-dimensional (3D) material this means that the surface is conducting, whereas for a 2-dimensional (2D) material only the one-dimensional edge has conductive properties. The states at the boundaries, located in the bandgap originally present in the bulk, are called quantum spin Hall (QSH) states. These states are similar to the quantum Hall (QH) states with the main difference that no external magnetic field is necessary for these states to be present.[8]

The QH states appear when a 2D electron gas is placed in a sufficiently strong magnetic field.[9] The electrons are bend following the right-hand rule of Fleming.[10] Figure 3.1a shows how this will create two lanes on the edge of the material with electrons, one lane going forward and one going in the opposite direction. If a defect would be present at one of these edges, the electron would simply go around this defect. It is not possible for the electron to be scattered by the defect as this would mean it would have to reverse its direction against the flow of the lane. This is called dissipationless transport. Current electronic devices do not have this type of transport and therefore electrons can be scattered leading to a loss of energy. Hence, the prospect of creating materials

which are protected against backscattering would reduce the energy consumption of electric devices. Since the quantum Hall effect requires unpractically large magnetic fields (typically >5 T), this effect cannot be used in everyday devices.[9,11–13]

Independent work from Kane and Mele[14,15] and Bernevig and Zhang[16] showed that a similar effect can be created when spin-orbit coupling is introduced. The boundary states originate from an inversion of two bands due to strong spin-orbit coupling. The bulk boundary principle explains that the bands obtain the normal roles just outside the crystal. There is hence always a location where the bands "touch", that is the location where the edge states arise. Per edge there are two lanes, spin up electrons move forward in one lane whereas the spin down electrons would be moving backwards in the other lane, as shown in figure 3.1b, this is called spin-momentum locking. These boundary states are similarly robust against defects since backscattering is prohibited as the electron would have to flip its spin in order to backscatter. This spin flip can occur however when the impurity is magnetic or when an external magnetic field is applied (this topic will be studied further in chapter 4). These states are called helical boundary states or QSH states.

(a)   (b)

Figure 3.1: Schematic representation of a quantum Hall insulator and a quantum spin Hall insulator

(a) A two dimensional spinless quantum Hall system with spatially separated edge states. The channel at the top only has electrons moving to the right whereas the channel at the bottom only has electrons moving to the left. The robustness of the top channel is shown by the edge state going around the impurity (blue dot) without backscattering. **(b)** A two-dimensional quantum spin Hall system with two channels of two electrons of opposite spin propagating in opposite directions on each edge. The top edge has spin-up electrons moving to the right and spin-down electrons moving to the left. For the bottom edge, the opposite is true.

3.3: Characteristics of Bi$_2$Se$_3$ crystals

Helical edge states originate from an inversion of the conduction and the valence band, which is caused by the strong spin orbit coupling present in some materials.[11,16] Bi$_2$Se$_3$ has such spin-orbit coupling and was one of the first experimentally verified topological insulators..[17] Bi$_2$Se$_3$ has one, relatively large, inverted gap at the Gamma-point of ~0.3 eV. This makes it easier to observe boundary states and makes these states robust against thermal excitation.[17,18] Three-dimensional Bi$_2$Se$_3$ has been the focus of numerous studies including, measurements on step edges from grown layers, surface states of bulk crystals and surface states induced by substitution.[19–26] There is however, no work on the electronic properties of colloidally synthesized 2D Bi$_2$Se$_3$.

Bi$_2$Se$_3$ grows in quintuple layers (QL) with a Se-Bi-Se-Bi-Se configuration. These layers stack to form platelets of multiple QLs with every layer connected via van der Waals interaction. Hence, it is an ideal material to study the transition from a 3D to 2D. A preliminary model (a 4-band **k·p** model) indicated that for 3 to 6 QL films the material should act as a 2D topological insulator whereas for 7QL and higher the material will behave as a 3D material.[16,27] Since every QL has a thickness of ~0.96nm,[28] the synthesized platelets should ideally be in the range of 2 to 8nm, which is measurable by STM.

3.4: Synthesis and preparation

Different methods have been reported in literature to synthesize 2D colloidal Bi$_2$Se$_3$ platelets.[29–32] For this research two of these methods, hot injection and polyol reflux, are combined to create stable well-defined nanoplatelets. Afterwards, additional washing steps are performed to prepare the samples for STM measurements.

3.4.1: Hot injection method

The hot injection method was developed to synthesize nanocrystals with a narrow size distribution. A solution of solvent with one of the precursors is heated up to a certain temperature after which a cold solution of the different precursor is added. Initially the heat from the solvent in the flask will lead to a burst of nucleation. However, since the added solution of the second precursor will be 'cold' i.e room temperature, the nucleation rate will rapidly decrease. After this has happened the solution with the nuclei will enter the growth stage in which no new nuclei can be formed but monomer units will add to the existing nuclei, thereby growing the nanoparticle. Separating this nucleation process and the growth stage is vital in creating a narrow size distribution.

Previously, it has been shown by Wei *et al.*[30] that it is possible to synthesize Bi_2Se_3 nanoplatelets using the hot injection method. A precursor of bismuth would be added to a hot solution of selenium in oleylamine (OLAM). When replicating this synthesis, we found that the formed crystals tended to aggregate. This made it impossible to discern the shape and size of the individual crystals. Additionally, these aggregated clusters are not suited for STM experiments.

3.4.2: Polyol reflux method

The second method to create nanoplatelets is the polyol reflux method.[33] This method is a heating up method in which the precursors are all added to the flask simultaneously and the mixture is slowly heated up under atmospheric conditions using a reflux condenser. The polyol will first act as a solvent for the precursors resulting in an intermediary phase. Secondly the polyol will act as a reduction agent. The balance between the consequent dissolution of this intermediary phase and the reduction process will drive the nucleation process. This nucleation process can be tuned by changing the temperature in the following way:

When the temperature is higher, the dissolution rate of the intermediary phase and the rate of reduction will be higher. Therefore, the rate of the creation of nuclei will also be higher, resulting in more nanocrystals. When there are more nanocrystals being formed in the growth phase, there are less monomers available per nanocrystal resulting in smaller nanocrystals.

We performed a polyol synthesis of Bi_2Se_3 NPLs, replicated from Zhang *et al.*[29] A solution of bismuth precursor, selenium precursor, ethylene glycol (EG) and polyvinylpyrrolidone (PVP) was heated to 190 °C and left for two hours. In this synthesis, the EG acts as the polyol solution and the PVP is a (charged) polymer which should attach to the NPLs, to prevent aggregation.

When checking the formed crystals in an Transmission Electron Microscope (TEM), large, rod-like structures were present, which created aggregations of the nanoplatelets. Trying to use size-selective precipitation did improve the sample but still too many large structures were present to put this sample in the STM.

3.4.3: Polyol hot injection method

Both synthesis methods have their downsides making them unusable for STM experiments, therefore it was decided to combine both methods to try and gain more control over the different parameters. The mixture in the flask was similar to the mixture used in the polyol synthesis however the bismuth precursor was removed and added as a precursor in the same way as in the hot injection method. The advantage of the combination of these two methods is that the nucleation and growth phases are better separated while the PVP is present to

Ch.
3

stabilize the platelets and prevent aggregation. A full description of the synthesis method and the chemicals can be found in Supporting Information S3.1.

This new method resulted in well-defined, dispersed Bi$_2$Se$_3$ nanoplatelets. Figure 3.2 shows representative TEM and ambient-AFM images, as well as the distributions in lateral size and thickness extracted from multiple images. Both of these techniques can be used to determine the lateral sizes of the platelets, the electron beam of the TEM however can give information about the structure of the platelet whereas the scanning tip of the AFM can be used to determine the thickness. NPLs can be seen in different well-defined shapes and uniform thicknesses. About 2/3rd of the platelets have a hexagonal or triangular structure whereas the rest is irregular in lateral shape but still shows an (atomically) flat surface. Using TEM and AFM, statistics were acquired on the dimensions of the platelets after synthesis. Figure 3.2c shows the statistics of the lateral dimension measured with TEM. A lateral dimension of 159 ± 38nm was found.

AFM was used to determine the thickness of the synthesized particles. Figure 3.2d shows quite a heterogeneity in the distribution of thicknesses of the synthesized platelets between 2 and 9 nanometres. Bi$_2$Se$_3$ grows in quintuple layers of ~1 nm per layer[28], it is therefore assumed that the size distribution shown in figure 3.2d corresponds to nanoplatelets of 2 to 9 QL in thickness. Literature suggests that a QSH edge state should be visible for platelets of thicknesses between 3 and 6 QL.[16,27] The size distribution found shows that the majority of platelets will be 5 or 6QL in thickness and is therefore ideal to probe this state. Since there are also sub 3QL platelets as well as platelets thicker than 6QL, it should be possible to study the thickness dependence of the QSH state in Bi$_2$Se$_3$.

To investigate the crystallinity of the nanoplatelets, High-angle annular dark-field scanning transmission electron microscopy (HAADF-STEM) was performed. This technique can be used to measure differences in thickness and therefore shows any disorder present in the Bi$_2$Se$_3$ NPLs. When a platelet is perfectly homogeneous it should be the same contrast over the full area, however any disorder and reduction in thickness shows as a reduction in brightness. Any deposition on the surface on the other hand will show as an increase in brightness. Figure 3.3a shows the uniform thickness as well as the crystallinity of a Bi$_2$Se$_3$ NPL. Some small areas of disorder can be seen on the edge of the crystal displayed by a darker colour in the HAADF-STEM image. One of such areas can be seen in figure 3.3b which shows the difference between a well-ordered crystalline edge and a more disordered edge. The width of the disorder is quite irregular and most of the edge of the crystal is unaffected. The disorder originates from an in-situ annealing procedure at 393K for 2 hours which is similar to a procedure necessary for STM measurements. Further elaboration on this procedure will follow in the next section. Additional HAADF-STEM images on the NPLs before this annealing procedure can be found in SI figure S1.
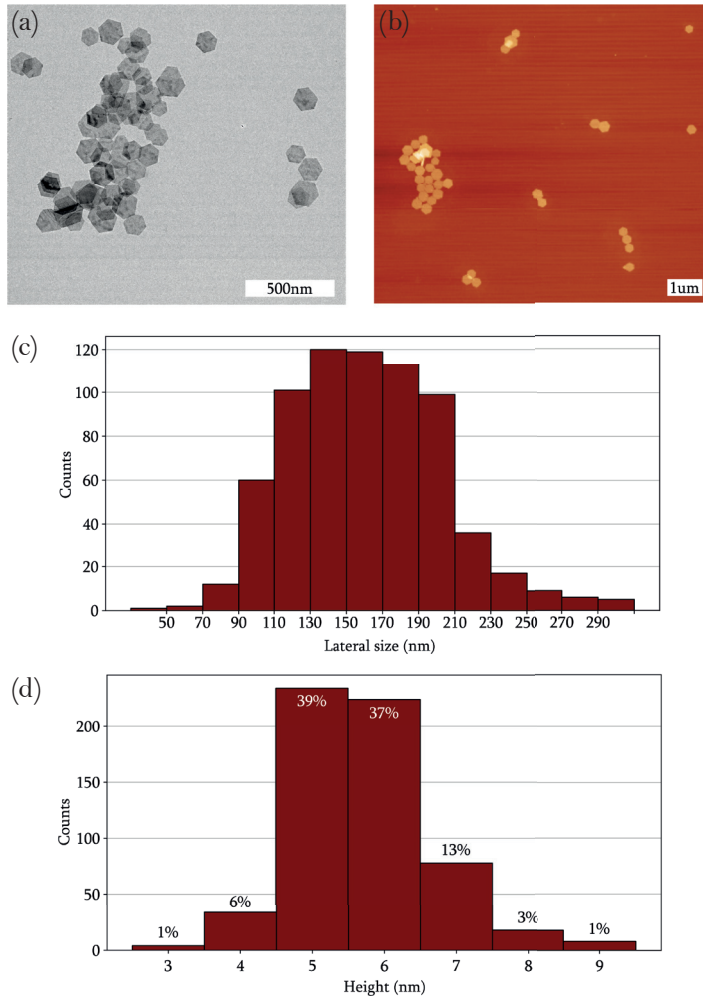
Figure 3.2: **Characterizing the different dimensions of Bi$_2$Se$_3$ NPLs using TEM and AFM.**

(a) TEM image of an ensemble of Bi$_2$Se$_3$ NPLs. **(b)** AFM image of an ensemble of Bi$_2$Se$_3$ NPLs. **(c)** Lateral size distribution of synthesized Bi$_2$Se$_3$ NPLs. The results were obtained from TEM image by measuring the largest corner to corner length (i.e., maximal diameter) of 700 hexagonal NPLs of different samples. **(d)** Thickness distribution rounded to integer nanometres to determine the distribution of NPLs in number of quintuple layers. The results were obtained by measuring 600 Bi$_2$Se$_3$ NPLs of different samples with AFM.
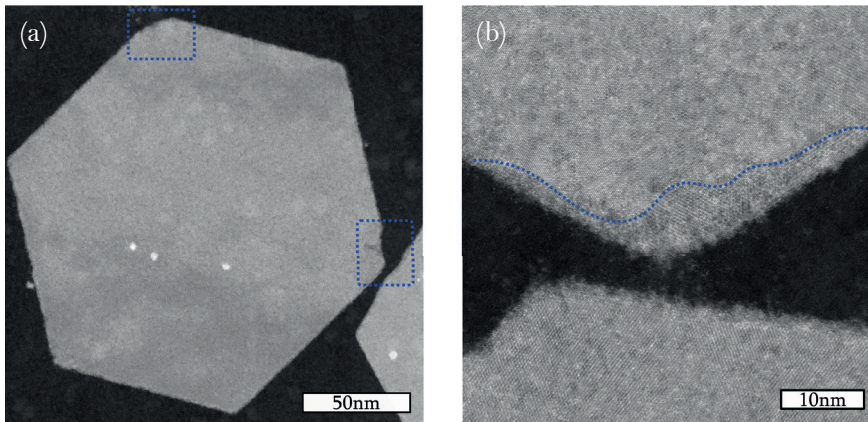
Figure 3.3: **Characterizing the crystallinity of Bi$_2$Se$_3$ NPLs using HAADF-STEM**

(a) HAADF-STEM image of a single crystalline Bi$_2$Se$_3$ NPL after in-situ annealing for 2 hours at 393K displaying some areas of disorder (outlined in blue). **(b)** HAADF-STEM image displaying the slight disorder in small areas of an NPL

3.4.4: Preparation of the Bi$_2$Se$_3$ NPLs for STM measurements

The PVP polymers present in the mixture ensure that the platelets do not aggregate during synthesis nor while in solution afterwards. These PVP polymers are flexible organic molecules and because STM measurement require a stable tunnel junction, the presence of PVP can cause problems during imaging. It is necessary to strip these polymers away before inserting the sample into the STM. This creates a delicate balance however, as stripping of the PVP polymers will cause the platelets to cluster and in order to take STM measurements it is important that the NPLs are separated on the substrate. After different iterations of washing with hydrazine and OLAM as well as using different concentrations, the following procedure was found to create a solution of NPLs suitable for STM. After synthesis hydrazine or OLAM was added to the solution with NPLs on a 1:1 ratio and shaken vigorously. The NPLs were subsequently isolated by centrifugation and redispersed in 1mL ethanol. The resulting dispersion was washed a minimum of two times by addition of (a mixture of) ethanol and acetonitrile, followed by centrifugation and redispersion of the precipitate in 1 mL of ethanol. Afterwards the solution was drop-casted on an Au(111)/MICA substrate and annealed at 370K for one to two hours in ultra-high vacuum. To ensure that the post-synthesis procedure does not affect the structure of the crystals, an in-situ annealing experiment was performed

followed by high resolution HAADF-STEM. Results are shown in figure 3.3. It was concluded that there are some affected areas on the crystal, but the damage was minimal and should not affect the STM measurements.

3.5: Theoretical models

STM and STS can measure the electronic density of states of the crystals at different locations. The local density of states can give information about states at the edge of the crystals but does not give information regarding spin, thus STS cannot provide absolute proof of the helicity of the edge state. Theoretical models on two levels of complexity will be used to predict the presence or absence of edge states and their exact nature. The model mentioned in section 3.2, to describe topological edge states was extended to feature the first set of bulk bands. This extended model is called the 8-band **k·p** model in comparison to the low-energy effective model of Zhang. Additionally, a GW approximation is used on top of first-principles density functional theory (DFT) which is combined with tight-binding (TB) calculations.

3.5.1: Low-energy 8-band k·p model

Zhang et al.[17] described 3D Bi_2Se_3 around the 3D Γ point using a low-energy effective model. They devised a Hamiltonian from four low lying states at the Γ point, for the finite wave vector **k**, taking into account the relevant symmetries: time-reversal symmetry, inversion symmetry and three-fold rotation symmetry along the z-axis. This model shows that a 3D TI continuously deforms into a 2D QSH insulator. However, the model does not predict at which thickness the transition occurs. Angle-resolved photoemission spectroscopy (ARPES) measurements have shown that the topological states at the top and bottom of a Bi_2Se_3 crystal hybridize for a thickness $\leq 6QL$, however ARPES does not show whether an edge state is present. ARPES uses the photoelectric effect to measure the band structure of a sample. This technique can however only measure the band structure of thin films and not of the edge of the produced NPLs. Therefore, the 4-band model was extended by introducing the first set of four surface bands closest to the Fermi level, thereby extending the Hamiltonian devised by Zhang into an 8x8 Hermitian matrix. Using this model, the energy spectrum as well as the Z_2 invariant can be calculated for infinite systems. A non-zero value of the Z_2 invariant indicates that a finite crystal will feature topologically protected non-trivial states at its boundary.[34]

3.5.2: GW-TB model

The limitation of the 8-band **k·p** model is the inability to simulate the full band structure for a material over the entire 2D Brillouin zone. In order to obtain the complete band structure and therefore the density of states (DOS)

of Bi$_2$Se$_3$, a GW-TB model is used. This model is a combination of the GW approximation in Density Functionality Theory (DFT) and Tight Binding calculations (TB). DFT is a type of calculation used to determine the electronic structure of atoms, molecules and solids.[35,36] Our finite-sized Bi$_2$Se$_3$ crystals are too large (contain too many electrons) to be treatable with DFT. Therefore, an infinite crystal with a limited thickness is used to calculate the Wannier wave functions as well as the Hamiltonian from which a TB model is build. Before these parameters are extracted however, the GW approximation is used. This approximation introduces self-energy to the electrons while they propagate through the system. The self-energy is a product of G, the one-body Green's function describing the propagation of the electron in an interacting system, and W, the Coulomb interaction. This means that the electrons consider the system as a charge density and only the linear response of this density is taken into account.[37]

The TB model describes electrons in a system which are tightly bound to the atoms and therefore have limited interaction with their surroundings. The resulting wave function will thus be similar to the atomic orbital and therefore in chemistry this model is also referred to as the linear combination of atomic orbitals model (LCAO). This model is often used to describe larger solids and crystals as it requires less computing due to the lack of electron interaction. The wave functions extracted from DFT with the GW approximation include the self-energy of the electrons, thus combining these methods will yield a good approximation to the synthesized Bi$_2$Se$_3$ nanoplatelets.[37]

3.6: Results and discussion

To determine whether there is a state on the edge, and what the nature of this state might be, different nanoplatelets of varying thicknesses are investigated using STM and STS. By taking *dI/dV* spectra on different areas of the NPLs, the density of states of the interior and edges of the platelets can be compared. Lastly, height adjusted differential conductance mapping can be used to study the spatial extent of electronic states.

The distribution in thickness found in STM is smaller than the distribution previously found in AFM. There are two possible explanations for this observation. Firstly, as the STM is able to image the particles without problems it can be assumed that most of the PVP polymers are removed upon washing. The platelets of a thickness more than 6QL are generally larger, laterally, creating a larger area on the sides of the platelet where other nanoplatelets can aggregate, leaving the smaller platelets measurable in STM. A second reason is incomplete sampling. The maximum scan range of our STM is ~1x1 μm², whereas the field of view in AFM and TEM images can be as large as ~100x100 μm². This allows for imaging many crystals at the same time whereas in STM only a small number of crystals can be imaged at the same time and thus no extensive

statistics can be obtained about the distribution.

Both ambient AFM and ultra high vacuum (UHV) STM are sensitive to the cleanliness of the surface of the platelets. In general, STM offers higher spatial resolution and therefore more defects and undefined moieties can be detected. It is also possible that the post synthesis treatment creates more defects and hampers the cleanliness. It is important to note that post-synthesis induced deformations and non-magnetic defects should not affect the topological edge states of Bi_2Se_3 platelets.

Figures 3.4(a-d) show height profiles corresponding to a selection of NPLs imaged using STM, shown in the respective insets. Most of the platelets show the hexagonal shape previously seen in AFM and TEM, as well as matching lateral sizes. Some NPLs show some defects and/or some adsorbates on the surface. The heights determined from the height profiles correspond to NPLs with 1, 3, 4, and 6 QL respectively, (additional measurements on a 4QL and 5QL platelet can be found in supplementary figures S3.2 and S3.3). It should be noted that the 1QL platelet in figure 3.4a was synthesized using an adjusted synthesis procedure and therefore is not shown in the TEM and AFM images and statistics in figure 3.2. A different Bi precursor was used which has shown to result in thinner NPLs.

After determining the thickness of the platelet, differential conductance spectra were taken along the blue and red lines shown in the inset of figures 3.3(e-h). We took the absence of irregular and spiky spectroscopic data as a measure of the cleanliness of the surface of the Bi_2Se_3 crystal under investigation. All spectra taken more than 10nm away from the edge of the crystal are similar. (see also SI figure S3.4). The spectra shown in blue in figures 3.4(e-h) represent the average spectrum along the blue line, with a blue gloom for the standard deviation. The first noticeable result is that although Bi_2Se_3 is a semiconductor with an inverted gap of 300meV, there is a finite (non-zero) DOS in much of the bandgap region (between -0.8V and -0.2V). It will be shown later that this is in agreement with theoretical predictions.

The LDOS within ~10nm of the edge of the crystal is significantly different compared to spectra taken in the interior. The averaged STS spectra are shown in red in figure 3.4(e-h), the path along which the spectra were averaged is indicated by the red line in the inset. A red gloom again shows the standard deviation in these datasets. The STS data on the NPL with a thickness of 1QL (figure 3.4e) does not show any difference in the DOS at the edge or in the interior of the platelet. This leads to the conclusion that there is no additional state at the edge of the crystal and therefore a 1QL thick Bi_2Se_3 NPL cannot be considered as a 2D TI. In figure 3.4f the averaged dI/dV data is shown for an NPL with a thickness of 3QL. There is again quite some similarity in the DOS at the edge and interior however there is some increased intensity around -0.6V

Ch.
3
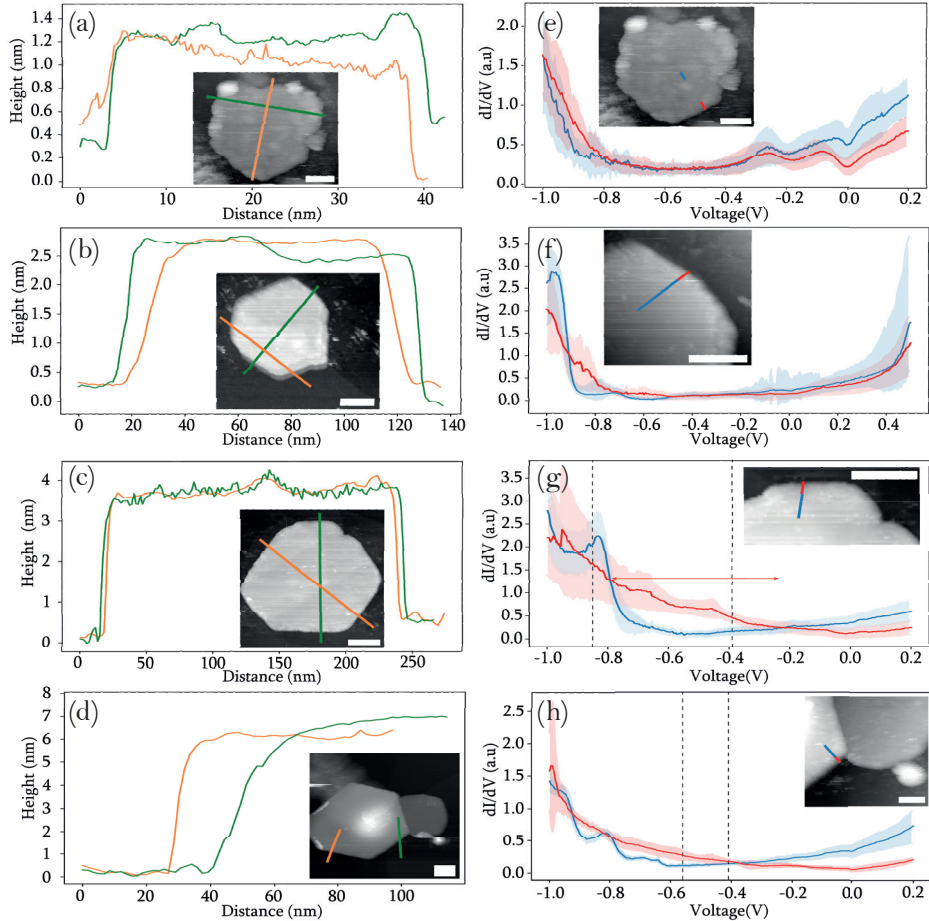
Figure 3.4: **Characterization of the dimensions and electronic states of Bi$_2$Se$_3$ platelets with varying thicknesses, using scanning tunnelling microscopy and spectroscopy.**

(a-d) Height profile of a single platelet on a flat Au substrate along the orange and green lines shown in the inset. The height profiles indicate that these platelets consist of 1QL (a), 3QL (b), 4QL (c) and 6QL (d). **(e-h)** Averaged scanning tunnelling spectrum (proportional to the local DOS(x,y,E)) in the interior(blue) and at the edge (red). The blue curve is an average of multiple (between 5 and 25) positions on the blue line in the inset. The standard deviation is presented as a blue gloom. The red curve presents an average over multiple (between 5 and 8) positions on the red line. The standard deviation is presented as a red gloom; these spectra represent the edge state. The red arrow in fig. 3.4g represents the energy region over which the density of states at the edge is larger than in the interior. The set point in the spectroscopy is 1nA.

for the DOS at the edge of the crystal. This could be an indication that a 3QL thick platelet possesses an edge state, however an increased DOS in the entire bandgap region is to be expected if the platelet where to have a well-defined QSH edge state. From this data it is not possible to conclude whether a Bi_2Se_3 NPL with a thickness of 3QL can be considered as a 2D TI. Later in this chapter it will be investigated further whether Bi_2Se_3 NPLs with a thickness of 3QL are topologically trivial or non-trivial.

The first clear change visible in the spectra acquired on nanoplatelets of 4 and 6 QLs (figure 3.4h and 3.4j) is that the peak around -0.85V present in the spectra taken at the interior is not present in the spectra taken at the edge. More importantly, in the energy range between -0.8V and -0.2V, the DOS is higher for the spectra taken close to the edge of the NPL. This indicates the presence of an electronic state at the edge of nanoplatelets of theses thicknesses. In order to quantify the stability and extend of this electronic state, adjusted height differential conductance maps of these NPLs were taken at two energies (indicated by dotted lines in figure 3.4g and 3.4h), the resulting maps are shown in figure 3.5. Figure 3.5a shows an LDOS map taken at -0.85V on the 4QL thick platelet, it can be seen that all around the edge of the crystal there is an 8-10nm band, with less intensity than in the interior of the crystal. Conversely, the inverse can be seen when taking a map in the energy region between -0.8V and -0.2V, as shown in figure 3.5(b-d). This band follows the entire circumference of the crystal, without large density fluctuations, despite deformations (fig. 3.5b), a screw dislocation (fig. 3.5c) or attachment to a thinner crystal (fig. 3.5d). This suggests that the observed state is robust against backscattering, which is a characteristic of a helical topological edge state. Further research on the robustness of the QSH state will be addressed in the next chapter of this thesis.

To explain the different observations from the STS data, two theoretical models were used, the 8-band **k·p** model and GW-TB simulations. First, the low energy 8-band **k·p** model was used to calculate a Hamiltonian which was then numerically solved. The result of this is shown in figure 3.6 for a 2D Bi_2Se_3 ribbon with a thickness of 4QL and a width of 100nm. In figures 3.6a the low energy bands can be seen where the colour coding is representative for the localization of the bands (black, blue for the interior and surface layers, respectively). It is clearly visible that the hybridization of the top and bottom surface states creates states which nearly bridge the inverted bandgap originally present in a bulk Bi_2Se_3 semiconductor. This explains the presence of the non-zero DOS in the bandgap region in the spectra taken on different NPLs as shown in figure 3.4. Furthermore, a Dirac line can be seen, in orange/pink, which crosses between the valence and the conduction band coming from a one-dimensional state at the edge. In figure 3.6b the same band structure can be seen; in this figure the spin component for the z-direction is shown. For the edge

Ch.
3
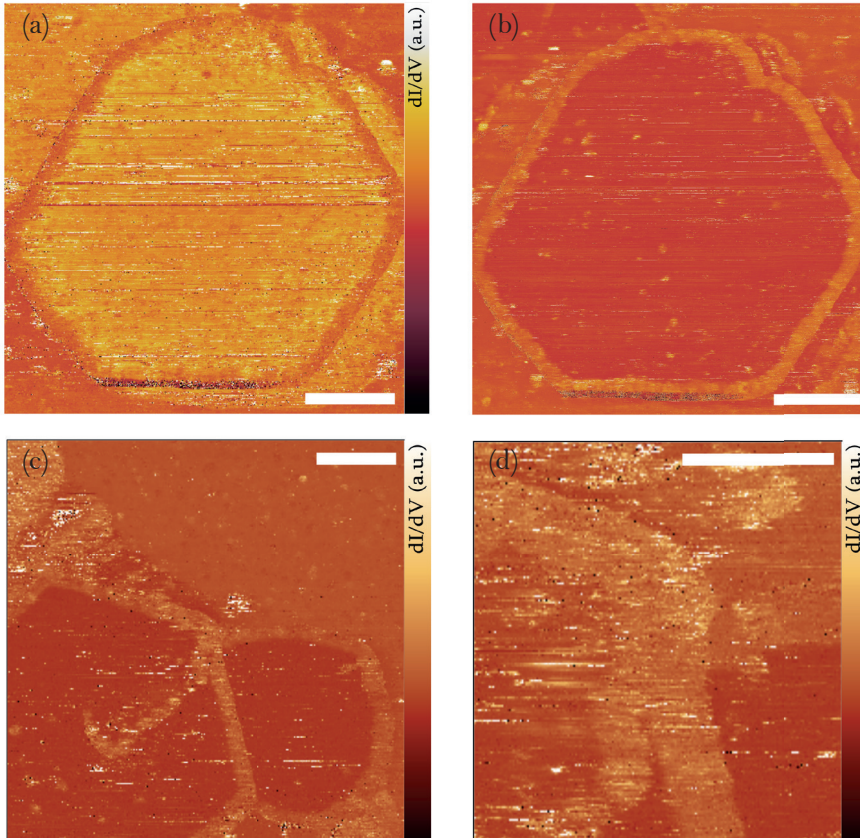
Figure 3.5: **Characterization of the state at the edges of the Bi$_2$Se$_3$ platelet using LDOS maps.**

(a) LDOS map on 4QL NPL acquired at a bias voltage of –0.85V. Current setpoint at background is 0.5nA. **(b)** LDOS map on 4QL NPL acquired at a bias voltage of –0.39V. Current setpoint at background is 0.5nA. **(c)** LDOS map on 6QL NPL (attached to a 4QL NPL) acquired at a bias voltage of –0.41V. Current setpoint at background is 0.5nA. **(d)** LDOS map on 6QL NPL (left) (attached to a 4QL NPL, right) acquired at a bias voltage of –0.56V. Current setpoint at background is 0.5nA.

edge state a spin-polarization was found of 0.5-0.8 $\hbar/2$ which is locked to the momentum. The Dirac line crossing the bands is absent for ribbons with a thickness less than 3QL as shown in figure S3.5. Using the model, the Z_2 invariant was calculated, and it was found that crystals with 1 and 2QLs have a Z_2 invariant of 0 and are thus trivial. Crystals of 3,4,5 QLs have a Z_2 invariant of 1 and hence are QSH insulators. In contrast to what experimental results suggest, NPLs with a thickness of 6QL seem to be trivial ($Z_2=0$) in the 8-band **k·p** model.

To relate this to experimental data a DOS plot was calculated, shown in figure 3.5c, with the blue spectrum showing a calculated spectrum of the interior and red a calculated spectrum of the edge. The shape of the plot is similar to data shown in figure 3.3, a peak in intensity can be seen in the region just inside the valence band, which is lower for the edge. Most importantly however is the heightened intensity in the bandgap region for the calculated edge spectrum for a wide range of energies. The energy range does not fully match the experimental results as the synthesized NPLs are, most likely, doped and therefore the Fermi level is not located at 0V bias.

The width of the calculated state was examined as well using this theoretical model (figure 3.5d). In this figure the intensity at certain energies is plotted against the width of the ribbon (100nm). It can be seen that the raised intensity that was calculated is indeed localized on the extremities of the ribbon with a width in agreement with the experimental results.

For further investigation of the electronic structure of 2D Bi_2Se_3, DFT calculations were performed including the GW approximation, the found parameters were then used in TB simulations. For more details see supporting information S3.2. The resulting band structure for an infinite 2D Bi_2Se_3 crystal with 4QL thickness, calculated using GW-DFT is shown in figure 3.7a. This result is in line with the low-energy 8 band calculations in figure 3.6a: the bandgap is nearly closed due to hybridizing surface states. The tight binding calculations were performed on a 4QL thick ribbon of Bi_2Se_3 with a width of 100nm using the GW-DFT results. The resulting band structures can be seen in figures 3.6b and c, with states originating from the interior shown in blue/green and the states located on the edges shown in red/orange. In figure 3.7b edge states can be seen over the whole energy range depicted. For the region between -0.8V and -0.2V this is completely in line with experimental results as well as the 8-band calculations. There are however a few key differences. In the magnified band structure, shown in figure 3.7c, the edge states starting from the valence band bridge the small remaining gap in energy, however they do not connect to the conduction band. Therefore, it can only be concluded that there is a situation very close to a topological phase transition. More recent results on fully relaxed NPLs of 4QLs (not shown here) depict that the edge state does-connect the valence- and conduction band.

Ch.
3
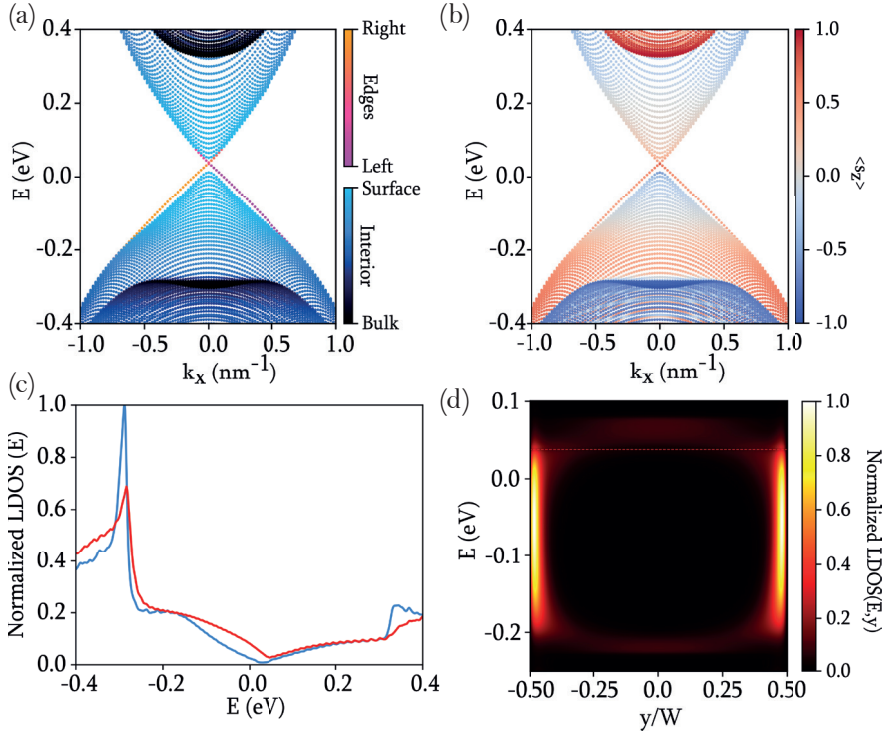
Figure 3.6: **Theoretical analysis of a 2D (4QL) Bi$_2$Se$_3$ ribbon (100nm in width) using the low-energy 8-band k·p model.**

(a) Calculated band structure with states originating from the inner QLs in black, states originating from the hybridized surface states from the top and bottom layers in blue and states originating from the edge in orange/pink. (b) Same band structure as (a), presenting the spin-polarization $<s_z>$. **(c)** Resulting DOS for the interior (blue) and for the edge of the ribbon (red). **(d)** LDOS along the width of the ribbon in the energy range of the bandgap of Bi$_2$Se$_3$. The red dashed line signals the position of the Dirac point.

A comparable situation has previously been reported by Xu *et al.*[38] in BiTl(S$_{1-\delta}$Se$_\delta$)$_2$. Despite the edge states not bridging the bandgap, the resulting states still exhibit the same characteristics as topological states, including spin–momentum locking. To gain more insight in whether this exotic state is equal-ly robust and protected has to be further investigated. The second difference between the experimental results and the GW-TB calculations can be seen in the calculated DOS plot in figure 3.7d, with the interior DOS in blue and the spectrum for the edge in red. Around -0.85V a peak in intensity can be seen for

the interior which is absent at the edge and a heightened DOS is apparent for the energy region between -0.8V and -0.2V at the edge, matching the STS data. In the energy region above -0.2V however there seem to be more edge states available, as is also visible in the band structure in figure 3.7b. These states have not been observed by STS for any of the platelets. Whether this is an artifact or whether adjustments need to be made to the calculations is unclear from the current results. A full description of the calculation of the Z_2 invariant can be found in supplementary section S3.3.

The Z_2 invariant was calculated using the GW method and it is found that 1-3QL and more than 6QL are topologically trivial, with crystals of 4-6QLs having a Z_2 invariant of 1, and are thus QSH insulators. This result is different from the low-energy model as that model predicted crystals with a thickness of 3QLs to be non-trivial and 6QLs to be trivial. It is therefore assumed that these are the border cases for whether Bi_2Se_3 is a QSH insulator or not.

Both experiment and theorical calculations (DFT-GW and 8-band **k·p** model) have shown that Bi_2Se_3 nanoplatelets with thicknesses of 4 and 5QL are topologically non trivial. In contrast, experimental and theoretical data are inconclusive regarding Bi_2Se_3 platelets of 3QL in thickness. To gain more insight into this lower limit, six NPLs with a thickness of 3QL were investigated, all of these platelets have similar lateral dimensions, and have a similar shape. STS data and *dI/dV* maps on two of these NPLs are shown in figure 3.8.

Figure 3.8a shows averaged *dI/dV* spectra taken in the interior and on the edge of a 3QL thick NPL, see the insert. Similar characteristics can be seen as previously observed in the STS data for 4-6QL thick crystals. In a rather large energy range (between -0.8V and -0.3V) there is an increase in intensity, corresponding to a higher LDOS, at the edge of the NPL (red spectrum). The extend of this increase of the LDOS is shown in the differential conductance map at -0.4V shown in figure 3.8b. A clear band of increased intensity around the circumference of the platelet is seen with a width of ~8nm with no noticeable gaps. This is attributed to a QSH edge state.

A different spectrum can be seen for a different 3QL thick platelet in figure 3.8c: the increase in LDOS, in the bandgap region, at the edge of the NPL is minimal. The extend of this difference can be seen in the differential conductance map in figure 3.8d, taken at -0.4V. Instead of a continuous broad ~8nm band along the entire circumference of the crystal, there are pronounced gaps between areas of increased intensity , i.e. there is no continuous edge state for this nanoplatelet. Another difference between the maps shown in figure 3.8b and 3.8d are the intensity modulations: minimal in 3.8b, and prominently visible in 3.8d.

Ch.
3
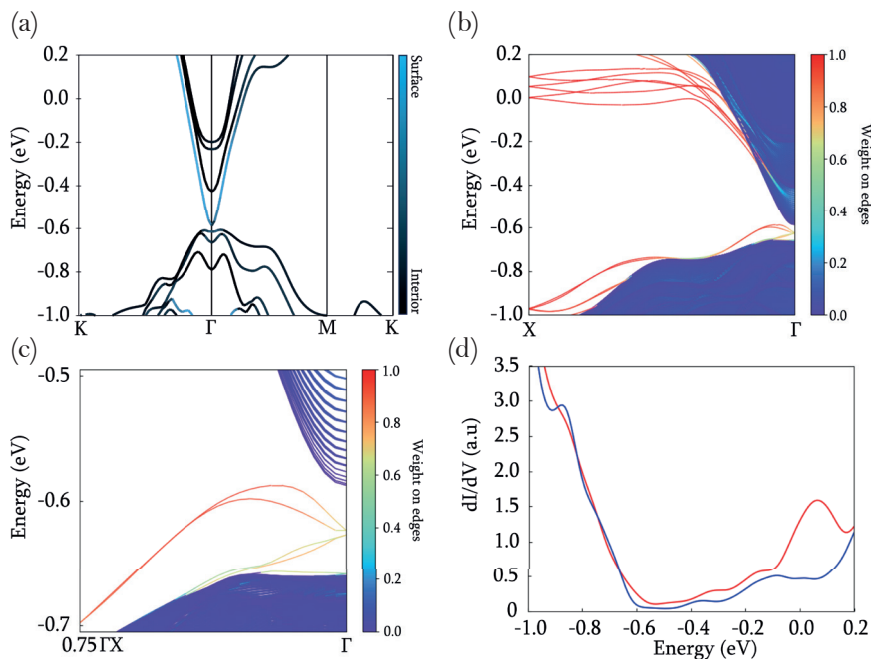
Figure 3.7: Theoretical analysis of a 2D (4QL) Bi$_2$Se$_3$ infinite crystal (a) and a 2D Bi$_2$Se$_3$ ribbon 100nm in width(b-d), using GW-TB calculations.

(a) Calculated band structure with states originating from the inner QLs in black, states originating from the hybridized surface states from the top and bottom layers in blue. **(b)** Band structure along the Γ-X line. The colour indicates the weight of the wavefunction on the regions 2nm from the edge of the crystal. The bands for the interior region are displayed in blue and states situated at the edge are displayed in red/orange. **(c)** Enhanced part of the band structure shown in (b) near the Fermi energy around the Γ-point, displaying the red denoted states from the edges spanning the full band gap. **(d)** Resulting DOS for the interior (blue) and for the edge of the ribbon (red).

For the 6 measured Bi$_2$Se$_3$ nanoplatelets with a thickness of 3QL, only one platelet showed a well-defined edge state, the rest of the platelets showed different gradation of a QSH edge state. Some of the additional data is presented in the supporting information figure S3.6. It is unclear why certain 3QL platelets feature a well-defined edge state and others only show patches of the edge state. All measurements shown are from platelets with similar lateral dimensions and from the same batch of crystals, which shows that small differences are responsible for the presence or absence of an edge state in the case of Bi$_2$Se$_3$ NPLs with a thickness of 3QL. This is in contrast to the very robust QSH edge state for platelets between 4 to 6QL. Interestingly, simulations using the 8-band

k·p model suggest that a 3QL thick platelet is topologically non-trivial, while DFT-GW calculations imply that a 3QL thick platelet *is* topologically trivial.
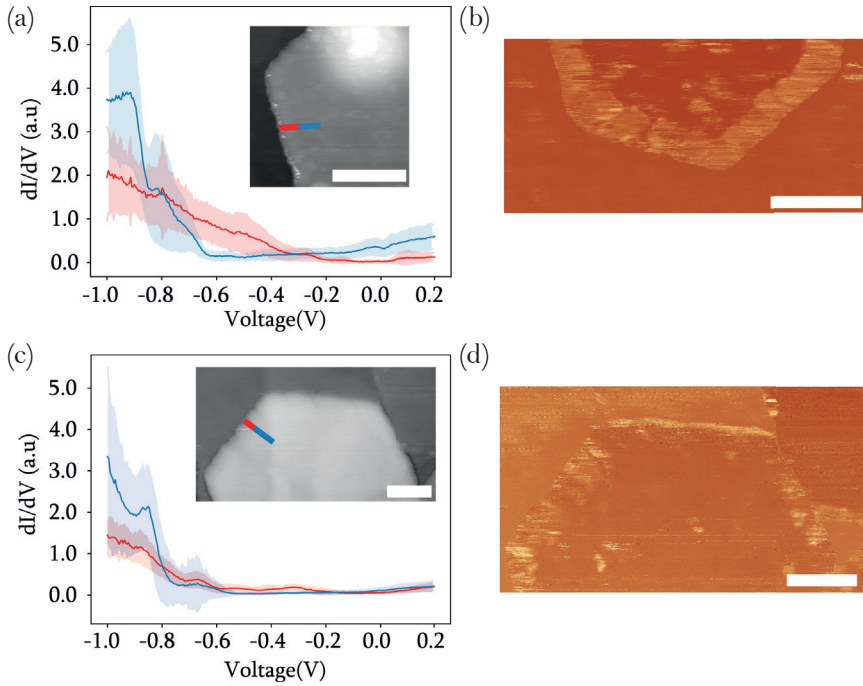
Figure 3.8: **Characterization of QSH edge state in two different 3QL thick Bi$_2$Se$_3$ NPLs using STS and LDOS maps.**

(a,c) Averaged scanning tunnelling spectra of the interior (blue) and the edge (red). The blue curve is an average of multiple (between 20 and 30) positions on the blue line in the inset. The standard deviation is presented as a blue gloom. The red curve presents an average over multiple (between 5 and 15) positions on the red line. The standard deviation is presented as a red gloom; these spectra represent the edge state. The set point in the spectroscopy is 1nA at -1V. **(b,d)** Differential conductance maps on 3QL NPLs acquired at a bias voltage of -0.4V. Current setpoint at background is 0.5nA. Scalebars are 25nm.

3.7: Conclusion and outlook

Bi_2Se_3 nanoplatelets with a homogeneous thickness were colloidally synthesized by a polyol hot injection method. The two-dimensional crystals are 1–9 quintuple layers in thickness and have finite lateral dimensions on the order of 150nm, determined with AFM and TEM. The electronic structure of NPLs with thicknesses of 1-6QL were investigated using scanning tunnelling spectroscopy and differential conductance mapping. For 4-6QL thick platelets a higher LDOS can be observed at a bias of -0.85V which disappears 10nm from the edge of the crystal, subsequently, in the energy region between -0.8V and -0.2V a higher DOS is observed around the entire circumference of the crystals with a width of ~10nm compared to the interior of the crystal. DFT-GW calculations, combined with TB simulations as well as a low-energy 8-band model provide evidence that for Bi_2Se_3 NPLs of 4 and 5QL this is a helical edge state of a two-dimensional quantum spin Hall insulator. Only the DFT-GW method confirms the experimentally shown existence of the QSH edge state in NPLs with a thickness of 6QL.

To determine the lower limit when a Bi_2Se_3 crystal can be considered to be 2D, it was found that at a thickness of 3QL the platelet exhibits different behaviour from platelet to platelet. Some show a well-defined edge state whereas other crystals show only patches of a state on the edge or lack any evidence of the QSH state. The low-energy 8-band model states that a 3QL thick NPL is topologically non-trivial, but DFT-GW calculations conclude that an NPL with such a thickness is topologically trivial. The discrepancies in the experimental spectroscopy results and between the two theoretical models requires further research. For a 1-2QL crystal it is clear that the DOS at the edge and the interior is nearly identical, which is confirmed by theory; these crystals are not QSH insulators.

In order to expand the knowledge on this state in Bi_2Se_3 NPLs more experiments should be performed focussed on platelets with more diverse dimensions. First, more research is needed to determine what influences the QSH edge state of the 3QL thick NPLs as well as determining whether Bi_2Se_3 NPLs with a thickness of more than 6QL possess surface states rather than edge states. Secondly, the robustness of the edge state should be investigated by analysing various defects as well as determining whether the state can be broken by applying a magnetic field. Both topics will be addressed in the next chapter. Lastly, as the width of the edge state is ~10nm it could be interesting to investigate crystals with a significantly smaller diameter to determine at which distance edge states will start to hybridize. In the more distant future, more research should be performed on the transport capabilities of these materials to determine if these platelets can be used as a device for non-dissipative information transfer.

3.8: Acknowledgements

Ch.

3

This chapter is based on the following publication:

Moes, J.R., Vliem, J.F, de Melo, P.M.M.C., Wigmans, T.C., Botello-Méndez, A.R., Mendes, R.G., van Brenk, E.F., Swart, I., Maisel Liceran, L., Stoof, H.T.C., Delerue, C., Zanolli, Z., Vanmaekelbergh, D., *Characterization of the edge states in colloidal Bi_2Se_3 platelets*, Nanoletters (2024), DOI: 10.1021/acs.nanolett.3c04460

Chapter 3: Supplementary information

S3.1 Methods and materials

<u>Chemicals</u>

Na$_2$SeO$_3$ (99%, Aldrich), 0.22 g polyvinylpyrrolidone (Mw = 10,000, Aldrich), ethylene glycol (anhydrous, 99.8%, Aldrich), Bi(NO$_3$)$_3$.5H$_2$O (99,999%, Aldrich) , ethanol (anhydrous 99.8%, VWR chemicals), acetone (anhydrous 99.8%, VWR chemicals), acetonitrile (anhydrous, 99.8%, Aldrich).

<u>Synthesis procedure</u>

Bi$_2$Se$_3$ nanoplatelets (NPLs) were synthesized according to a procedure adapted from Zhang *et al.*[19] During a typical synthesis, 0.05 g of sodium selenite, 0.22g polyvinylpyrrolidone and 9.5 mL ethylene glycol are mixed in a 50 mL roundbottom flask. This mixture is degassed at the schlenkline for 15 minutes at room temperature. After degassing, the colorless solution is heated to 50°C to dissolve all sodium selenite, followed by heating to 190°C under N$_2$. This induces a gradual color change from yellow at 120°C, to orange (130°C), and finally black (135°C). Once the mixture has reached 190°C, a Bi precursor injection solution (0.2 g Bi(NO$_3$)$_3$.5H$_2$O in 1 mL ethylene glycol) is heated under N$_2$ for 30 seconds after its color changed to turbid white, which typically occurs at 140°C. 0.5 mL of this Bi precursor is then injected into the selenium mixture. After leaving the NPLs to grow for 10 minutes at 190°C, the reaction mixture is cooled to room temperature using a water bath. The black product is transferred to a scintillation vial in a glovebox and washed by addition of acetonitrile and ethanol or acetone, followed by centrifugation. The clear supernatant is discarded and the black precipitate is redispersed in 10 mL ethanol. To prevent degradation, the samples were stored in a glovebox under N$_2$ atmosphere. Thinner platelets were prepared by using bismuth oxide dissolved in EG instead of Bi(NO$_3$)$_3$·5H$_2$O.

Prior to high resolution STEM measurements and STM/STS measurements, the NPL samples were treated to remove surfactants and organic contaminants. Depending on the sample, either hydrazine hydrate (N$_2$H$_4$·xH$_2$O 50-60%, Aldrich) or oleylamine (70%, Aldrich) was added to strip off PVP ligands or facilitate additional washing of the NPLs. During a typical treatment, 1 mL of hydrazine hydrate or oleylamine was added to 1 mL NPL dispersion and the resulting mixture was shaken vigorously. The NPLs were subsequently isolated by centrifugation and redispersed in 1 mL ethanol. The resulting dispersion was washed a minimum of two times by addition of (a mixture of) ethanol and acetonitrile, followed by centrifugation and redispersion of the precipitate in 1 mL of ethanol.

<u>Post synthesis procedure</u>

Annealing of the NPLs in the STM is required to remove any remaining con-
tamination and facilitate STM measurements. To investigate the influence of
annealing on the NPLs, in-situ TEM experiments were performed using an
aberration-corrected Thermo Scientific Spectra 300 (S)TEM operating at 300
keV. Parameters were chosen that resemble the conditions in the STM closely:
2 µL of a diluted NPL dispersion was drop-casted on a MEMS heating chip,
after which the chip was heated to 393K at a rate of 10K/min. The electron
beam was blanked during annealing to prevent beam damage. After 2 hours
of annealing at 393K, high resolution HAADF-STEM images were collected
(figure S3.1).

<u>Characterization</u>

A Talos F200X (S)TEM operating at 200 keV was used for imaging and for
scanning transmission electron microscopy – energy dispersive x-ray analy-
sis **(STEM-EDX) analysis**. An aberration-corrected Thermo Scientific Spec-
tra 300 (S)TEM operating at 300 keV was used for high resolution imaging.
TEM samples were prepared by drop-casting a diluted dispersion of NPLs on
200 mesh Formvar/carbon-coated Cu TEM grids (for low resolution measure-
ments), 400 mesh ultra-thin (3 nm) carbon coated Cu TEM grids (high resolu-
tion measurements, or 200 mesh Quantifoil® holey carbon Cu TEM grids (side
view of NPLs). Prior to high resolution measurements, the TEM samples were
treated with ethanol and activated carbon according to a procedure reported
by Li *et al.*[39] The TEM samples were further cleaned by holding the grids in
fumes of boiling acetone and waiting until drops of acetone started to condense
on the grids. The grids were removed from the fumes after 5-10 drops of ace-
tone had condensed and rolled off the grid.

AFM measurements were carried out using a JPK Nanowizard II operating
in intermittent-contact mode in ambient atmosphere. Bruker OTESPA-R3 (26
N/m) or MikroMasch ultrasharp SPM tips (CSC37/No Al, 0.3 N/m) were used
to acquire images with typical set-points of 0.8V. Samples were prepared by
drop-casting or spin-coating 20 µL of a diluted NPL dispersion onto a freshly
cleaved mica surface.

STM/STS measurements were obtained in a Scienta Omicron POLAR SPM
Lab. For the measurements on the $3-6$ QL NPLs the STM was operated at a
base temperature of 4.5K. For the measurements on the 1QL NPLs the STM
was operated at 77K. The base pressure during all experiments was in the 10^{-10}
mbar range. STM samples were prepared by diluting and sonicating the treat-
ed NPL dispersion, after which 10 µL was drop-casted or spin-coated on an
Au(111)/MICA substrate purchased from Phasis. Before measuring, the sample
was annealed in the STM at 393K for 1-2 hours.

Ch.
3

STS spectra were obtained using the following parameters, a 1nA current at -1V was applied before going out of feedback to perform STS. A 10mV bias modulation was applied at 973Hz for the lock-in amplifier and 501 points were obtained at 100ms acquisition time per point.

Adjusted height differential conductance maps were obtained at an in feed-back current of 0.5nA and a speed of approximately 5nm/sec.

S3.2 Modelling of the band structure of Bi$_2$Se$_3$ using a low-energy 8-band model

We use the four–band $\mathbf{k} \cdot \mathbf{p}$ Hamiltonian derived by Zhang *et al.*[27] for describing 3D Bi$_2$Se$_3$ around the 3D Γ point. In the basis (|Bi$^+$, ↑>, |Se, ↑>, |Bi$^+$, ↓>, |Se, ↓>) it has the form

$$H(\boldsymbol{k},k_z) = \epsilon_0(\boldsymbol{k},k_z)\mathbb{I}_{4\times4} + \begin{bmatrix} \mathcal{M}(\boldsymbol{k},k_z) & A_1 k_z & 0 & A_2 k_- \\ A_1 k_z & -\mathcal{M}(\boldsymbol{k},k_z) & A_2 k_- & 0 \\ 0 & A_2 k_+ & \mathcal{M}(\boldsymbol{k},k_z) & -A_1 k_z \\ A_2 k_+ & 0 & -A_1 k_z & -\mathcal{M}(\boldsymbol{k},k_z) \end{bmatrix}$$

where $\mathbf{k}=(k_x,k_y)$ is the in–plane momentum, $\varepsilon_0 (\boldsymbol{k},k_z) = C + D_1 k_z^2 + D_2 \boldsymbol{k}^2$, and $M(\boldsymbol{k},k_z) = M - B_1 k_z^2 - B_2 \boldsymbol{k}^2$. All parameters are fitted from the *ab initio* calculation of ref. *16* and their values are: C = -0.0068 eV, M = 0.28eV, A$_1$ = 0.22eV nm, A$_2$ = 0.41eV nm, B$_1$ = 0.10eV nm², B$_2$ = 0.566eV nm², D$_1$ = 0.013eV nm², and D$_2$ = 0.196eV nm². It is important to note that our model does not take any further inputs, and the models for thin nanosheets will be derived directly from the above 3D bulk model.

The model is solved at the 2D Γ point (k$_x$ = k$_y$ = 0) in a slab geometry via the substitution k$_z$ → i δ_z and hard-wall boundary conditions Ψ(z = ±L$_z$/2) = 0, with L$_z$ the nanosheet thickness. As a result of the confinement in the z-direction we obtain an infinite set of transverse states, which at the 2D Γ point separately describe spin-up and spin-down electrons. Four of these states are surface states whose dispersions at large L$_z$ come in the form of a gapless Dirac cone, but the cone becomes gapped at the small thicknesses of interest as a result of the hybridization between states on the top and bottom surfaces. To obtain an accurate effective Hamiltonian, we project the Hamiltonian at finite k on a subset of these states. We take the four surface bands corresponding to the gapped Dirac cone and also the first set of four bulk bands closest to the Fermi level. The basis is ordered as follows:

$$[\varphi_\uparrow^S \quad \chi_\downarrow^S \quad \varphi_\uparrow^B \quad \chi_\downarrow^B \quad \varphi_\downarrow^S \quad \chi_\uparrow^S \quad \varphi_\downarrow^B \quad \chi_\uparrow^B]$$

where the z-dependent states φ and χ are defined in ref. *49* and the superscripts

S and B refer to the surface and bulk bands, respectively. The resulting Hamiltonian is an 8x8 Hermitian matrix that decouples into two 4x4 subblocks as a combined effect of the time-reversal symmetry (TRS) and the mirror symmetry with respect to the xy-plane. The two subspaces are related by TRS, so here we present the Hamiltonian of only one of them, which reads

$$\begin{bmatrix} H_{SS} & H_{SB} \\ H_{SB}^{\dagger} & H_{BB} \end{bmatrix}$$

Here,

$$H_{II} = \begin{bmatrix} E_0^I - D^I \mathbf{k}^2 + (M^I - B^I \mathbf{k}^2) & A^I k_- \\ A^I k_+ & E_0^I - D^I \mathbf{k}^2 - (M^I - B^I \mathbf{k}^2) \end{bmatrix}, \quad H_{SB} = \begin{bmatrix} ak^2 & bk_- \\ ck_+ & dk^2 \end{bmatrix}$$

where $I = S,B$, $k_{\pm} = k_x \pm ik_y$, and all parameters (E_0^I, D^I, M^I, B^I, A^I, a,b,c,d) depend on the thickness L_z and together encode the topology of the material. As mentioned above, these parameters are derived unambiguously from the initial set of bulk parameters. In previous works only H_{ss} was considered as an effective Hamiltonian for thin films, but we find that this approximation can only describe thicknesses of up to 3 QLs. We observe that for thicker nanosheets of 4, 5, and 6 QLs the bulk bands are required as well to give accurate results.

For the effective 8-band model we calculate the Z_2 invariant ν by counting the number of pairs of zeros of the Pfaffian of the occupied subspace of the time-reversal matrix on a contour that encloses exactly half of our (infinite) Brillouin zone.[14] Since the system has also inversion symmetry, this is the same as computing the product of parities of the Kramers pairs at the time-reversal invariant momenta[40] which in our continuum model are $|k| = 0$ and $|k| = \infty$.

We have also computed the energy spectrum of the 8-band model on a ribbon of 100 nm width. When the Z_2 invariant is nonzero we find states localized at the edges whose dispersion lives in the energy gap and forms a Dirac point with linear dispersion. Due to finite-size effects the states hybridise slightly at the Dirac point and a small gap opens. When the Z_2 invariant is trivial, no edge states are found. In figure S3.5 we show the spectrum for 2 QLs (trivial) to illustrate this.

S3.3 Specifications of the GW-DFT calculations to extract TB parameters and calculate the invariant

Ground state DFT simulations

Density Functional Theory (DFT) calculations were performed on several slabs of Bi_2Se_3, from one to six quintuple layers (QL) using the QuantumESPRESSO software package.[41] Simulations were performed using norm-conserving fully relativistic pseudo-potentials from PseudoDOJO[42] with spin-orbit coupling, and GGA-PBE exchange-correlation functional.[43] The in-plane lattice parameters were optimized for each slab until the maximum force per atom was less than 10^{-6} Ry/Bohr and the components of the stress tensor were below 10^{-4} kBar, within collinear-spin simulations. The separation distance between periodic replicas was 20 Å, and simulations were performed on a 12x12x1 k-point grid with a wave-function kinetic energy cutoff of 140 Ry. Long range van der Waals interactions were included via a Grimme D3 parametrization, but with no three-body interactions.

We investigated the nature of the electronic band structure by projecting each state on each individual atom and then adding the contributions of the atoms belonging to the same quintuple layer. This procedure reveals which electronic states are localized on the surface (*surface states*) or in the interior of the slab (*inner states*) as highlighted, for instance, in the GW band structure of figure 3.6a.

G_0W_0 simulations

The DFT energies obtained with QuantumESPRESSO where corrected using the quasi-particle full frequency G_0W_0 approximation with the Yambo package.[44] The kinetic energy cutoffs were 45 Ha for the G-vectors in the Fast Fourier Transform and 4.250 Ha for the sum in G-vectors in the exchange and correlation self-energy. A total of 180 bands per layer were used in the polarizability while 300 bands per layer were used in the correlation self-energy. The convergence of the sum over empty bands was accelerated by employing a terminator based on the Bruneval-Gonze technique. Finally, a truncation technique was used for the Coulomb potential to minimize the long-range interaction between replicas of the slabs, with the cutoff distance equal to $c - 2$ Bohr, where c is the out-of-plane lattice parameter for each slab.

Extraction of Tight-Binding parameters from G_0W_0 and computation of the topological invariant from DFT and G_0W_0

The DFT ground state calculations were post-processed with the Wannier90[45] package to obtain the Hamiltonian and wave-functions in the maximally localized Wannier function (MLWF) representation. The Wannier wave-functions and Hamiltonian were used to generate the Tight-Binding model Hamiltonian and Wannier charge centers which were then processed with WannierTools[46]

to compute the topological invariant Z_2 on DFT bands. The electronic bands and energies were parametrized up to a 30x30x1 k-point grid to ensure that the bands obtained from the Wannier model match those obtained directly from DFT. Only 30 bands per quintuple layer were parametrized and the window of frozen energies was kept at 1 eV around the Fermi level. The calculation of the Z_2 topological invariant required a very dense k-sampling, depending on the number of QLs. For Bi_2Se_3, 1QL and 2QL a 15x15x1 k-sampling was sufficient to converge Z_2. For 3 to 6QL, however, several hundreds to thousands of k points were needed to achieve convergence of Z_2.

To confirm that the topological properties are preserved after the G_0W_0 corrections of the energy levels, we computed the Z_2 topological invariant for the G_0W_0 energies. We followed the same procedure as in the DFT case, with the same convergence parameter, and processed the G_0W_0 energies with Wannier90 and WannierTools. In both DFT and G_0W_0 cases, the onset of the topological behavior is likely at 4QL.

Ch.
3
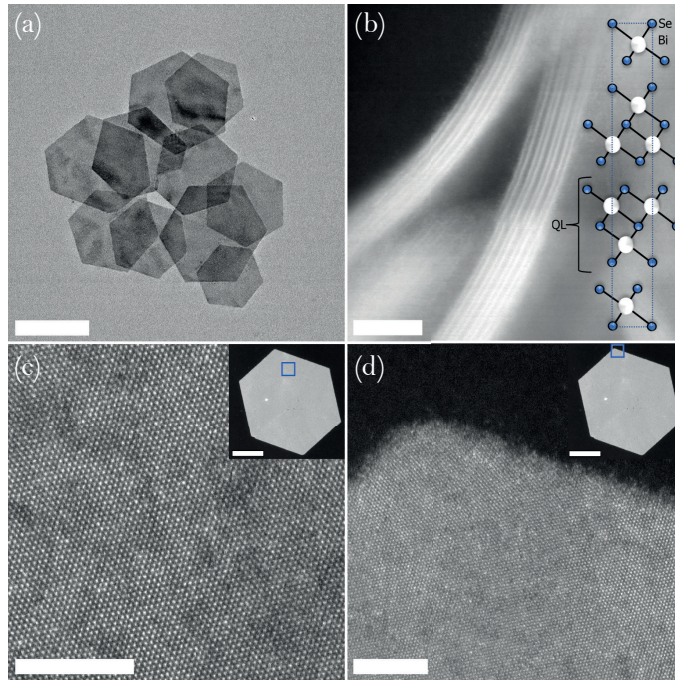
Figure S3.1: Structural characterization of colloidal Bi$_2$Se$_3$ NPLs using TEM and HAADF-STEM.

(a) TEM image of an ensemble of typical Bi$_2$Se$_3$ NPLs. Scalebar is 100nm. **(b)** HAADF-STEM image with the viewing direction along the NPL, showing two NPLs with 3 and 4 QLs, respectively. The two high intensity lines in each QL are due to the Bi columns (see inset). **(c,d)** High resolution HAADF-STEM images showing the high crystalline quality of the NPLs. The blue square in the inset shows the location at which the images were obtained. Scalebar for (b-d) is 5nm and for the insets of (c) and (d) 50nm.
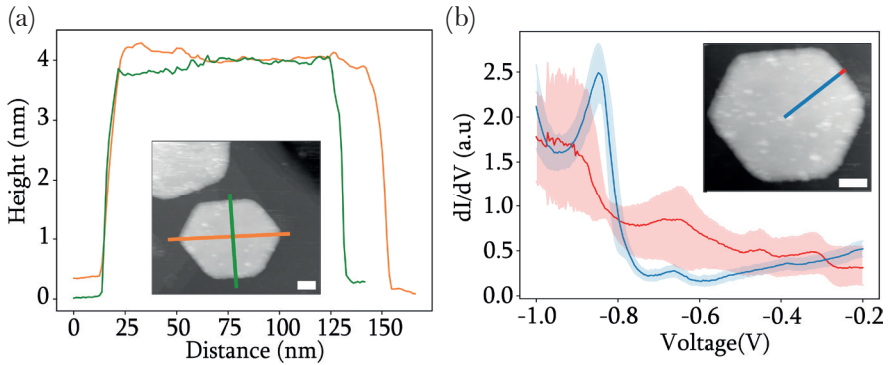
Figure S3.2:   **Characterization of the electronic states of a Bi_2Se_3 platelet, 4 QLs in thickness, in the interior and at the edge, with cryogenic scanning tunneling microscopy and spectroscopy.**

(a) Height profile of a single platelet on a flat Au substrate along the orange and green lines shown in the inset. The diameter of the 2D sheet is about 125 nm. The height profile shows this Bi_2Se_3 platelet consists of 4 quintuple layers (QLs). **(b)** Scanning tunneling spectrum of the local DOS(x,y,E) taken along the blue points (see insert, region of the interior) and the red points (see insert, region of the edge). The set point in the spectroscopy is 1nA. The interior spectrum has been averaged over 25 blue positions; the standard deviation in the DOS is indicated by a blue shade. The red edge spectrum is averaged over the spectra taken at 5 red positions, the standard deviation is indicated by a red gloom. Scalebars are 25nm.

Ch. 3
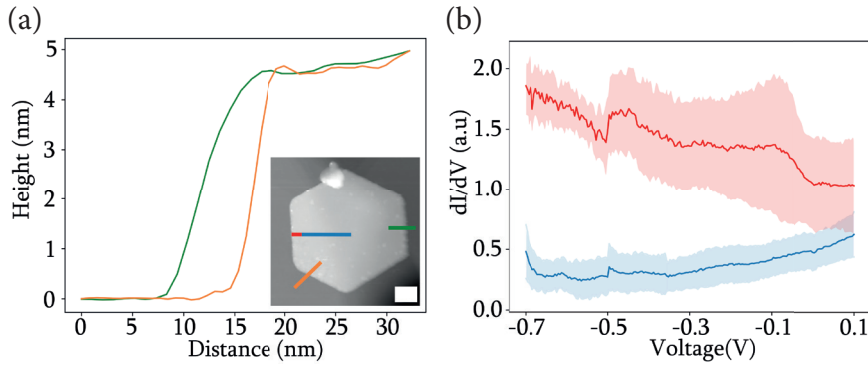
Figure S3.3: Characterization of the electronic states of a Bi$_2$Se$_3$ platelet, 5 QLs in thickness, in the interior and at the edge, with cryogenic scanning tunneling microscopy and spectroscopy.

(a) Height profile of a single platelet shown in the insert. The diameter of the 2D sheet is about 125nm. The height profile shows this Bi$_2$Se$_3$ platelet consists of 5 quintuple layers (QLs). Scalebar is 25nm. **(b)** Scanning tunneling spectrum of the local DOS(x-,y,E) taken along the blue points (see the insert of figure A3.3a, region of the interior) and the red points (see insert of figure A3.3a, region of the edge). The set point in the spectroscopy is 1nA. Mind the different bias range to focus on the area with the increased intensity of the edge. The interior spectrum has been averaged over 20 blue positions; the standard deviation in the DOS is indicated by a blue shade. The red edge spectrum is averaged over the spectra taken at 6 red positions, the standard deviation is indicated by a red gloom.
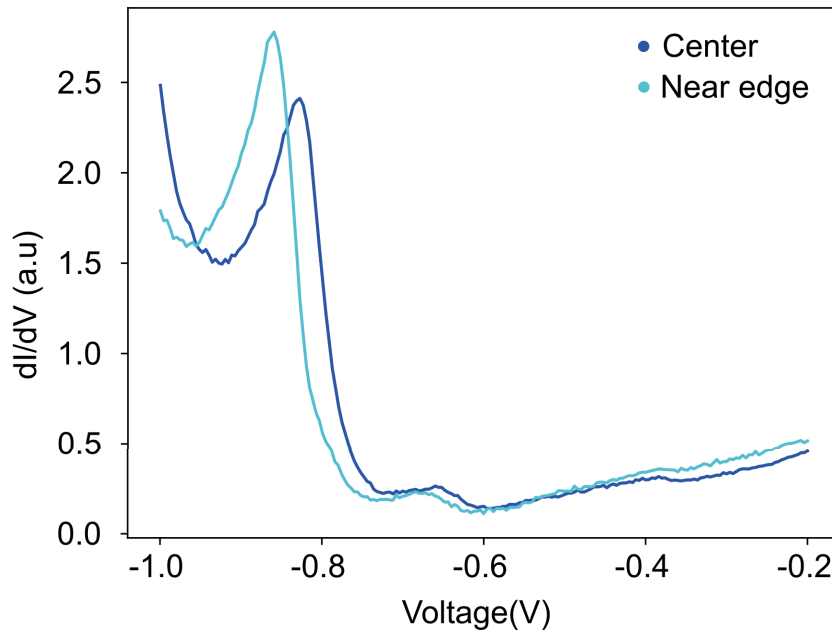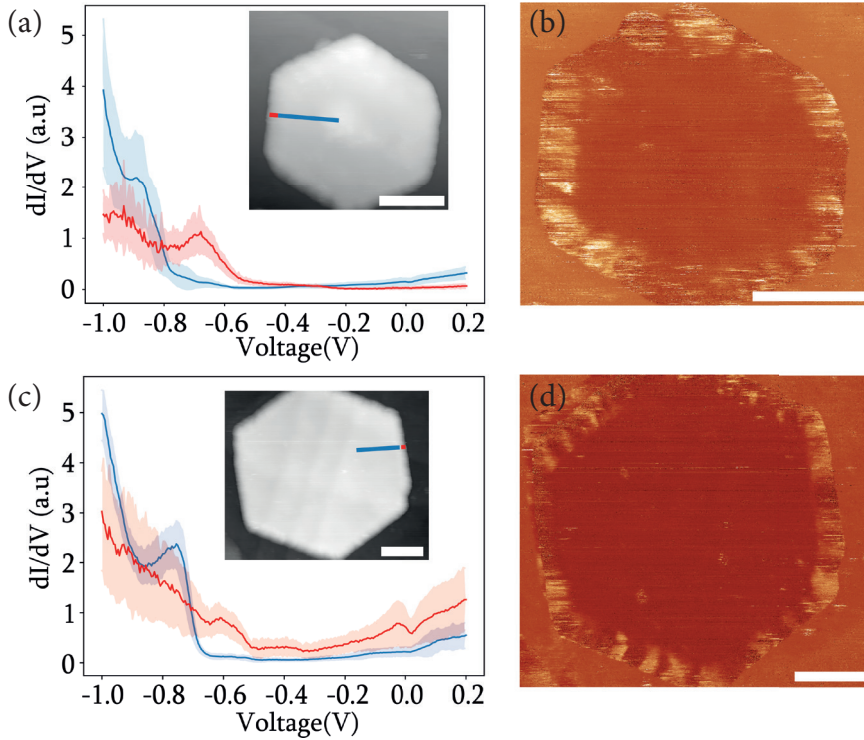
Figure S3.4.: Scanning tunnelling spectrum of the local DOS(x,y,E) taken, on a 5QL thick NPL. The dark blue spectrum is an average of 10 positions in the centre of the interior of the platelet. The light blue spectrum is an average of 3 positions less than 1nm away from the confirmed edge state. The setpoint in the spectroscopy is 1nA

Ch.
3
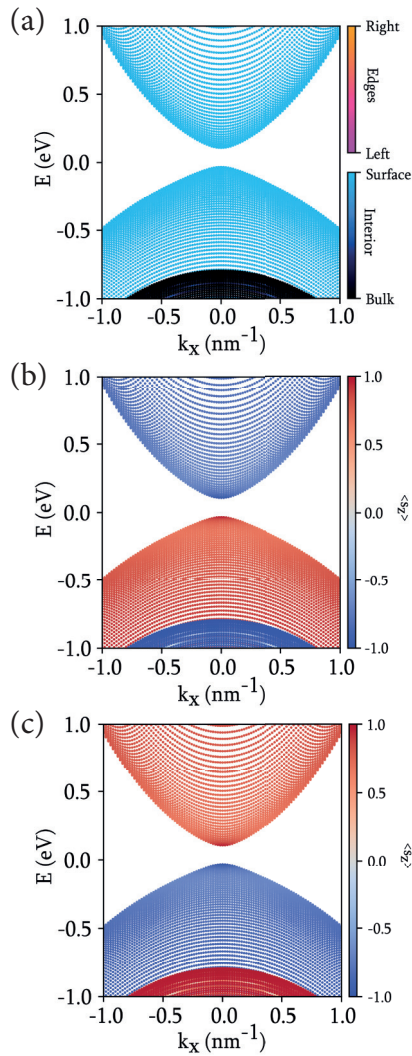
Figure S3.5: **Energy spectrum of a 100 nm wide ribbon of 2 QL thickness as calculated from the 8-band model.**

There are no edge states for this 2QL thick ribbon as the Z$_2$ invariant is trivial. **(a)** The surface–bulk character of the states is identical in the two subspaces. **(b,c)** The spin of both subspaces is reversed as a consequence of TRS.

Ch.
3

Figure S3.6: **Characterization of QSH edge state in two different 3QL thick Bi$_2$Se$_3$ NPLs using STS and LDOS maps.**

(a,c) Averaged scanning tunnelling spectra of the interior (blue) and the edge (red). The blue curve is an average 35 positions on the blue line in the inset for both NPLs. The standard deviation is presented as a blue gloom. The red curve presents an average over 5 positions on the red line for both NPLs. The standard deviation is presented as a red gloom; these spectra represent the edge state. The set point in the spectroscopy is 1nA at –1V. **(b,d)** Differential conductance maps on 3QL NPLs acquired at a bias voltage of –0.4V. Current setpoint at background is 0.5nA. Scalebars are 25nm.

Bibliography

1.   Dang, W., Peng, H., Li, H., Wang, P. & Liu, Z. Epitaxial heterostructures of ultrathin topological insulator nanoplate and graphene. *Nano Lett.* **10**, 2870–2876 (2010).

2.   Hu, X., Rüegg, A. & Fiete, G. A. Topological phases in layered pyrochlore oxide thin films along the [111] direction. *Phys. Rev. B* **86**, 235141 (2012).

3.   Borisova, S., Krumrain, J., Luysberg, M., Mussler, G. & Grützmacher, D. Mode of Growth of Ultrathin Topological insulator Bi$_2$Te$_3$ Films on Si (111) Substrates. *Cryst. Growth Des.* **12**, 6098–6103 (2012).

4.   Park, Y.-S., Lim, J. & Klimov, V. I. Asymmetrically strained quantum dots with non-fluctuating single-dot emission spectra and subthermal room-temperature linewidths. *Nat. Mater.* **18**, 249–255 (2019).

5.   Lhuillier, E. & Guyot-Sionnest, P. Recent progresses in mid infrared nanocrystal optoelectronics. IEEE J. Sel. *Top. Quantum Electron.* **23**, 1–8 (2017).

6.   Wu, K., Li, H. & Klimov, V. I. Tandem luminescent solar concentrators based on engineered quantum dots. *Nat. Photonics* **12**, 105–110 (2018).

7.   Knowles, K. E., Kilburn, T. B., Alzate, D. G., McDowall, S. & Gamelin, D. R. Bright CuInS$_2$/CdS nanocrystal phosphors for high-gain full-spectrum luminescent solar concentrators. *Chem. Commun.* **51**, 9129–9132 (2015).

8.   Qi, X.-L. & Zhang, S.-C. The quantum spin Hall effect and topological insulators. *Phys. Today* **63**, 33–38 (2010).

9.   Klitzing, K. v., Dorda, G. & Pepper, M. New method for high-accuracy determination of the fine-structure constant based on quantized Hall resistance. *Phys. Rev. Lett.* **45**, 494–497 (1980).

10.   Hughes, E. *Electrical and electronic technology. in electrical and electronic technology* 140–145 (Pearson education limited, 2008).

11.   Maciejko, J., Hughes, T. L. & Zhang, S.-C. The quantum spin Hall effect. *Annu. Rev. Condens. Matter Phys.* **2**, 31–53 (2011).

12.   Tsui, D. C., Stormer, H. L. & Gossard, A. C. Two-dimensional magnetotransport in the extreme quantum limit. *Phys. Rev. Lett.* **48**, 1559–1562 (1982).

13.   Schumann, T. *et al.* Observation of the quantum Hall effect in confined films of the three-dimensional Dirac semimetal Cd$_3$As$_2$. *Phys. Rev. Lett.* **120**, 016801 (2018).

14.   Kane, C. L. & Mele, E. J. Quantum spin Hall Effect in graphene. *Phys. Rev. Lett.* **95**, 226801 (2005).

15.   Kane, C. L. & Mele, E. J. Z_2 topological order and the quantum Spin Hall effect. *Phys. Rev. Lett.* **95**, 146802 (2005).

16.   Bernevig, B. A. & Zhang, S.-C. Quantum spin Hall effect. *Phys. Rev. Lett.* **96**, 106802 (2006).

17.   Zhang, H. *et al.* Topological insulators in Bi_2Se_3, Bi_2Te_3 and Sb_2Te_3 with a single Dirac cone on the surface. *Nat. Phys.* **5**, 438–442 (2009).

18.   Lawal, A., Shaari, A., Ahmed, R. & Jarkoni, N. First-principles many-body comparative study of Bi_2Se_3 crystal: A promising candidate for broadband photodetector. *Phys. Lett. A* **381**, 2993–2999 (2017).

19.   Zhang, J. *et al.* Raman Spectroscopy of few-quintuple layer topological insulator Bi_2Se_3 nanoplatelets. *Nano Lett.* **11**, 2407–2414 (2011).

20.   Yazyev, O. V., Kioupakis, E., Moore, J. E. & Louie, S. G. Quasiparticle effects in the bulk and surface-state bands of Bi_2Se_3 and Bi_2Te_3 topological insulators. *Phys. Rev. B* **85**, 161101 (2012).

21.   Yazyev, O. V., Moore, J. E. & Louie, S. G. Spin polarization and transport of Surface States in the Topological Insulators Bi_2Se_3 and Bi_2Te_3 from first principles. *Phys. Rev. Lett.* **105**, 266806 (2010).

22.   Jurczyszyn, M., Sikora, M., Chrobak, M. & Jurczyszyn, L. Studies of surface states in Bi_2Se_3 induced by the BiSe substitution in the crystal subsurface structure. *Appl. Surf. Sci.* **528**, 146978 (2020).

23.   Linder, J., Yokoyama, T. & Sudbø, A. Anomalous finite size effects on surface states in the topological insulator Bi_2Se_3. *Phys. Rev. B* **80**, 205401 (2009).

24.   Romanowich, M. *et al.* Interplay of topological surface and bulk electronic states in Bi_2Se_3. *Phys. Rev. B* **87**, 085310 (2013).

25.   Neupane, M. *et al.* Observation of quantum-tunnelling-modulated spin texture in ultrathin topological insulator Bi_2Se_3 films. *Nat. Commun.* **5**, 3841 (2014).

26.   Chiatti, O. *et al.* 2D layered transport properties from topological insulator Bi_2Se_3 single crystals and micro flakes. *Sci. Rep.* **6**, 27483 (2016).

27.   Zhang, Y. *et al.* Crossover of the three-dimensional topological insulator Bi_2Se_3 to the two-dimensional limit. *Nat. Phys.* **6**, 584–588 (2010).

Ch. 3

28.   Sun, Y. *et al.* Atomically Thick bismuth selenide freestanding single layers achieving enhanced thermoelectric energy harvesting. J. *Am. Chem. Soc.* **134**, 20294–20297 (2012).

29.   Zhang, G., Wang, W., Lu, X. & Li, X. Solvothermal synthesis of V-VI binary and ternary hexagonal platelets: The oriented attachment mechanism. *Cryst. Growth Des.* **9**, 145–150 (2009).

30.   Wei, T. *et al.* A solution synthetic route toward Bi$_2$Se$_3$ layered nano-structures with tunable thickness via weakening precursor reactivity: Bi$_2$Se$_3$ layered nanostructures with tunable thickness. *Phys. Status Solidi A* **210**, 1909–1913 (2013).

31.   Zhang, K. F. *et al.* Strongly compressed Bi(111) bilayer films on Bi$_2$Se$_3$ studied by scanning tunneling microscopy. *Appl. Phys. Lett.* **107**, 121601 (2015).

32.   Zhu, H., Zhou, W. & Yarmoff, J. A. The growth of bismuth on Bi$_2$Se$_3$ and the stability of the first bilayer. *Thin Solid Films* **660,** 343–352 (2018).

33.   De Mello Donega, C. *Nanoparticles: Workhorses of Nanoscience* (Springer Berlin Heidelberg, 2014).

34.   Kaufmann, R. M., Li, D. & Wehefritz-Kaufmann, B. Notes on topological insulators. *Rev. Math. Phys.* **28**, 1630003 (2016).

35.   Baseden, K. A. & Tye, J. W. Introduction to density functional theory: Calculations by hand on the helium atom. *J. Chem. Educ.* **91**, 2116–2123 (2014).

36.   Kurth, S., Marques, M. A. L. & Gross, E. K. U. *Encyclopedia of Condensed Matter Physics.* 395–402 (Elsevier, 2005).

37.   Reining, L. The GW approximation: content, successes and limitations. WIREs *Comput. Mol. Sci.* **8**, (2018).

38.   Xu, S.-Y. *et al.* Unconventional transformation of spin Dirac phase across a topological quantum phase transition. *Nat. Commun.* **6**, 6870 (2015).

39.   Li, C. *et al.* A simple method to clean ligand contamination on TEM grids. Ultramicroscopy 221, 113195 (2021).

40.   Fu, L. & Kane, C. L. Topological insulators with inversion symmetry. *Phys. Rev. B* **76**, 045302 (2007).

41.   Giannozzi, P. *et al.* QUANTUM ESPRESSO: a modular and open-source software project for quantum simulations of materials. *J. Phys. Condens. Matter* **21**, 395502 (2009).

42.   van Setten, M. J. *et al.* The PseudoDojo: Training and grading a 85

element optimized norm-conserving pseudopotential table. *Comput. Phys. Commun.* **226**, 39–54 (2018).

43.   Perdew, J. P., Burke, K. & Ernzerhof, M. Generalized gradient approximation made simple. *Phys. Rev. Lett.* **77**, 3865–3868 (1996).

44.   Sangalli, D. *et al.* Many-body perturbation theory calculations using the yambo code. *J. Phys. Condens. Matter* **31**, 325902 (2019).

45.   Pizzi, G. *et al.* Wannier90 as a community code: new features and applications. *J. Phys. Condens. Matter* **32**, 165902 (2020).

46.   Wu, Q., Zhang, S., Song, H.-F., Troyer, M. & Soluyanov, A. A. WannierTools: An open-source software package for novel topological materials. *Comput. Phys. Commun.* **224**, 405–416 (2018).

Ch.
3

Chapter 4:
The robustness of the QSH edge states in Bi$_2$Se$_3$ NPLs

The quantum spin Hall state present in topological insulators is protected by time-reversal symmetry. This protection should ensure that no backscattering from non-magnetic defects can occur. We investigated the robustness of the edge states of Bi$_2$Se$_3$ nanoplatelets reported in the previous chapter, using STM, STS and LDOS mapping. We examined the influence of structural imperfections in the platelets, the effect of platelets being next to each other or semi-stacked on top of each other. Finally, the impact of magnetic fields up to B = 5T, as well as the deposition of paramagnetic impurities (Mn atoms) was studied.

We find that edge defects, screw dislocations and non-magnetic adsorbates on the edges of the nanoplatelets do not affect the edge state, in agreement with what is expected for a topologically protected edge state. Furthermore, the edge state remains present up to magnetic fields of at least B = 5T. Upon deposition of Mn atoms, the edge state vanishes, suggesting that the topological protection is broken in that case.

"What I think I've been able to do well over the years is play with pain, play with problems, play in all sorts of conditions."
– Roger Federer

Chapter 4: The robustness of the QSH edge states in Bi_2Se_3 NPLs

4.1: Introduction

One of the key reasons for using topological insulators (TIs) for opto-electronics or spintronics is the robustness of the boundary states. This robustness of the quantum spin Hall (QSH) state comes from the protection against backscattering.[1–3] As shown in the previous chapter, colloidally synthesized Bi_2Se_3 nanoplatelets (NPLs) possess a QSH state around the entire circumference of the particle, when the thickness of the platelet is 4 to 6QL. For NPLs with a thickness of 3QL both experimental results as well as theoretical models are not in agreement with one another whether these platelets are trivial or non-trivial.

To determine the robustness of the edge state, multiple different irregularities have been investigated which will be discussed in this chapter. First, structural deformations of individual NPLs will be investigated. Theory dictates that structural defects or adsorbates on top of the edge should not influence the topological edge state.[1,2] The electrons in the channels of the QSH state have a specific spin momentum per channel, so as long as the deformities or adsorbates do not allow the electrons to perform a spin flip, the edge state should remain stable.

Secondly, it will be investigated how the QSH state is influenced when two platelets are adjacent to each other or even when two platelets are semi-stacked. When the thickness of the platelets decreases below 7QL it has been shown that wavefunctions of the top and bottom surface state of the TI start to hybridize which turns the 3D TI into the 2D TI, resulting in a helical state at the edges.[4,5] When two platelets are semi-stacked or in very close proximity of each other, the wavefunctions might influence each other as well. Additionally, when two platelets are semi-stacked a part of the crystal is bend due to the height difference between platelet and substrate, which causes strain. It has been shown that strain can tune the Dirac point energy and bandgap, and even break the QSH state in Bi_2Se_3.[6–8]

Lastly, the effect of magnetic fields and deposition of (para)magnetic atoms will be investigated. A perpendicular magnetic field breaks time-reversal symmetry (TRS), consequently, the edge states should no longer be protected.[9,10] We examined the robustness of the edge state by recording spatially resolved dI/dV spectra with and without a magnetic field of $B = 5$ Tesla in the perpendicular direction. Additionally, the influence of a different method to induce a spin-flip in the electrons will be tested, namely the deposition of magnetic adsorbates on the nanoplatelets. These magnetic adsorbates should act differently to the adsorbates previously discussed as these adsorbates break the TRS protection and therefore it is allowed for electrons to flip their spin.[1]

Determining the robustness of the QSH edge state by investigating these different situations will show in which environments the edge states of these crystals could potentially be used.

4.2: Theory

4.2.1: Time-reversal symmetry

Landau theory states that a stable phase of matter is characterized by a local order parameter.[11,12] When there is order, this parameter is nonzero but becomes zero following a phase transition to a disordered state. For example, if one considers a gas, it has a continuous translational symmetry which is broken when a solid is formed, the order parameter in this case is the density, which changes rapidly at a critical temperature. Upon the discovery of topological insulators this theory was no longer sufficient and a new order parameter was needed to describe when a material is in a topological phase or when it is in a trivial state, this is the Z_2 invariant, introduced by Kane and Mele.[13]

Z_2 topological insulators are protected by time reversal symmetry (TRS). This means that when time is reversed the laws of physics are still the same. For a Quantum Spin Hall (QSH) phase this symmetry can be intuitively understood when thinking about the two channels hosting spin up and spin down electrons respectively (see figure 4.1). When time would be reversed the electrons would flow in the opposite direction which would mean that the physics is different. However the channels consist of two streams of electrons with opposite spin, the situation i.e. the helical edge state, is unchanged as both streams move in opposite directions and both spin as well as linear momentum of each state are reversed.
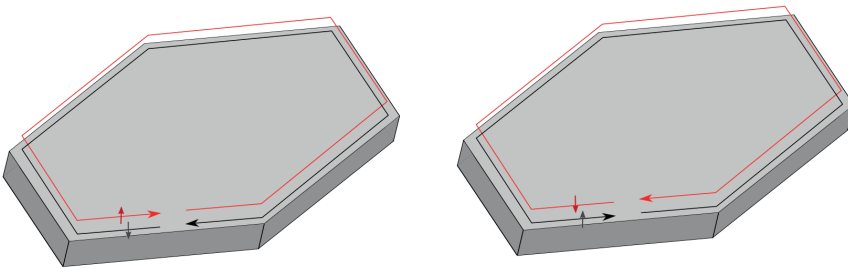
Figure 4.1: **Schematic representation of the quantum spin Hall effect on a hexagonal platelet displaying time reversal symmetry, with reversed spin and linear momentum of each state.**

Ch.
4

The QSH state can potentially be broken by applying a sufficiently large external magnetic field perpendicular to the 2D plane, as well as by magnetic defects in the material.[9,10,14,15] A perpendicular magnetic field could break TRS for such a system due to the Zeeman effect, as the spin up and spin down electrons can get different energies. However this effect is small and it is more likely that the inverted bandgap is closed due to the magnetic field or that backscattering is enhanced.[10,16,17] A second effect is the Lorentz force, which can change the trajectory of the electron channels and change the intrinsic energy of each of the two helical states.[2] Magnetic defects would be able to break TRS by enhancing the backscattering of the electrons in the edge state. By enhancing the backscattering the spin-momentum locking will be broken and no spin specific channels will be present at the edge of the crystal.[14,17]

4.3: Results and discussion

4.3.1: Structural anomalies

Theoretically, as long as structural imperfections do not break TRS, they should not affect the QSH state present at the edges.[1,2] Multiple NPLs of various thicknesses in the range of 3 to 6 QLs with non-hexagonal shape or with other types of anomalies have been investigated using STM, STS and differential conductance mapping. This last technique is especially important as it directly reveals the spatial extent of the edge state. Figure 4.2 shows constant current images and differential conductance maps of three different platelets (3,4 and 6 QL respectively) with different structural irregularities. In figure 4.2a an NPL can be seen in which the bottom part of the platelet is 'dirty', i.e. the STM topography shows clear height variations. The height varies by approximately 0.5 nm, i.e. less than a QL. We cannot determine the origin of the irregularities. Options include adsorbates on the surface, local strain induced by the presence of adsorbates underneath the platelets, chemical/structural defects formed during the synthesis and/or annealing of the platelets. The LDOS map, at -0.4V, of figure 4.2b shows the familiar continuous edge state. Hence, the edge is robust with respect to these imperfections. A clear band is visible around the entire circumference of the crystal, with a width of 8nm. The STS data, shown in figure 3.7a of the previous chapter, is comparable to that of a nanoplatelet without these defects.

The TEM image shown in figure S4.1 demonstrates that the majority of the synthesized crystals have a well-defined hexagonal or trigonal shape with straight edges. There are however also NPLs with a more irregular shape which leads a different edge termination and therefore to curved edges (figure 4.2b). The LDOS map of figure 4.2d however shows that the edge state is continuous around the curve in the edge, demonstrating that this structural

difference has no effect on the QSH state.

Lastly, a 6QL thick nanoplatelet (as measured on the bottom left edge) with a screw dislocation was studied, see figure 4.2e. This defect causes an additional edge going from the location of the screw dislocation outwards to the edge of the crystal. The differential conductance map (figure 4.2f) shows that the state, observed at the edge of the crystal, propagates along the dislocation to the interior of the nanoplatelet. The height variation due to the screw dislocation corresponds to 1QL. It can therefore be concluded that this edge still behaves as an edge of 6QL crystal and not as a 1QL edge as it has been shown in previous chapter that 1QL Bi_2Se_3 NPLs are not topological insulators. Furthermore, it can be seen that the QSH edge state of the entire crystal on the outer edges has not changed even at the connection of the screw dislocated edge in the top right corner of the crystal. The STS data acquired at the screw dislocation on this nanoplatelet, is very similar to those reported for areas on this crystal, away from the screw dislocation (c.f. figure S4.2 and figure 3.3h of previous chapter)

From these measurements it can thus be concluded that the edge state is indeed robust against the studied structural anomalies. It has been shown that unknown adsorbed molecules on the edges, edge defects and screw dislocations do not have a significant effect on the state. This coincides with theory about the TRS protection of topological insulators as most structural irregularities do not break the protective symmetry.

4.3.2 Influence of adjacent and semi-stacked NPLs on the QSH state

Apart from structural anomalies, there are more situations in which the existence of a QSH state is not trivial. The dispersion of Bi_2Se_3 NPLs in ethanol is drop-cast onto gold on Mica, creating a random distribution on the gold surface. Depending on the concentration of the particles in the dispersion, there is a certain chance that two or more crystals end up next to each other, on top of one another, or fuse together during post synthesis annealing. These situations can cause strain on the Bi_2Se_3 crystal lattice or influence the QSH state in other ways.[6–8] In figure 4.3a and c there are two constant current images shown in which half of a nanoplatelet is laying on top of another nanoplatelet, which we refer to as semi-stacking. All four platelets have a thickness of ~3nm (3QL each) with respect to the background but the overlapping part of the two platelets has a thickness of ~6nm with respect to the background, see figures 4.3b and 4.3d. The line trace in Fig. S4.4 demonstrates that the height increase occurs over a range of ~10nm. It can therefore be concluded that these platelets are quite flexible in their structure. This poses the question what happens to the edge states at the overlapping part: will this area act as a 6QL thick platelet, will the
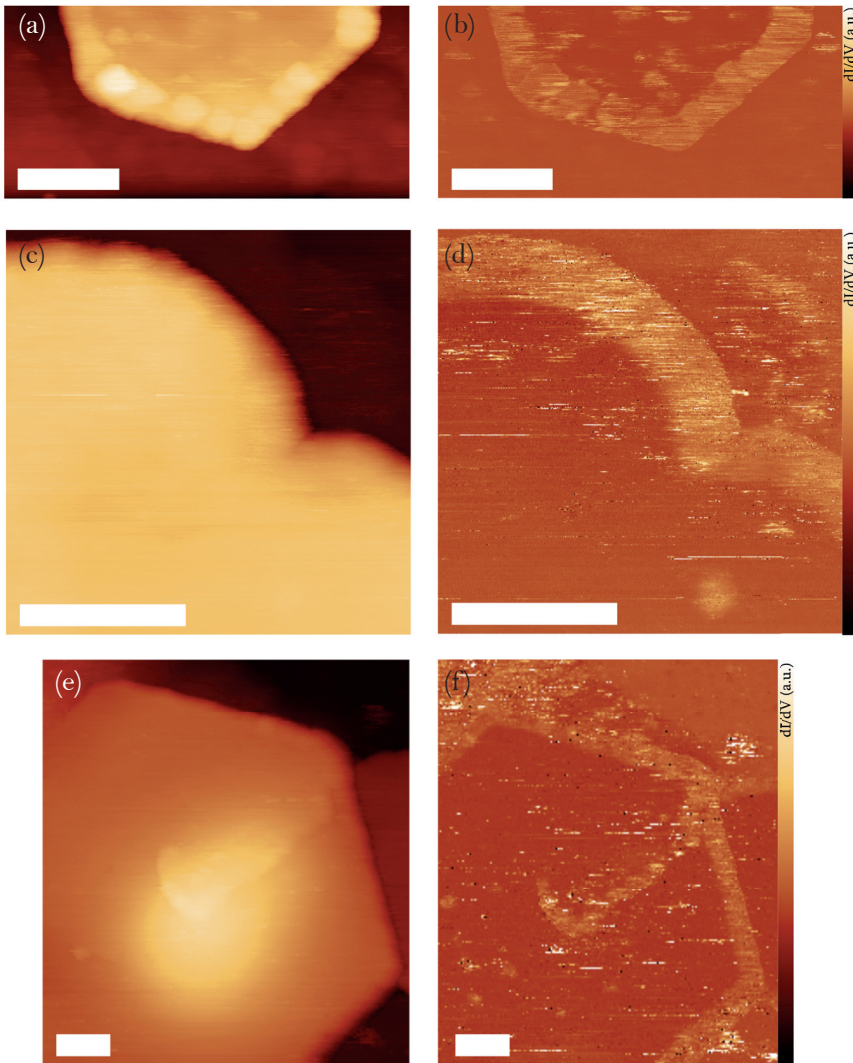
Figure 4.2: **Structural irregularities in Bi$_2$Se$_3$ nanoplatelets with a thickness of 3QL (a,b), 4QL (c,d) and 6QL (e,f), characterized with scanning tunnelling microscopy and LDOS mapping.**
(a,c,e) Constant height images of NPLs with thickness 3,4 and 6 QL respectively showing an edge with unknown adsorbed molecules on the edge (a), a nonlinear edge (c) and a screw dislocation in the middle of the platelet (e). **(b,d,f)** LDOS(x,y) maps at -0.4V displaying the QSH edge state being unchanged by the structural anomalies. Scalebars are 25nm.

edge state remain intact, or will the edge states be broken due to strain?

As shown in the previous chapter, nanoplatelets with a thickness of 3QL do not always possess a well‑defined continuous state around the edges of the crystal. The LDOS map at $V = -0.4$V, figure 4.3e, shows intensity all throughout the platelet. The interior of both the upper and lower nanoplatelet show significant intensity variations, while a more continuous band is seen along the edges. Note that this band is also observed for the part of the platelet that lies on top of the bottom platelet. Differential conductance spectra acquired on the platelet at the top of the image are in agreement with previous findings, see figure S4.3.

Interestingly, there is quite some intensity visible on the interior of both plate‑lets. For the top NPL the raised intensity seems to be mainly at the part of the platelet that is on top of the other NPL, suggesting that perhaps the strain caused by the stacking of part of the platelet influences the states in the interi‑or. However, the bottom platelet also shows significant intensity variations in the interior, even though it lies flat on the substrate.

An LDOS map of the second set of stacked platelets is shown in figure 4.3f. This stack of platelets shows different behaviour to the previous stack. Throughout both platelets there is no evidence of a QSH edge state nor of a state in the interior of the crystals. Both of the platelets of this stack are 3QL in thickness which could mean that no pronounced QSH state is available for either of the platelets and therefore the stacking does not influence the overall DOS. It can however be concluded that the overlapping part of the platelets does not behave as a 6QL NPL as a platelet of this thickness would exhibit a clear edge state. These two datasets on semi‑stacked NPLs, suggest that stacking platelets of 3QLs does not have a dramatic influence on their electronic properties (edge states do not suddenly appear or disappear). However, these experiments should be repeated for thicker nanoplatelets that exhibit a clear edge state.

(Semi)‑stacking is not the only configuration possible after the dispersion is drop‑cast on the gold on mica substrate, it could happen that two (or more) NPLs end up adjacent to each other. In these situations, the edge states of different platelets can potentially couple and hybridize. A scanning tunnelling topographic image of such an occurrence can be seen in figure 4.4a, with a larger 4QL thick platelet next to a smaller 3QL thick platelet. Both NPLs show the well‑defined hexagonal shape without any overlap as was seen in figure 4.3. Figure 4.4b shows a line trace on the gap between the two nanocrystals as drawn in figure 4.4a, despite the line trace not going to 0 nm it is believed that these two NPLs have not fused together. Due to the STM tip with finite aspect ratio in combination with the parameters of the scan image the depth of the gap might be underestimated.

Ch.
4
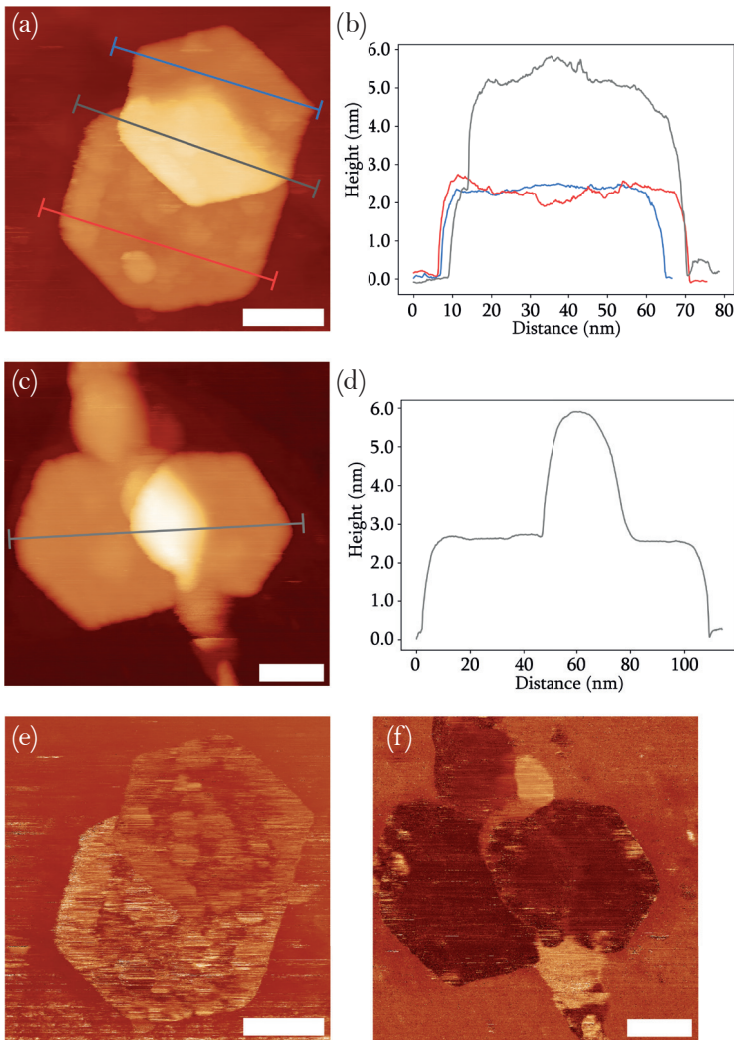
Figure 4.3: **Influence of semi-stacking on the QSH state in two stacks of two 3QL thick Bi_2Se_3 NPLs**

(a) Constant current image of two partially overlapping NPLs. **(b)** Line traces on the platelets of (a) showing a ~2.5nm thickness corresponding to 3QL and a ~5.5nm thickness at the overlapping area. **(c)** Constant current image of two partially overlapping NPLs. Including some 'dirt' above and below the stacked NPLs. **(d)** Line trace on the overlapping platelets of (c) showing ~2.5nm in thickness for a single NPL, corresponding to 3QL, and ~6.0nm in thickness at the overlapping area. **(e)** LDOS(x,y) map at -0.4V on the stack of (a) showing a resemblance of the QSH edge state as well as states in the interior of both platelets. **(f)** LDOS(x,y) map at -0.4V on the stack of (c) showing no QSH edge state. Scalebars are 25nm.

Figure 4.4c shows STS data on the 4QL and 3QL thick platelets. The difference between the averaged spectra on the interior and the edge for both crystals is limited. The clear difference between the interior and edge spectra previously seen for NPLs with a 4QL thickness is absent although the averaged spectra on the edge do show some increased DOS in small areas of the bandgap region. As NPLs with a thickness of 3QLs do not always have a continuous edge state, no conclusions can be drawn from these STS results. A differential conductance map at –0.4V is shown in figure 4.4d. The QSH edge state for the 4QL thick NPL can be seen and is reasonably well-defined, however at the area adjacent to the 3QL thick NPL, the intensity of the edge state seems to have been diminished. Notably, this is not the only region in which the intensity of the LDOS map is lower at the edges of the platelet. One possible reason for this could be residual magnetic material present on the 4QL thick platelet. Please note that, a project prior to this research used Mn adsorbates in the STM and therefore traces of Mn could have remained in the system and therefore involuntarily be introduced to the NPLs. Further investigation on the effect of magnetic adsorbates on the QSH state will be discussed later in this chapter. For the smaller 3QL thick NPL no trace of the edge state can be seen. As can be seen in figure 3.7d of previous chapter, platelets with a thickness of 3QL usually do show some residual traces of the QSH edge state which is completely absent in figure 4.4d. A potential explanation would be that the edge states of the two NPLs hybridize, leading to an energy shift.

In figure 4.5 STM data is shown on a set of platelets with thicknesses of 6QL and 4QL respectively, both of which should have a well-defined QSH edge state. The topographic image in figure 4.5a shows a well-defined hexagonal shape for the 6QL thick NPL (left). The shape of the 4QL thick NPL (right) is less well-defined however it can be seen at the bottom where the two particles meet that the edge crossed into the larger particle. It is therefore concluded that there is no discernible gap between the platelets and the platelets have fused together. The fusion of these particles could have occurred at two steps in the process, during synthesis (see figure S4.4) or during the annealing procedure.[18] The *dI/dV* spectrum in figure 4.5b shows an averaged spectrum of the interior (along the green line in figure 4.5a) and the fused edge of the 6QL NPL (along the orange line in figure 4.5a). The presence of the QSH state can be seen, similar to the acquired *dI/dV* spectra shown in figure 3.3h of the previous chapter.

Figure 4.5c shows STS data on the 4QL thick NPL (with exact locations of spectra shown in figure 4.5a); averaged spectra representative of the interior of the platelet are shown in blue, while spectra of the edge are given in red. Again the data is in excellent agreement with the previously reported *dI/dV* spectra of NPLs with a thickness of 4QL: a peak at $V = $ –0.85V in the interior which is

Ch.
**4**
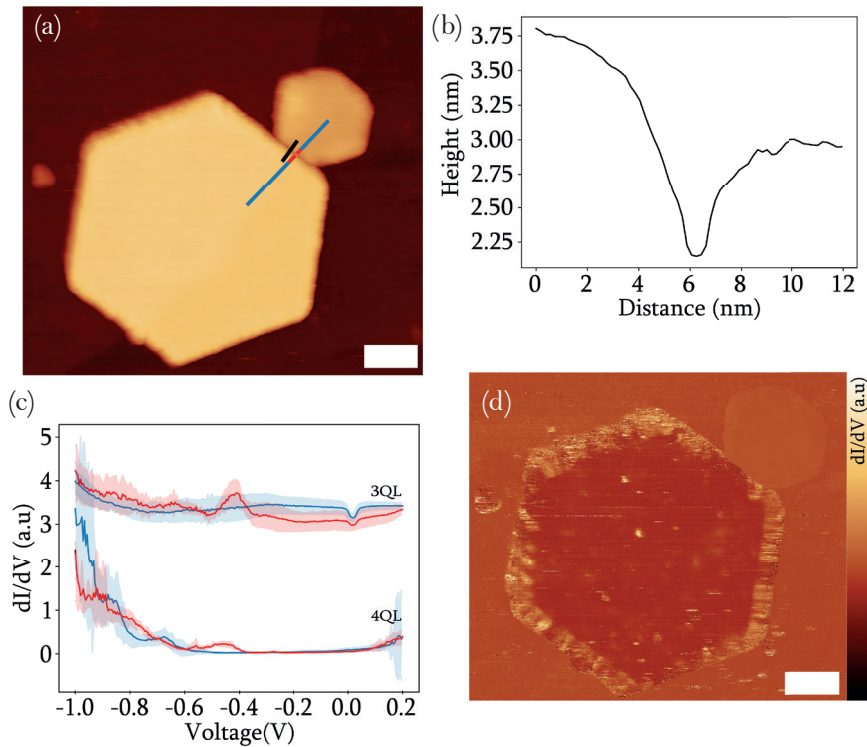
Figure 4.4:   **Influence of minimal separation between two adjacent Bi$_2$Se$_3$ NPLs on the QSH state.**
(a) Constant current topographic image of two Bi$_2$Se$_3$ NPLs laying adjacent on the substrate. **(b)** Height trace as shown in (a) displaying a gap between the two particles. **(c)** Averaged scanning tunnelling spectra on the interior (blue, 25 averages) and on the edge (red, 5 averages) of a 4QL thick NPL and of the interior (blue, 17 averages) and the edge (red, 4 averages) of the adjacent 3QL NPL. The averaged spectra have been offset for clarity purposes. **(d)** LDOS(x,y) map at -0.4V on the two adjacent NPLs showing a reasonably well-defined QSH edge state for the 4QL thick NPL but not for the 3QL thick NPL. Note the perturbations of the QSH edge state of the 4QL platelet, especially at the contact region with the 3QL thick platelet. Scalebars are 25nm.

absent in the averaged spectra on the edge, and a heightened DOS in the band-gap region for spectra taken on the edge of the crystal in comparison to the interior, as seen in figure 3.3g. The average differential conductance data on the edge of this platelet that is fused to the 6QL thick platelet, however shows a different behaviour (black). The spectrum at this edge is more reminiscent of spectra taken in the interior: a peak V = -0.85V, as well as a lower intensity in

the bandgap region. The differential conductance map of figure 4.5d confirms that indeed the edge state in this region of the 4QL thick platelet has disappeared while the edge state on the 6QL thick NPL is still present at the fused edge. This appears to be a similar situation to the screw dislocation discussed before, the higher "edge" still acts as a 2D TI with a QSH state.

Ch.
4
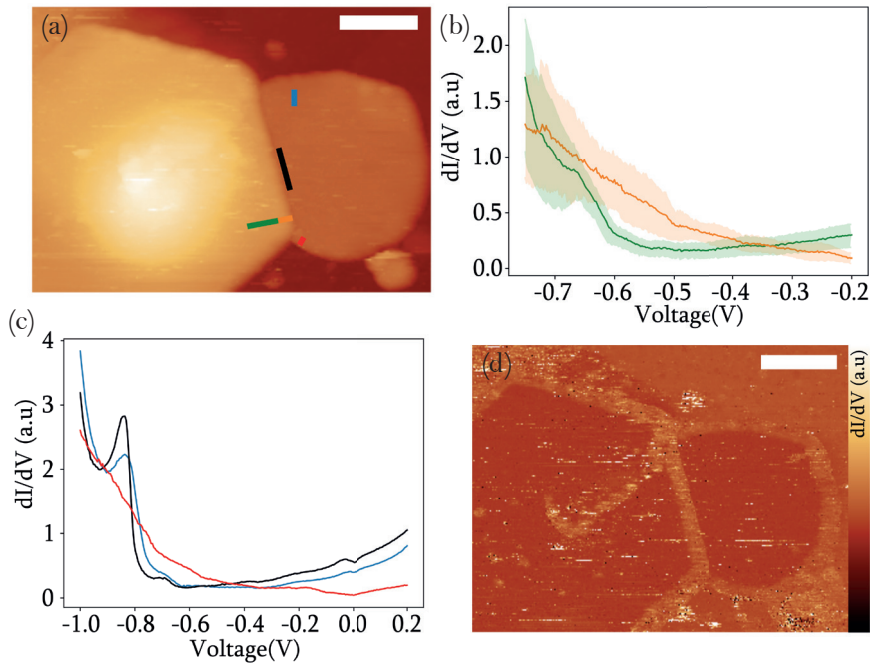
Figure 4.5: **Influence of the fusion of two Bi$_2$Se$_3$ NPLs on the QSH edge state**
(a) Constant current topographic image of a 6QL thick NPL (left) and a 4QL thick NPL fused together. **(b)** Averaged scanning tunnelling spectra on the interior (green, 15 averages) and on the edge (orange, 7 averages) of the 6QL thick NPL. **(c)** Averaged scanning tunnelling spectra on the 4QL thick NPL taken in the interior (blue, 10 averages), at an outer edge (red, 7 averages) and at the edge fused to the thicker (6QL) NPL (black, 20 averages). **(d)** LDOS(x,y) map at $V = -0.4$V on the fused NPLs showing well-defined QSH edge states for the 6QL thick NPL as well as for the outer edges of the 4QL NPL but not on the fused edge of the 4QL NPL to the 6QL NPL. Scalebars are 50nm.

Due to limited experimental results on fused or adjacent NPLs, it is difficult to draw conclusions. In both cases studied, there are indications that the edge state is affected by other nearby platelets. With the NPLs adjacent to each other showing indications of hybridization between the edge states of the two platelets whereas the fused particle shows behaviour of a single particle with the thinner NPL no longer having an edge state at the fused edge.

4.3.3 Effects of magnetic field and paramagnetic atoms

It has been theorized that time reversal symmetry protection makes the QSH state very robust as the electrons in the state would have to undergo a spin flip in order to be (back)scattered. It is predicted that this protection can be broken by applying a perpendicular magnetic field.[2,9,10,19] The applied perpendicular magnetic field could have four effects on the electrons in the QSH state, (i) Zeeman splitting, (ii) a splitting of the states in the edge by Lorentz force, (iii) the closing of the bulk gap and (iv) enhanced backscattering by defects in the NPLs.[10,15,17] The Zeeman effect has been shown to be minimal for these kinds of systems due to their relatively small g-factor, with Zhang *et al.* estimating a required perpendicular magnetic field of more than $B =100$T for HgTe and InAs/GaSb.[2,10] It is however unclear what strength of magnetic field is needed for the Lorentz force to open a subgap in the edge state or for the gap to close in the bulk of Bi$_2$Se$_3$ nanoplatelets. There are however some papers showing both theoretically and experimentally that a field up to $B =12$T is not enough to break the QSH edge state in HgTe, InAs/GaSb and HgTe/CdTe quantum wells.[9,10,15,17,20]

Figure 4.6 shows differential conductance maps of two different Bi$_2$Se$_3$ nano-platelets with a thickness of 3QL taken without an applied magnetic field as well as in a $B = 5$T perpendicular magnetic field. These LDOS maps are taken at $V = $ -0.4V in energy as this is inside of the bandgap region for these Bi$_2$Se$_3$ NPLs. Previously, it was shown that the edge state is often not well defined for NPLs with a thickness of 3QL. Hence, it could be hypothesized that this edge state is more susceptible to magnetic fields.

Figures 4.6a and 4.6c show differential conductance maps taken without an applied magnetic field. The NPL shown in figure 4.6a does not display a well-defined QSH edge state whereas the NPL shown in figure 4.6c does show a full band around the entire circumference of the crystal. In figures 3.7a and S3.6a of previous chapter, the STS data for both of these platelets without an applied magnetic field are shown.

A $B = 5$T perpendicular magnetic field was applied and another set of differential conductance maps was acquired at a bias voltage of $V = $ -0.4V. Figure 4.6b

shows the nature of the QSH edge state for the platelet which did not show a well-defined state but rather patches of the remainder of the state. Upon first inspection, the spatial distribution appears similar, however, there are small changes, most prominently on the edge on the left hand side. The map without applied magnetic field shows a rather uniform band, while the state seems more patchy at $B = 5$T. Another difference is that the intensity profile of the edge state itself is approximately uniform without magnetic field, while in the magnetic field the intensity more gradually decays from the edge towards the centre. The corresponding STS data is shown in figure S4.5.

Figure 4.6d displays a *dI/dV* map of the second 3QL thick platelet at -0.4V in energy which shows different behaviour than the edge state in the first platelet. With the edge state now well-defined without an applied magnetic field, the 5T perpendicular magnetic field doesn't seem to have any measurable effect on the intensity of the state.

From these measurements the following conclusions can be drawn. The edge state of colloidal Bi_2Se_3 nanoplatelets are robust in a perpendicular magnetic field up to $B = 5$T. In both experiments, the edge state is still measurable. However, some effect of further breaking of the state appears to be visible when the QSH state is already ill defined. This leads to the hypothesis that a higher magnetic field will break the QSH state as shown before by Du *et al.*[20]

Ch. 4
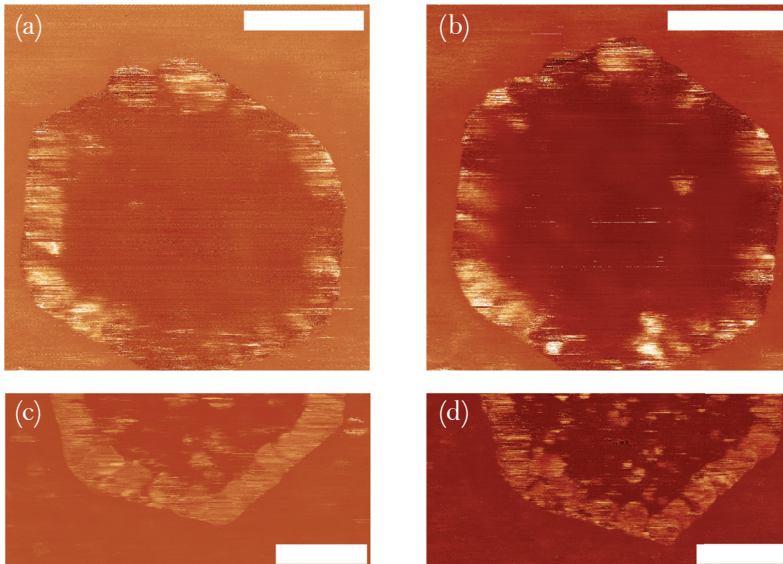
Figure 4.6:   **LDOS(x,y) maps of two different Bi_2Se_3 NPLs with a thickness of 3QL at V = -0.4V without magnetic field (a,c) and with a $B = 5$T perpendicular magnetic field (b,d). Scalebars are 50nm.**

A different method to influence the QSH edge state is by depositing paramagnetic impurities onto the surface of the NPLs. When the spin-momentum locked electrons in the edge state encounter such a paramagnetic defect, rather than going around the defect like it normally would, the electron can flip its spin and be backscattered. This enhanced backscattering by paramagnetic impurites is a breaking of the TRS protection. To test this theory, manganese (Mn) atoms were evaporated onto the sample in various amounts. Due to the size of the NPLs as well as the inherent amount of adsorbed particles, it is not possible to distinguish the individual adsorbates on the platelets. In the supporting information it is described how Mn atoms were evaporated onto the surface and how the coverage was estimated.

In figure 4.7 the characterization of the QSH state is shown after two evaporation cycles of Mn, with the second evaporation cycle roughly 10 times the amount of material evaporated as the first cycle. This resulted in a coverage of approximately 60 cluster per 100nm^2, for the first evaporation cycle, as shown in figure S4.6. The averaged dI/dV spectra in figure 4.7a were taken on a 4QL thick Bi$_2$Se$_3$ nanoplatelet after the deposition of manganese. The spectrum shows differences to the data on the Mn-free platelets of this thickness (see chapter 3). First, in the averaged spectrum taken on the edge, the standard deviation is very large in the energy region between $V = $ -0.9V and -0.5V. This indicates that there are significant differences in the energy landscape between every individual spectrum, with the distance between each spectrum being ~1nm. Secondly, the density of states in the bandgap region(between $V = $ -0.8V and -0.2V) shows a different behaviour than previously seen. Between $V = $ -0.8V and -0.5V there seems to be an increase in DOS when measuring at the edge in comparison to the interior, despite the large standard deviation. This increase in DOS suggests the presence of an edge state, however between $V = $ -0.5V and -0.2V the increase in DOS at the edge is minimal. Lastly, the DOS at the onset of the conduction band ($V > 0.0$V) at the edge shows a higher intensity than in the interior, but also with a rather large standard deviation.

The differential conductance map at $V = $ -0.4V (figure 4.7b) shows the extend of the differences between the well-defined QSH edge state previously measured and the QSH state affected by the paramagnetic manganese adsorbates. The clear band of higher intensity before evaporation of Mn, on a 4QL thick NPL, has disappeared and has been replaced by patches of varying intensity. This is consistent with the large standard deviation in the STS data as well as with the lack of states in the bandgap region. To verify whether this effect originates from the paramagnetic adsorbates, more Mn was evaporated at the same evaporation rate as before but for ten times as long. This should lead to ten times the amount of manganese on the surface of the NPL. The differential conductance map of a 5QL platelet shown in figure 4.7c does not show any indications of an edge state. This is in stark contrast to the experimental and
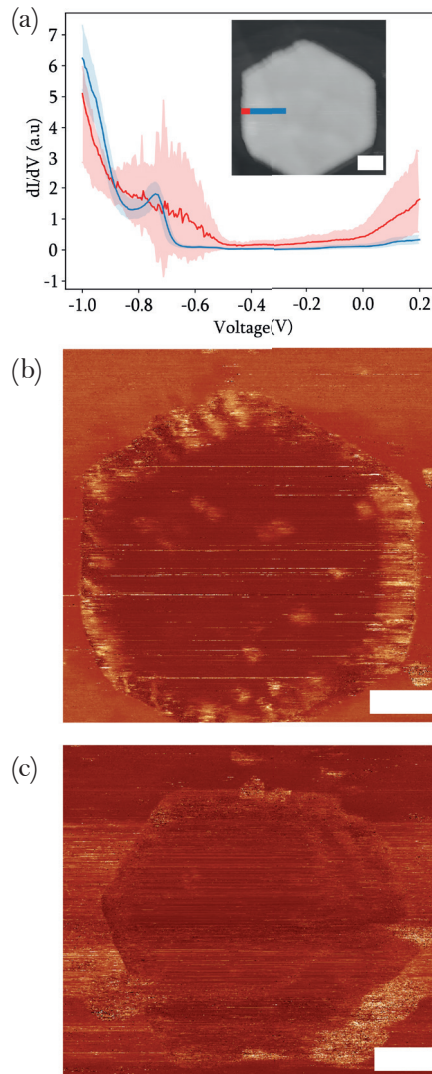
Figure 4.7: **Characterization of QSH edge state after evaporation of Mn.**
(a) Averaged scanning tunnelling spectrum on the interior and on the edge of a NPL with a thickness of 4QL after evaporation of Mn. The blue curve is an average of 30 positions on the blue line in the inset. The standard deviation is presented as a blue gloom. The red curve presents an average over 7 positions on the red line. The standard deviation is presented as a red gloom; these spectra represent the edge state. **(b)** LDOS map on 4QL NPL acquired at a bias voltage of -0.4V. **(c)** LDOS map of an NPL with a thickness of 5QL after evaporation of 10 times the amount of Mn in comparison to (a,b) acquired at a bias voltage of -0.4V. Scalebars are 25nm.

Ch.
4

theoretical data discussed in chapter 3. Hence, we conclude that deposition of Mn atoms on Bi_2Se_3 NPLs does break the TRS, which leads to enhanced backscattering of the electrons in the edge state. This leads to a conversion of the Bi_2Se_3 platelet from a QSH insulator into a trivial insulator

4.4 Conclusion and outlook

The robustness of the QSH state in 2D Bi_2Se_3 nanoplatelets hinges on time reversal symmetry. Therefore, the state should not be affected by structural defects but a sufficiently strong magnetic field, as well as magnetic impurities are expected to influence the edge state. We examined the effects of structural irregularities, neighbouring nanoplatelets, magnetic fields and paramagnetic adsorbates using STM/STS and LDOS maps.

Structural anomalies in the colloidally synthesizes particles are not uncommon. Examples include imperfections at the edge (kinks, structural defects) and in the bulk (screw dislocation). None of these three imperfections had a significant effect on the edge state. The screw dislocation acted as an additional edge which could hamper the transport of the electrons in the QSH state but transport measurements would have to determine the exact behaviour of electrons in well-defined hexagonal platelets and platelets with structural anomalies.

Stacking of crystals as well as platelets adjacent to each other exhibit interesting behaviour on the QSH state. Two semi-stacked platelets were investigated with one of the stacks showing no clear signs of the presence of the QSH edge state whereas the other stack shows increased intensity over both of the crystals on the edge as well as on the interior. Both aggregation of two NPLs as well as two NPLs being sufficiently close to each other seems to hybridize the QSH edge state although due to limited experimental results, no hard conclusions can be drawn.

We found that a perpendicular magnetic field of $B = 5T$ did not significantly affect the edge state. In contrast, the deposition of paramagnetic manganese atoms on the Bi_2Se_3 nanoplatelets resulted in the disappearance of the edge state. In lower quantities the paramagnetic adsorbates seems to break the TRS protection, with the edge state no longer being a continuous band but only showing localized patches of the QSH state. Higher quantities of Mn adsorbed on the surface even leads to the full disappearance of the QSH state, in agreement with the theory that the electrons in the edge state can be (back)scattered by paramagnetic impurities.

In conclusion, the edge state of colloidally synthesized NPLs with a thickness between 4 and 6 QLs is robust with respect to structural anomalies and in

magnetic fields of at least $B = 5$T. Paramagnetic Mn adsorbates are however able to break the QSH edge state at higher concentrations, by enhancing (back) scattering of the electrons in the edge state. Further study on the robustness of this state would require experiments in multiple directions. More statistics is needed on stacked, adjacent and aggregated platelets of various thicknesses and configurations to be able to draw conclusions on the effect that platelets exert on each other. A stronger perpendicular magnetic field should break the QSH edge state. It could also be interesting to apply a parallel magnetic field to break the edge state by enhancing backscattering from non-magnetic defects.

Ch.
4

Chapter 4: Supplementary information

S4.1 Methods

STM/STS measurements were obtained in a Scienta Omicron POLAR SPM Lab at a base temperature of 4.5K. The base pressure during all experiments was in the 10^{-10} mbar range. STM samples were prepared by diluting and sonicating the treated NPL dispersion, after which 10 μL was drop-casted or spin-coated on an Au(111)/MICA substrate purchased from Phasis. Before measuring, the sample was annealed in the STM at 393K for 1-2 hours.

STS spectra were obtained using the following parameters, a 1nA current at -1V was applied before going out of feedback to perform STS. A 10mV bias modulation was applied at 973Hz for the lock-in amplifier and 501 points were obtained at 100ms acquisition time per point.

Adjusted height differential conductance maps were obtained at an in feedback current of 0.5nA and a speed of approximately 5nm/sec.

TEM images were acquired on a Talos F200X (S)TEM operating at 200 keV. TEM samples were prepared by drop-casting a diluted dispersion of NPLs on 200 mesh Formvar/carbon-coated Cu TEM grids

For the **evaporation of Mn** onto the cold sample in the STM a crucible with Mn powder (Sigma-Aldrich, ≥99.9 trace metal basis) was inserted into a FOCUS GmbH EFM3 e-beam evaporator. A 2 keV acceleration voltage was used at a filament current between 0.80 and 0.85mA, resulting in a flux current between 50 and 100nA. Mn was evaporated directly onto the sample which is located in the STM head through holes in the radiation shields for 20 seconds and 2 minutes, respectively. Since determining the coverage is difficult on the Bi_2Se_3 on the Au(111)/mica sample, Mn was also evaporated onto a clean Cu(111) sample with the same procedure for 20 seconds. The results of which can be found in figure S4.5. The (nearly) circular protrusions (which have an apparent height between 0.2nm and 0.8nm) correspond to clusters of Mn atoms. The coverage is approximately 60 clusters per 100 nm^2
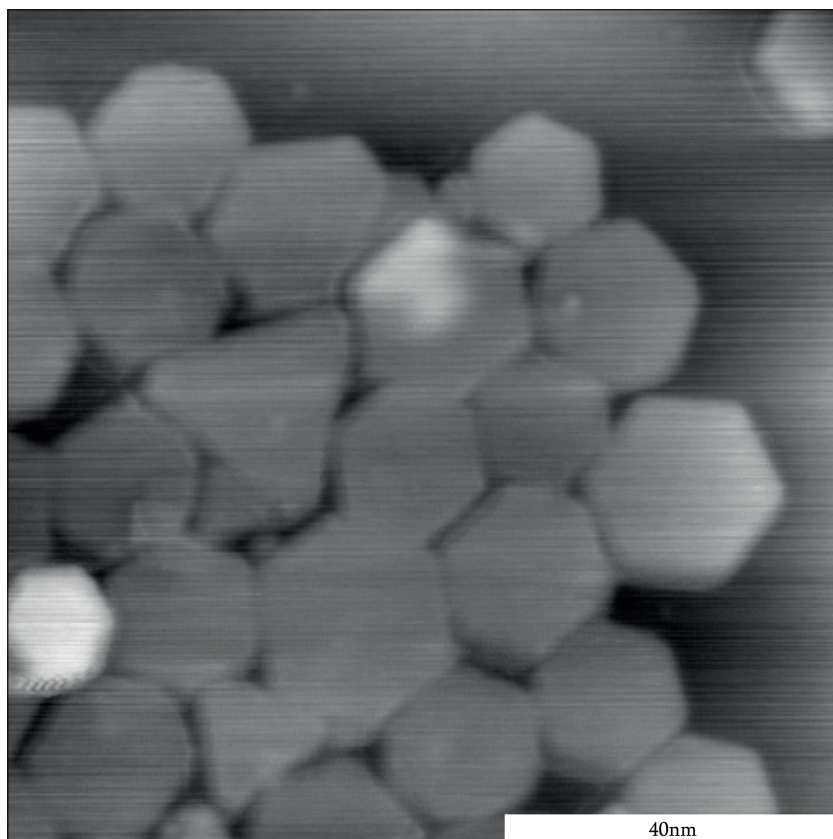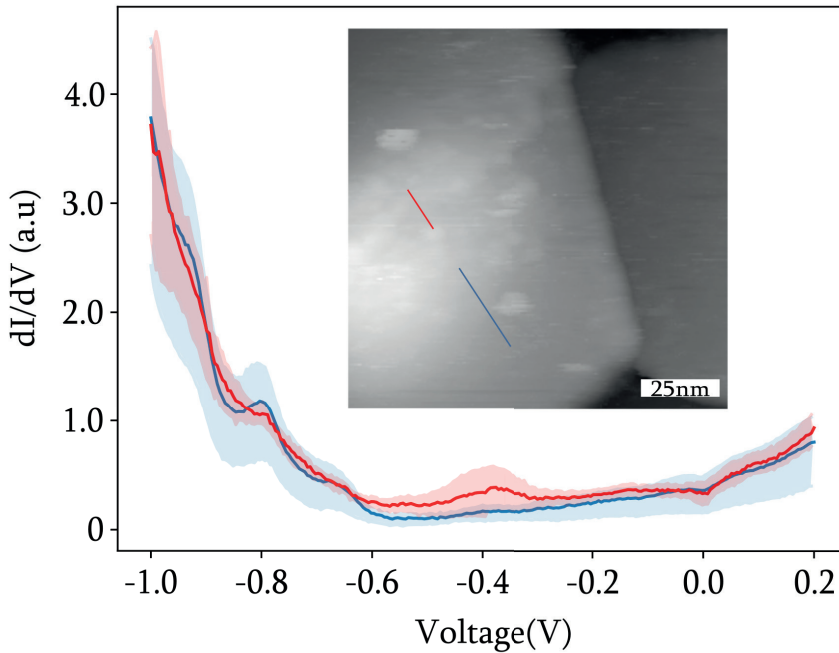
Figure S4.1: **TEM image of colloidally synthesized Bi_2Se_3 NPLs of different shapes and sizes**

Figure S4.2:   Characterization of QSH state at a screw dislocation on a 6QL thick Bi$_2$Se$_3$ NPL
Averaged scanning tunnelling spectrum of local DOS(x,y,E) in the interior (blue) and at a screw dislocation in the center of the nanoplatelet (red). The blue curve is an average of 8 spectra with the standard deviation presented as a blue gloom. The red curve is an average of 4 spectra with the standard deviation presented as a red gloom.

(a)

(b)

(c)
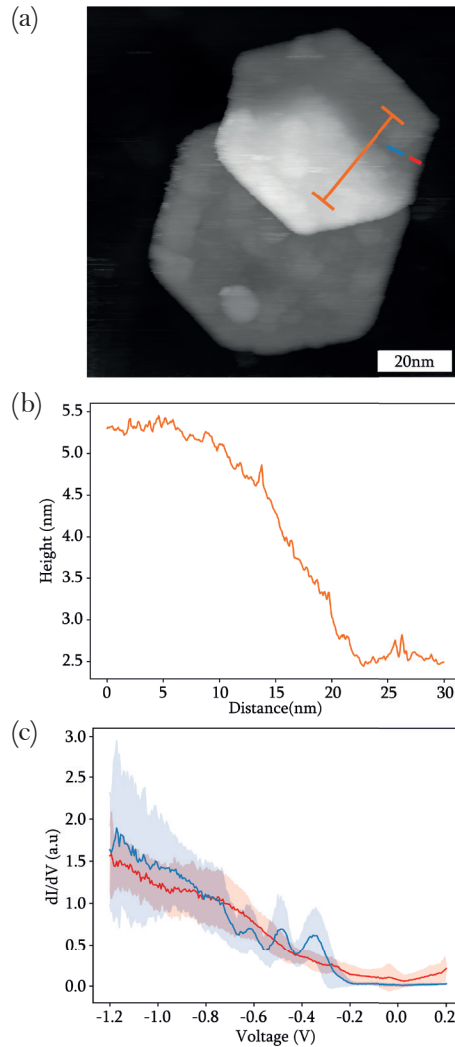
Figure S4.3:   Characteristics of the flexibility of a 3QL thick Bi$_2$Se$_3$ NPL semi stacked on a different 3QL thick NPL and the effect on the QSH state
(a) Scanning tunnelling topography image of a 3QL thick nanoplatelet semi-stacked on a different nanoplatelet showing the location of the line trace in (b) and the locations of the taken scanning tunnelling spectra in (c). **(b)** Line trace of the overlapping platelets showing a change in height over 10-15nm, originating from the folding of the upper NPL. **(c)** Averaged scanning tunnelling spectrum at the interior and at the edge of the top NPL. The blue curve is an average of 15 positions on the blue line in (a). The standard deviation is presented as a blue gloom. The red curve presents an average over 10 positions on the red line in (a). The standard deviation is presented as a red gloom; these spectra represent the edge state.
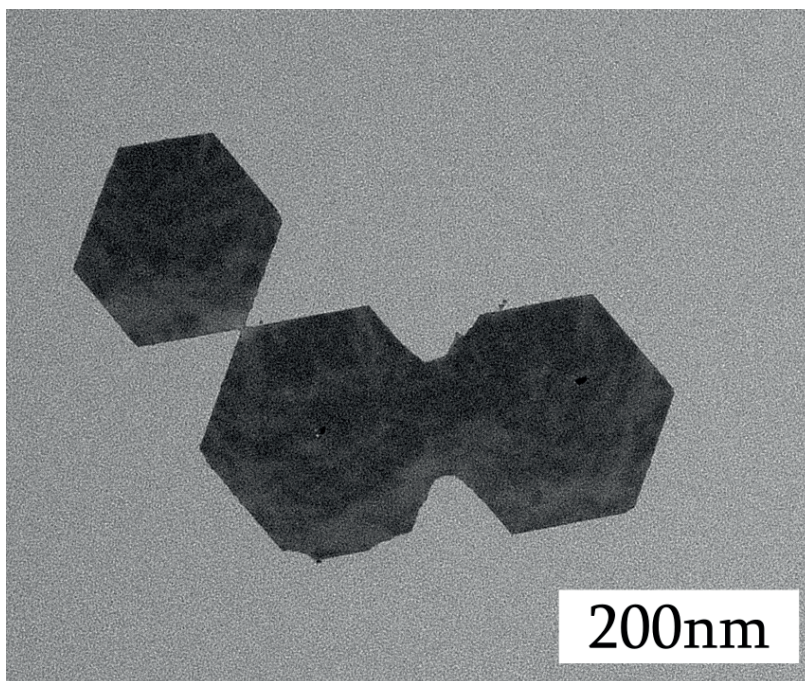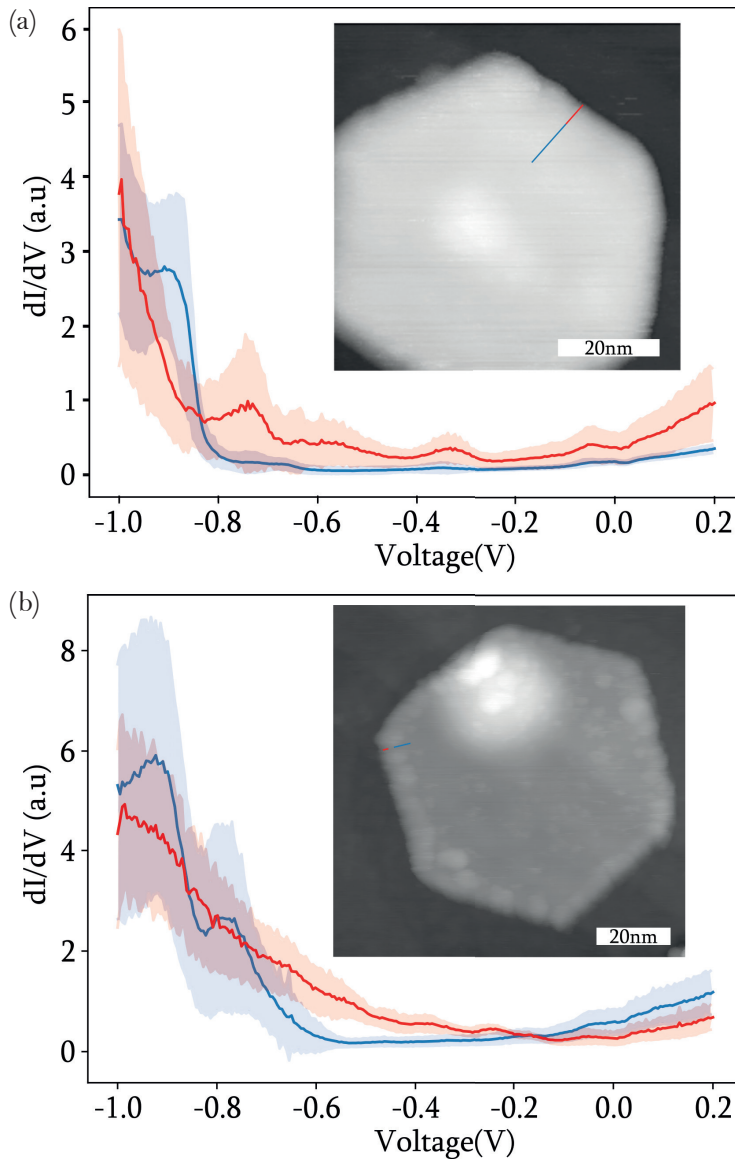
73

Figure S4.4:   **TEM image of fused and adjacent Bi$_2$Se$_3$ nanoplatelets**

Ch.
4

Figure S4.5: **Characterization of the QSH edge state of two Bi$_2$Se$_3$ nano-platelets under the influence of a 5T perpendicular magnetic field**
(a) Averaged scanning tunnelling spectra on a 3QL thick NPL taken in the interior (blue, 28 averages), at the outer edge (red, 14 averages) while under the influence of a 5T perpendicular magnetic field. **(b)** Averaged scanning tunnelling spectra on a 3QL thick NPL taken in the interior (blue, 15 averages), at the outer edge (red, 5 averages) while under the influence of a 5T perpendicular magnetic field.
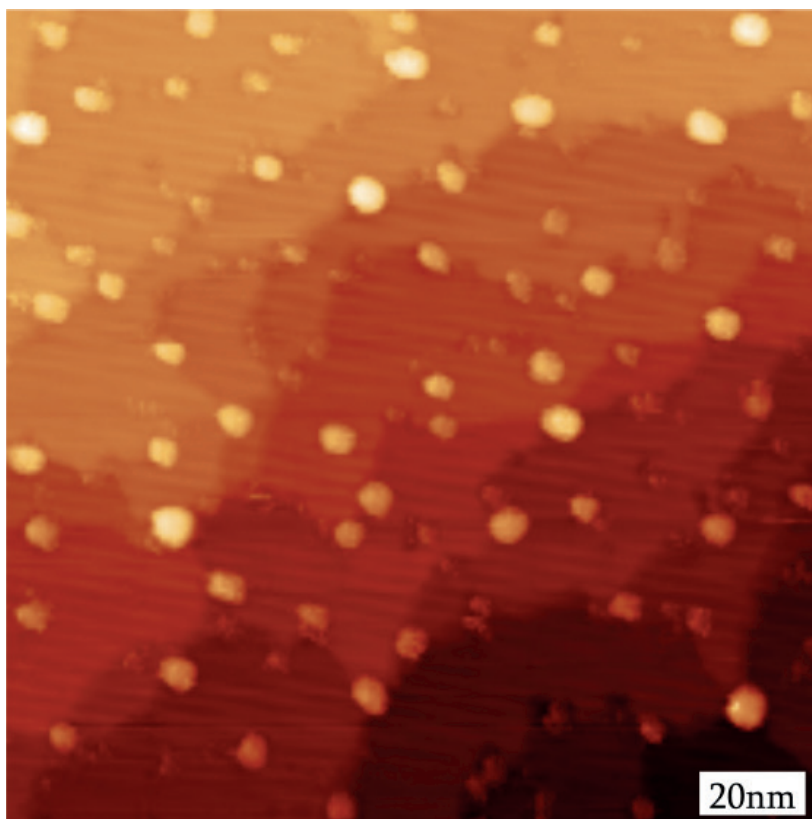
Figure S4.6: **Mn evaporated on a Cu(111) surface for 20seconds at ~50nA flux, showing agglomerations of Mn atoms**

Bibliography

1.   Qi, X.-L. & Zhang, S.-C. The quantum spin Hall effect and topological insulators. *Phys. Today* **63**, 33–38 (2010).

2.   Koenig, M. *et al*. The Quantum Spin Hall Effect: Theory and experiment. *J. Phys. Soc. Jpn.* **77**, 031007 (2008).

3.   Bernevig, B. A. & Zhang, S.-C. Quantum spin Hall effect. *Phys. Rev. Lett.* **96**, 106802 (2006).

4.   Zhang, Y. *et al*. Crossover of the three-dimensional topological insulator Bi_2Se_3 to the two-dimensional limit. *Nat. Phys.* **6**, 584–588 (2010).

5.   Zhang, H. *et al*. Topological insulators in Bi_2Se_3, Bi_2Te_3 and Sb_2Te_3 with a single Dirac cone on the surface. *Nat. Phys.* **5**, 438–442 (2009).

6.   Das, S. K. & Padhan, P. The effect of mechanical strain on the Dirac surface states in the (0001) surface and the cohesive energy of the topological insulator Bi_2Se_3. *Nanoscale Adv.* **3**, 4816–4825 (2021).

7.   Reid, T. K., Nayak, S. K. & Alpay, S. P. Strain-induced surface modalities in pnictogen chalcogenide topological insulators. *J. Appl. Phys.* **129**, 015304 (2021).

8.   Battilomo, R., Scopigno, N. & Ortix, C. Tuning topology in thin films of topological insulators by strain gradients. *Phys. Rev. B* **100**, 115131 (2019).

9.   Wang, Q., Sheng, L., Edge mode of InAs/GaSb quantum spin Hall insulator in magnetic field. *Acta Phys. Sin.* **64**, 097302 (2015).

10.   Zhang, S.-B., Zhang, Y.-Y. & Shen, S.-Q. Robustness of quantum spin Hall effect in an external magnetic field. *Phys. Rev. B* **90**, 115305 (2014).

11.   Landau, L. On the theory of phase transitions. *Zh. Eksp. Teor. Fiz 1*, 19–32 (1937).

12.   Umantsev, A. *Landau Theory of Phase Transitions. in Field Theoretic Method in Phase Transformations* 139–169 (Springer International Publishing, 2023). .

13.   Kane, C. L. & Mele, E. J. Z_2 Topological order and the quantum spin Hall effect. *Phys. Rev. Lett.* **95**, 146802 (2005).

Ch.
4

14.   Okada, Y. *et al.* Direct observation of broken time-reversal symmetry on the surface of a magnetically doped topological insulator. *Phys. Rev. Lett.* **106**, 206805 (2011).

15.   Skolasinski, R., Pikulin, D. I., Alicea, J. & Wimmer, M. Robust helical edge transport in quantum spin Hall quantum wells. *Phys. Rev. B* **98**, 201404 (2018).

16.   Yang, Y. *et al.* Time-Reversal-Symmetry-broken quantum spin Hall effect. *Phys. Rev. Lett.* **107**, 066602 (2011).

17.   Tkachov, G. & Hankiewicz, E. M. Ballistic quantum spin Hall state and enhanced edge backscattering in strong magnetic fields. *Phys. Rev. Lett.* **104**, 166803 (2010).

18.   Evers, W. H. *et al.* Low-dimensional semiconductor superlattices formed by geometric control over nanocrystal attachment. *Nano Lett.* **13**, 2317–2323 (2013).

19.   Taskin, A. A. *et al.* Planar Hall effect from the surface of topological insulators. *Nat. Commun.* **8**, 1340 (2017).

20.   Du, L., Knez, I., Sullivan, G. & Du, R.-R. Robust helical edge transport in gated InAs/GaSb bilayers. *Phys. Rev. Lett.* **114**, 096802 (2015).

Chapter 5:
Quantum corrals in a perpendicular magnetic field

By patterning a 2D electron gas with repulsive scatterers it is possible to emulate atoms, molecules and even lattices. Thus far, this approach has provided control over the lattice geometry, which orbitals couple, and the strength of the coupling between artificial atoms. In real materials, the spin degree of freedom plays an important role. However, thus far the spin degree of freedom i.e. the interplay between magnetic fields and artificial atoms has not been reported. Here, we experimentally and theoretically probe the influence of a perpendicular magnetic field on the electronic structure of quantum corrals. In particular, circular and rectangular corrals were assembled by positioning CO molecules on a Cu(111) substrate. Muffin-tin calculations performed on the artificial atoms predict a splitting of the s-type orbitals due to the Zeeman effect and a splitting of the p-type orbitals due to the Zeeman effect as well as, a Lorentz force in the experimentally accessible magnetic fields. However, the effects are predicted to be small. The experimental results are inconclusive.

"You name it, we build it."
—dr. Thomas Gardenier

5.1: Introduction

A unique feature of the scanning tunnelling microscope (STM) is the possibility to position adparticles on a substrate with atomic precision. This method, first described in 1993 by researchers from IBM[1], fulfilled the dream of Richard Feynman of being able to build structures atom by atom.[2] In 2012, atomic manipulation was used to create an artificial system resembling graphene.[3] Gomes et al. showed how the repulsive potential behaviour of carbon monoxide (CO) molecules could be used to contain the 2D electron gas (2DEG) of the copper (111) substrate by creating a honeycomb like structure similar to graphene which they could tune to simulate pseudo magnetic fields.[3]

This system, CO molecules on Cu(111), has been used to investigate properties of materials both known and unknown in nature like splitting of p_x and p_y orbitals, topological insulating edge states and p-orbital flatbands.[3–7] All studies thus far neglected the effect of the spin of the confined electrons, as it was not needed to explain the observations. Being able to understand and utilize the spin degree of freedom in artificial lattices could increase the different kinds of physics that can be investigated.

To fully understand the physics at play it is useful to look at one of the simplest systems one can build using the atom manipulation technique: the quantum corral. A quantum corral consists of a shape of adparticles to confine the 2D electron gas of the Cu(111) substrate. The quantum corral can be modelled as a particle in a 2D box, and be thought of an artificial atom. By coupling these corrals together, molecules and lattices can be emulated.[8–10]

The Pauli exclusion principle states that no two electrons in an (artificial) atom can have identical quantum numbers. Thus, every spatial orbital can only be filled by two electrons, one with spin quantum number S = +½ℏ (spin-up) and one with spin quantum number S = -½ℏ (spin-down). In the absence of a magnetic field, the two electrons have the same energy. By applying a perpendicular magnetic field, the degeneracy is lifted due to Zeeman effect (for s- and p-type orbitals) and Lorentz forces (for p-type orbitals which have non-zero orbital angular momentum).

An important characteristic of orbitals in real atoms is the well-defined angular momentum due to the spherical shape, which leads to an orbital momentum of zero for electrons in the s-orbital but non-zero for p-orbital electrons. It has been shown that a 2D equivalent of these orbitals can be recreated using circular artificial atoms.[1,8] However, lattices build in the STM are often based on rectangular or triangular corrals, for which the orbital angular momentum is not well-defined. It is therefore not a-priori clear how the electronic states of such corrals interact with a magnetic field.

For this work, lateral atomic manipulation was used to create circular and

rectangular quantum corrals. The electronic structure of the corrals was measured in the presence and absence of a $B = 5$T perpendicular magnetic field. We hypothesize that circular and rectangular corrals show similar behaviour.

This work is based on experimental work by Thomas Gardenier and theoretical work by Jette van den Broeke who devised the muffin-tin method used in this chapter.[11,12]

5.2 CO on Cu(111)

The quantum corrals were built by placing CO on a Cu(111) substrate in different configurations. Copper has an FCC crystal structure and therefore the (111) plane features a close-packed array of Cu atoms. At the interface of this Cu(111) surface and the vacuum there exists a Shockley surface state which behaves as a 2D electron gas (2DEG).[1] This electron gas is the cornerstone of building artificial atoms on the surface. By placing repulsive carriers on the surface, the sea of electrons can be shaped into the desired structures.[1] CO is such a repulsive scatterer and it has been shown that CO adsorbs on top of copper atoms.[13] Figure 5.1 shows the band structure of the Cu(111) surface.[14] The Shockley surface state exists in a pseudo gap of the Cu(111) surface and has a parabolic shape. The band onset is located at approximately -0.45eV. Around 0.3eV, the surface state and the bulk states cross.[14] This is the first limitation of this system. When states would appear outside this range of -0.45eV and 0.3eV, they would not be visible anymore with Scanning Tunnelling Spectroscopy (STS). We performed simulations for quantum corrals of different shapes and sizes to make sure that the features of interest are within the experimentally accessible energy range, which will be discussed later in this chapter.

Ch. 5
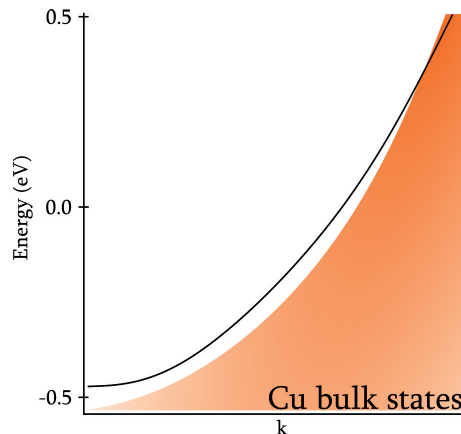
Figure 5.1: The Shockley surface state (black) of Cu(111) located in the pseudo gap of the bulk (orange)

5.3 Building artificial atoms using scanning tunnelling microscopy

To create the desired structures, CO was evaporated on the cold Cu(111) surface. These molecules land on random locations of the sample. CO molecules always adsorb on top sites of the (111) substrate.[13] In general, the tip of a STM can be used to push or pull molecules over the surface. This is called lateral manipulation.[15] For CO on Cu(211), Bartels *et al.* reported that the molecules are pushed.[15] It should be noted that in some cases atoms and molecules can be picked up from the surface and deposited at a desired location; this is called vertical manipulation.[16,17] For the CO on Cu(111) system lateral manipulation can be performed with atomic precision and large structures can be build.[3–5] The following procedure was used to laterally manipulate a CO molecule. First, the tip of the STM was positioned above a CO molecule using the normal scanning parameters. With these parameters, the tip is too far from the molecule to induce lateral movement. Then, the tip is approached to the molecule by decreasing the bias voltage and increasing the current. In our experiments, a tunnelling resistance of about $250k\Omega$ was used (see figure 5.2, step 1). When the tip is then moved over the surface, the CO molecule beneath the tip will follow the tip (figure 5.2, step 2). When the tip has reached the desired location, the junction resistance is gradually increased, leaving the molecule behind at the target destination.

The insert in Figure 5.2 depicts height traces of the tip as a function of lateral position during manipulation. CO molecules are imaged as dark circles in constant-current STM topographic images. First focus on the top trace. One observes a clear saw-tooth pattern, with a periodicity that matches the distance between nearest neighbour Cu atoms. This can be explained as follows. When the tip is placed behind a molecule and moves towards the centre of the CO in a lateral motion while in feedback, the tip will approach the surface (CO appears as a depression) until the force between tip and molecule is large enough to push the CO molecule to the next Cu(111) site. This results in a sudden retraction of the tip. These findings are in agreement with a previous report by Bartels *et al.*[15] However, we also observe the inverse saw-tooth pattern, see the bottom trace. This trace is indicative of pulling CO molecules across the surface. When the tip is placed directly on top of the CO molecule, and then moves laterally away from the molecule, the tip-sample distance is increased until there is a sudden decrease in the tip-height, signalling that the CO molecule has jumped underneath the tip.. Hence, CO molecules on Cu(111) can be manipulated by both pushing and pulling modes, which was not documented before.

As mentioned before, the CO molecules can only be positioned on the top site locations of the Cu(111) atoms. This must be taken into account when designing a circular or rectangular quantum corral. Furthermore, it is not possible to place two CO molecules in directly adjacent sites on the close packed row of the
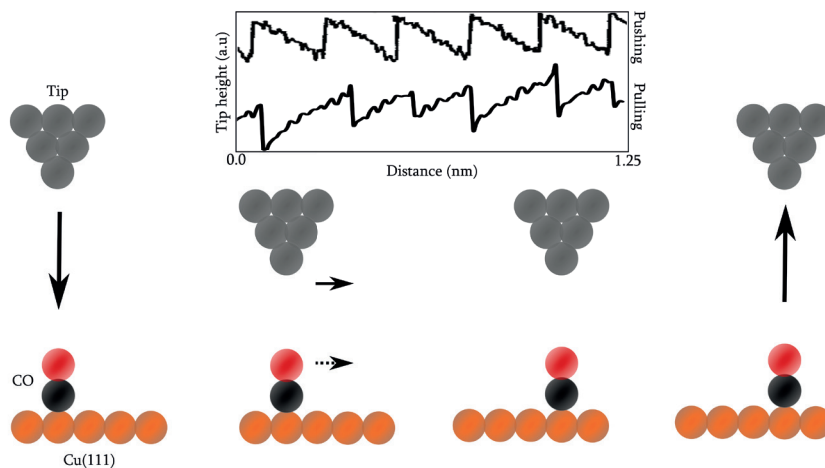
Figure 5.2: **Schematic representation of lateral manipulation of a CO molecule (black-red) using an STM tip (grey) on Cu(111) (orange).**

Step 1: The tip-sample distance is reduced from imaging height to manipulation height by increasing the setpoint current and decreasing bias voltage. **Step 2:** The tip is moved laterally across the surface, the tip pushes/drags the molecule along. **Step 3:** When the target position has been reached, the tip-sample distance is increased again to imaging height. (insert) Height traces during the lateral manipulation when pushing or pulling a CO atom (the height traces are offset arbitrarily).

Cu(111) surface.[18] The repulsive behaviour of the molecules will force one of the two molecules to a different site. Lastly, it has been shown that a single walled configuration is insufficient to eliminate coupling of the trapped electrons with the surface state outside of the corral.[11] This coupling leads to insufficient energy resolution. Artificial atoms and lattices constructed using the CO/Cu(111) platform, can be simulated effectively using muffin-tin calculations.[3–5,8]

5.4 Muffin-tin calculations in a magnetic field

Muffin-tin calculations can be used to simulate the energy landscape when repulsive scatterers are placed on a 2DEG.[19] The 2DEG is modelled as uniform electron gas whereas the scatterers are modelled as circular discs with a diameter of 0.6 nm and a potential of 0.9 eV, i.e. like an upside-down muffin tin.[4,7] After defining the potential landscape the corresponding Schrödinger equation can be solved:

Ch.
5

Chapter 5: Quantum corrals in a perpendicular magnetic field

$$\frac{-\hbar^2}{2m^*}\nabla^2\Psi + V(x,y)\Psi = E\Psi \qquad (5.1)$$

In equation (5.1), $V(x,y)$ is the potential landscape. This is essentially a par-
ticle–in–an–intricate–box problem. For the corrals build in this chapter, the
Schrödinger equation cannot be solved analytically, and we therefore use nu-
merical methods. The wavefunction is defined on a grid of n * n points rather
than as a continuous function. The number of points chosen for the grid will
determine the precision of the calculation. However, more points imply a longer
calculation time. Therefore, one needs to balance accuracy with computational
cost. Periodic boundary conditions were applied. The size of the simulation
cells was chosen such that corrals of neighbouring cells did not have a signifi-
cant interaction.

The kinetic energy term is treated using derivative matrices (D_x, D_y), and the
potential landscape is discretised into the n * n grid points. This leads to the
following discrete Hamiltonian:

$$H = \frac{-\hbar^2}{2m^*}(\mathbf{D}_x^2 + \mathbf{D}_y^2) + \mathbf{V} \qquad (5.2)$$

The Hamiltonian given in equation (5.2) works well for a system without an
external field.[4–6] When such a field is applied, the kinetic energy term of the
Hamiltonian becomes with q the charge of the electron and $\mathbf{A}$ the magnetic
vector potential acting on the electrons (and $\nabla \times \mathbf{A} = \mathbf{B}$). The magnetic field
acting on the spin of the electrons leads to an additional term proportional to
$\mathbf{S} * \mathbf{B}$, with $\mathbf{S}$ the electron spin operator. This results in the following Hamilto-
nian:

$$H = \frac{(\mathbf{p} - q\mathbf{A})^2}{2m^*} - \frac{q}{m^*}\mathbf{S}\cdot\mathbf{B} + \mathbf{V} \qquad (5.3)$$

In the experiments performed during this project it was only possible to apply a
magnetic perpendicular to the crystal surface which hosts the 2DEG. Equation
5.3 can therefore be rewritten to:

$$H = \frac{\mathbf{p}^2}{2m^*} - \frac{q}{m^*}(\mathbf{L} + g_e\mathbf{S}\cdot\mathbf{B}) + \frac{q^2\mathbf{B}^2}{8m^*}\mathbf{r}^2 + \mathbf{V} \qquad (5.4)$$

L in equation 5.4 is the angular momentum, $\mathbf{r}$ is the position vector, g_e is the
Landé factor (assumed to be $g_e \approx 2$, the value for free electrons). Additionally,
the symmetric gauge $\mathbf{A} = \frac{1}{2}\,\mathbf{B} \times \mathbf{r}$ was used. For an s-type orbital the angular
momentum operator $\mathbf{L} = 0$, whereas for a p-type orbital the operator $\mathbf{L} \neq 0$. As
this term scales with the magnetic field $\mathbf{B}$, it is now possible to distinguish the
effect of the magnetic field on the orbital momentum of the p-type orbital. $\mathbf{S}$ is

the operator of the spin component which can have a value of ±½ ħ.

Solving the Schrödinger equation gives the eigen energies from which it is possible to determine the Local Density of State (LDOS) as a function of energy, which can be directly compared to STS data. In the calculation, peaks in the LDOS are infinitely sharp. Experimentally this is not the case as multiple sources can cause broadening. First, we consider thermal broadening. The STM has a working temperature of 4.5K. Using the Boltzmann equation, the thermal broadening is calculated to be: $\Delta E_{th} = 3.3\ K_b T \approx 0.4$meV.[20,21] Secondly, a Lorentzian broadening is present due to the limited lifetime of the 2DEG electrons. The lifetime of these electrons has been reported to be ~29 fs,[22] which gives a Lorentzian broadening of: $\Gamma = ħ/\tau = 23$meV. This value is significantly higher than the thermal broadening. The features in the experimental spectra are significantly broader than this (Full width half maximum of 40 meV). We attribute this to the presence of the CO molecules on the surface. These adsorbates not only cause scattering between states in the 2DEG but also increase the chance of an electron being scattered from the 2DEG to the bulk, thereby reducing the lifetime. Throughout this chapter, a broadening of 40 meV will be used.[4,5,7,8]

5.5 Designs

In previous work, four different corrals were designed and built (see figure S5.2): A small circle, a small rectangle, a large circle and a large rectangle.[11] These corrals were designed with most of the limitations in mind using the CO on Cu(111) system. After the construction of these corrals, spectroscopic measurements were performed at various locations of the corral. These measurements were performed both at $B = 0$T and $B = 5$T. It turned out however that these results were inconclusive. One of the conclusions from those experiments was that the designs with a single wall of CO molecules allowed for too much coupling between the confined electrons and the electrons outside of the corral (also considering the magnitude of the effects of the magnetic field, in conjunction with the observed broadening). Adding an additional row of CO molecules to a circular corral reduced the coupling with the environment. This resulted in a better agreement between the calculations and the experimental results.

New designs for artificial atoms were created to limit this coupling by adding an additional row of CO molecules which increased the potential barrier between the 2DEG of the substrate and the confined electrons in the quantum corral. The top row of figure 5.3 shows the improved designs for a small rectangular corral (left), a large rectangular corral (middle) and a large circular corral (right). With the design of the large circular corral being the same as previous work. In these designs, the Cu(111) surface is represented by orange

dots whereas the CO molecules are depicted as black discs. The bottom row of figure 5.3 shows the experimental realization of the quantum corrals in the STM. When the CO molecules are two close-packed sites apart, it is not possible to identify individual CO molecules anymore.
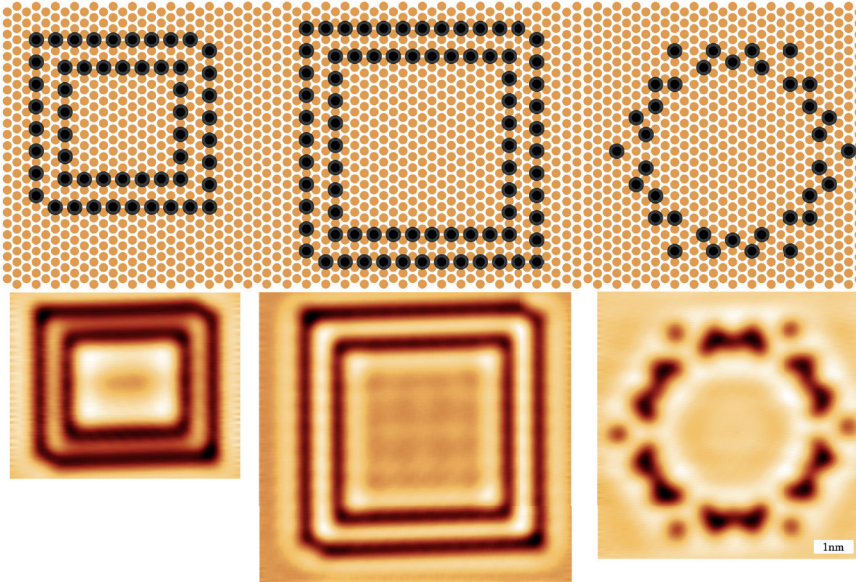
Figure 5.3: **Design and experimental realization of three different quantum corrals.**

(Top) Schematic design of a small rectangle (left), a large rectangle (middle) and a large circular (right) quantum corral with black circles representing CO molecules on a Cu(111) surface in orange. **(Bottom)** Experimental realization of the three quantum corrals using the lateral atomic manipulation technique in the STM. Scalebar is 1nm for all subfigures

5.6 Theoretical results

The differences between measurements with and without a perpendicular magnetic field are expected to be small. It is therefore important that a procedure is devised to extract information from small differences in the data. First, the experimental data is normalized using a reliable and reproducible method.[3] The dI/dV spectra of the corrals were scaled using dI/dV data from the Cu(111) background by equalizing the intensity of the feature originating from the surface state at -0.45V. This feature is present in both spectra and can therefore be used as an internal standard. After the scaling, the Cu(111) background was subtracted from the dI/dV measurements taken on the artificial atoms. This

removes accidental features due to the tip and Cu(111) background. Finally, we use the fact that a magnetic field cannot create or destroy electronic states. Therefore, the peak area corresponding to a particular state, should be equal for experiments performed with and without magnetic field. We enforced this in our analysis.

Considering the different spatial distribution of s-like and p-like orbitals, we took spectra at the centre of the corral (to analyse s-like orbitals) and off-centre (for p-like states). Further elaboration on the different normalization methods can be found in the methods section of the supporting information and figure S5.1.

After the normalization steps described above, any difference in the electronic structure can be attributed to the splitting caused by the magnetic field. To visualize and quantify the splitting, the normalized spectra with and without magnetic field will be subtracted. If a single electronic state splits, it will result in two smaller peaks, however due to limited energy resolution this will only be discernible as a slightly broader peak with less intensity as can be seen in figure 5.4a. However, subtracting the original single peak from the combined double peak will result in a characteristic peak-dip-peak structure, shown in figure 5.4b. Importantly, as stated before, no additional electronic states can be created by the magnetic field and therefore the integrated area of the peak-dip-peak structure should be 0.

Figure 5.5 shows calculated subtracted spectra ($B = 5T$ - $B = 0T$) on a circular (a) and rectangular quantum corral (b). Three different calculations were performed. First, the full Hamiltonian was used to calculate the local density of states, shown as a red line for spectra taken in the centre and black line for spectra taken off centre. Secondly, the spin operator was excluded from the Hamiltonian. In this case only the effect of the Lorentz force on the electrons is taken into account The results are shown as the orange dotted line (centre position) and blue dotted line (off-centre position). The third calculation only includes the spin term but excludes the orbital momentum term in the Hamiltonian, resulting in the pink dashed line for the centre position and the grey line for the off-centre position in the quantum corrals. In the calculations using the full Hamiltonian a peak-dip-peak feature is visible in the difference spectra for both the circular and rectangular corrals at the energies corresponding to the 1s-state ($V = \sim$-0.2V). Spectra taken at the off-centre position show an additional peak-dip-peak features due to the 1p-orbital ($V = 0.15V$). If the spin operator is excluded in the calculation, there is no peak-dip-peak feature visible for the 1s-orbital. In contrast, the p-like states do exhibit a peak-dip-peak structure, as can be seen in the spectrum taken at the off-centre position. The different behaviour observed for s- and p-like orbitals is consistent with the different angular momentum that these states should have. Interestingly, the difference spectra for circular and rectangular corrals are qualitatively similar,

Ch.

5
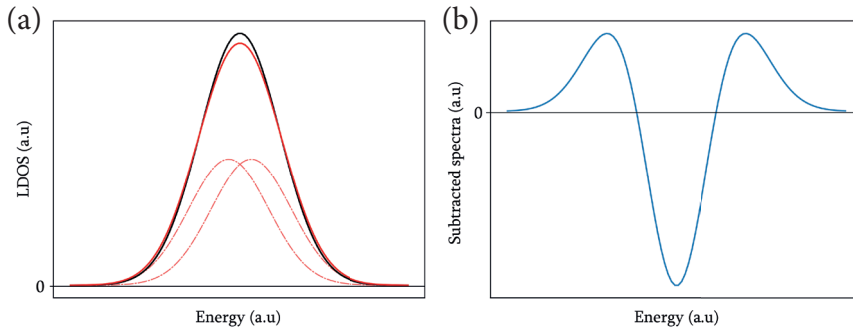
Figure 5.4: **Subtracting split peaks.**

(a) A single peak (black spectrum) that is split into two peaks (red dotted spectra) which still have significant overlap will result in a singular peak which is slightly lower in intensity but is slightly broader near the base of the peak. (red spectrum). **(b)** Subtraction of the black and red spectra in (a) results in a peak-dip-peak structure with a total integrated area of 0.

suggesting that p-like orbitals in rectangular corrals have non-zero angular momentum as well. When only the Zeeman effect is included in the calculations, a peak-dip-peak structure is observed for both orbitals. However, for the p-like state, the feature is located at lower energy than the feature induced by the Lorentz force. By taking STM measurements at different locations in the quantum corrals at different magnetic field and constructing the difference spectra, it should be possible to observe the characteristic features shown in Figure 5.5. These measurements could also give an indication for the relative importance of the Lorentz and Zeeman terms.

5.7 Experimental results and discussion

Figure 5.6 shows topographic images of three created artificial atoms, including the locations where differential conductance spectra were measured, with and without an applied perpendicular magnetic field. The locations were chosen such that the DOS originating from the s-type orbital and p-type orbitals are maximized (red, and black, respectively). The resulting normalized *dI/dV* spectra as well as the calculated muffin-tin spectra are shown in the right column. Similar to previous work,[8] the different peaks are attributed to the respective orbitals with the s-orbital being symmetric around the centre with the highest intensity in the centre of the corral and the p-orbital having a node in the centre and the highest intensity off-centre (see figure S5.3).
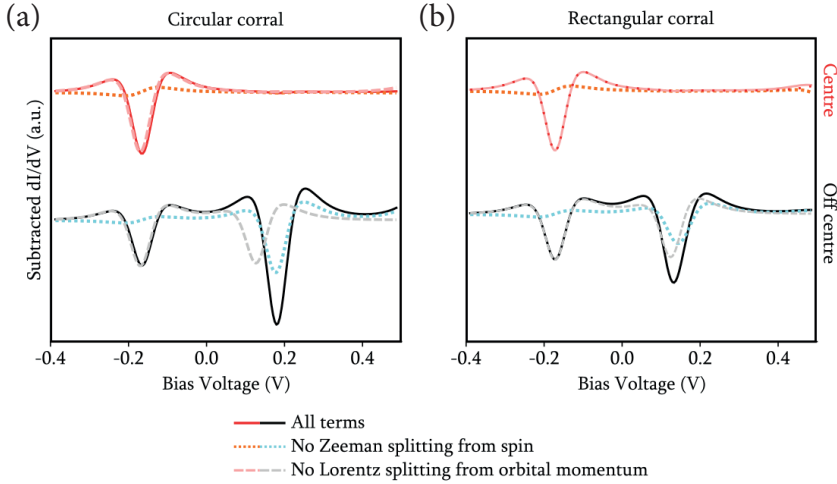
Figure 5.5: Calculated subtracted *dI/dV* spectra on a circular corral (a) and a rectangular corral (b) in two different locations: the centre of the corral (top) and off centre of the corral (bottom). The solid lines include all terms in the Hamiltonian, the dotted line includes only the orbital momentum term, and the striped line only includes the spin term.

Ch. 5

The normalized spectrum taken in the centre of the large rectangular corral shows good agreement to the corresponding muffin-tin calculations for the 1s-orbital peak around $V = -0.35$V. At 0.15V in energy the 2s-orbital peak can be discerned for the muffin-tin calculation. The experimental data shows significant broadening of the peaks which lowers the intensity. This can be attributed to the increased coupling to the Cu(111) bulk states. This can also be seen for the states at positive bias voltages for the data on the off-centre position, as well as for both experimental spectra on the circular corral. We will therefore restrict the analysis to the two lowest energy states located in the negative region of the voltage range. The experimental data taken on the off-centre positions in the large rectangular and circular corrals show good agreement to the muffin-tin calculations for the 1p-orbital like state. Therefore, it was decided to use the data acquired in the centre of the corrals to analyse the 1s-orbital like state and the off-centre data for the analysis of the 1p-orbital like peak. The difference between the experimental data between the $B = 0$T and $B = 5$T spectra is very small. To analyse the data further, we applied the normalization procedure described above. The boundaries used in determining peak areas for the respective orbital states are depicted as vertical dotted lines in the spectroscopy data for the large rectangular and circular quantum corrals. The resulting difference spectra are shown in figure 5.7.
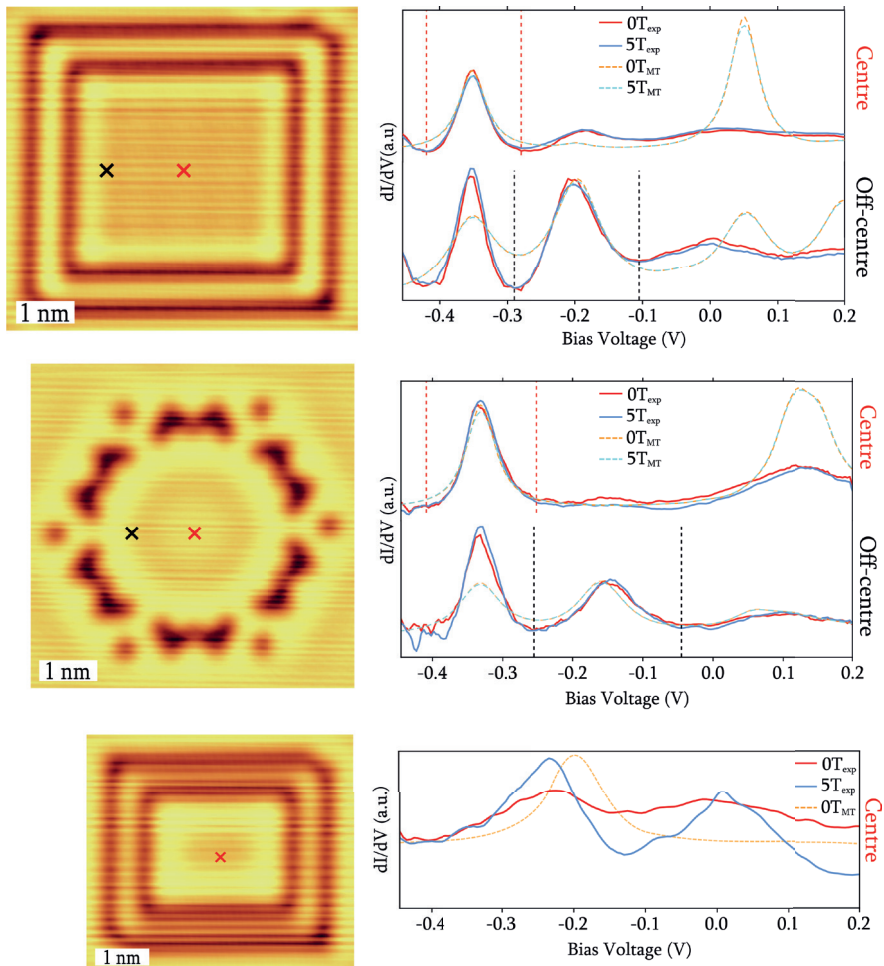
Figure 5.6: **STS data compared to muffin tin calculations taken at two locations on three quantum corrals.**

(Left) Topographic constant current images of three experimentally realized quantum corrals. Red and black crosses indicate the positions where the differential conductance spectra shown in the right column were acquired. **(Right)** Normalized *dI/dV* spectra taken on centre (red) and off-centre (black) positions in quantum corrals. Muffin-tin calculations on the large rectangular and circular corrals are shown as well. The vertical dotted black and red lines indicate the integration areas used for normalization.

For the smaller rectangular corral, the experimental *dI/dV* spectra and the calculated *dI/dV* spectra show significant differences. In the experimental data the peaks are not well-defined and the intensity of the base of the peak is differ-

ent which makes integration over the peak challenging. There is also a signifi-cant shift in energy for the 1s-type orbital peak. A possible explanation is that there is coupling between the confined electrons in the corral and the electrons between the two walls of CO molecules. When the peaks are poorly defined, the analysis of splitting of the states will not be possible and therefore it was decided to not analyse the data on this quantum corral further.

The integrated peaks of the 1s and 1p-like orbitals are shown in figure 5.7, including the corresponding subtracted spectra with the spectra taken at $B = 0T$ subtracted from the spectra taken at $B = 5T$. Results from muffin tin calcu-lations on the same system are also shown. In the subtracted experimental data for the 1s-like state in the rectangular corral (figure 5.7a), a pronounced dip is observed at the energy predicted by the muffin-tin simulations. The uncertain-ly in the experimental data is too high to convincingly observe the expected peak–dip–peak structure.

For the 1p-orbital state of the rectangular corral there is no well-defined peak–dip–peak structure visible after subtracting the 0T and 5T measurements. There is a dip visible with similar intensity as calculated by muffin tin, but there is an energetic mismatch. There seems to be a large asymmetry in the peaks left and right of the dip. A potential explanation could be the close prox-imity of the 1s and especially the 2s type state (which is extremely broad). A second explanation could be coupling between the energy states in the corral and states originating from the electrons confined in between the two rows of CO. Alternatively, the background correction might not be able to fully and properly correct for tip-artefacts or human error. During the experiments it was attempted to keep the location at which the spectra were acquired the same.. After ramping the magnetic field, a significant drift was observed and therefore it cannot be excluded that the location of the spectra taken with and without magnetic field were taken at slightly different locations. Despite these uncertainties, for this corral, the effects of a $B = 5T$ magnetic field are on the verge of being measurable.

Subtracted differential conductance data on the large circular corral are shown in figure 5.7b, including the corresponding muffin-tin calculations. For the subtracted spectra, no peak-dip-peak structure can be discerned, despite the extensive normalization procedure and the integration and equalization of the peaks. Instead, at the energy of the s-like state, a large peak is visible indicat-ing that the s-orbital peak at $B = 5T$ is higher in intensity than the peak at $B = 0T$, which can also be seen in the corresponding normalized spectra. This is not physically possible as a magnetic field cannot create additional electronic states. We conclude that the signal-to-noise ratio in the experimental data is insufficient to discern the effect of the magnetic field on the electronic struc-ture of this quantum corral.
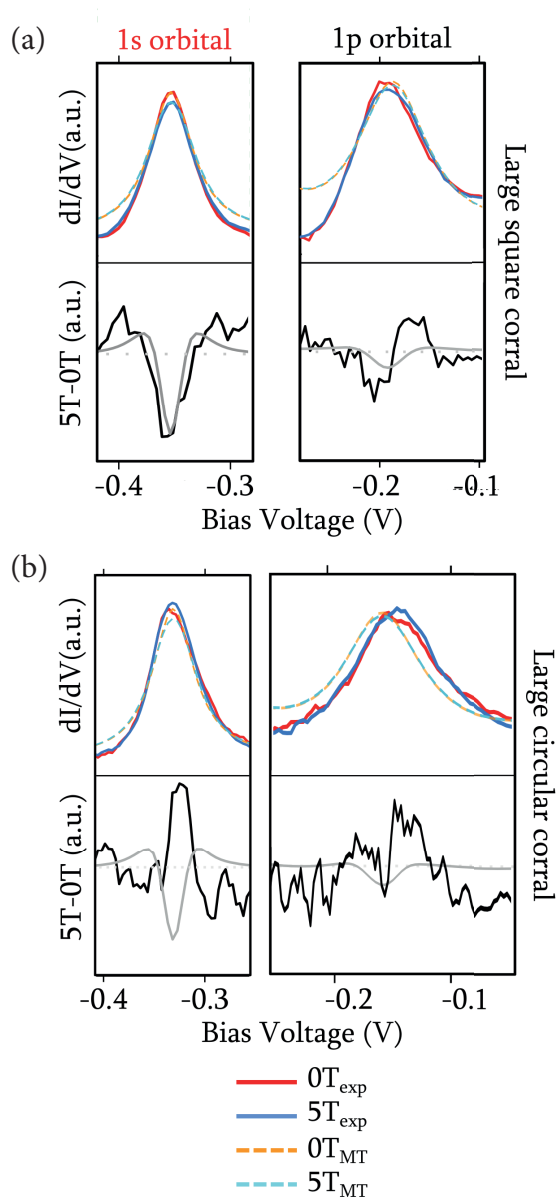
Figure 5.7: Enhanced normalized spectra focussed on the integrated region for the 1s (left column) and 1p-orbital peaks (right column) for the large rectangular (a) and circular corrals (b).

5.8 Conclusion and outlook

Three artificial atoms were built and investigated to probe the effect of a magnetic field on the s- and p-like orbitals. Theoretically, it has been shown that the Zeeman effect should shift the energies of the electrons in both the s- and p- like orbital. The Lorentz force should only significantly affect the electrons in the p-like orbital as this force only affects electrons with a non-zero orbital momentum. The small rectangular corral showed little overlap between the experimental results and the muffin-tin calculations, potentially due to coupling between the electrons confined in the corral and the electrons confined between the two potential barriers. This corral was therefore not investigated further.

The designs used in this project allow for minimal coupling between the 2DEG of the Cu(111) substrate and the confined electrons in the quantum corrals. This leads to a well-defined peak-dip-peak structure for the 1s orbital of the large rectangular artificial atom when subtracting differential conductance data taken at $B = 0$T from data taken at $B = 5$T. However, there is a significant mismatch between the experimental results and the muffin-tin calculations for the 1p orbital in the rectangular artificial atom and both orbitals of the circular artificial atom. The following conclusions were drawn: first, human error is present in selecting a location for the dI/dV spectroscopy combined with drift present after ramping the perpendicular magnetic field. A small difference in location can cause a mismatch in the spectra at 0T and 5T. Secondly, the stability of the system needs to be taken into account. During the ramping of the magnet in the STM there is a large probability of a tip change, despite the extensive normalization procedure including integration of the individual peaks belonging to the 1s or 1p-like orbitals it cannot be excluded that small differences are still present. Lastly, coupling between the different energy states or to the states present in between the two potential barriers (rows of CO molecules) could be present. The combination of these factors, in combination with the small effect of the magnetic field, make it impossible to discern the influence of the Zeeman and Lorentz contributions.

To improve the experiments, the following adjustments should be made. In the current software used for doing STM experiments there is no drift compensation which correct for the drift while doing spectroscopy. This feature is available for software used in other STMs and this could reduce the error in location where the measurements are recorded. Additionally, the system should be left to stabilize for at least multiple hours to reduce the drift as much as possible. By averaging multiple differential conductance curves, the signal-to-noise ratio in the experimental data can be improved. Furthermore, a higher magnetic field would create a larger splitting in the orbitals, which would make it easier to measure. Lastly, it could be considered to use a different system to the CO molecules on a Cu(111) substrate.

Ch.
5

5.9 Acknowledgements

## Chapter 5: Supplementary information

S5.1 Methods

STM/STS measurements were obtained in a Scienta Omicron POLAR SPM Lab at a base temperature of 4.5K which hosts a 5T perpendicular magnet. The base pressure during all experiments was in the 10^{-10} mbar range. STS spectra were obtained using the following parameters: a 2nA current at -0.5V was applied before turning off the feedback loop. A 5mV bias modulation was applied at 973Hz for the lock-in amplifier and 401 points were obtained at 500ms acquisition time per point.

Clean Cu(111) was prepared by repeated cycles of dynamic sputtering of Ar ions at 1kV and 10mA and consequent annealing between 400-500 °C.

Deposition of CO was performed by leaking in CO gas in the STM chamber at a dynamic pressure of $2.5e^{-8}$ mbar for 6 minutes.

Manipulation of CO was performed using a Cu-coated PtIr tip. Molecules were manipulated at currents in the 40-60nA range, with a bias voltage of 10mV.

To **normalize** the different dI/dV spectra the following procedure was used. Before performing STS on the quantum corrals, a Cu(111) background spectrum was obtained with the same settings (see figure S5.1a). The onset of the surface state of the Cu(111) background is then scaled to the onset of surface state present in the *dI/dV* spectrum taken on the quantum corral. The scaled background is then subtracted from the raw STS data.[3,4] As the magnetic field is unable to create electronic states, the area under the 1s or 1p peak can be integrated and normalized to 1 (see figure S5.1b).
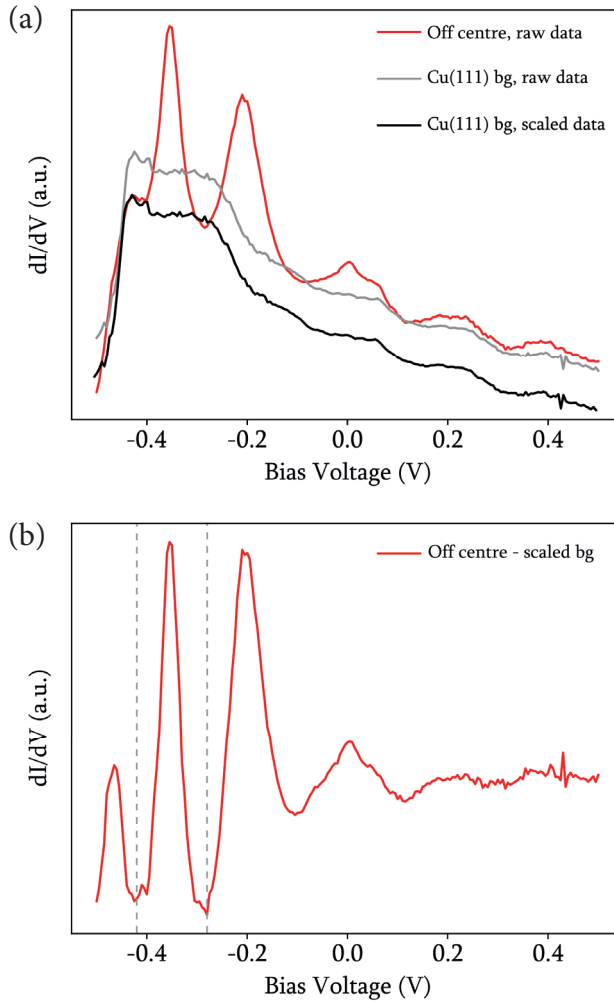
Figure S5.1   **Normalization procedure for dI/dV spectra taken on the quantum corrals**

(a) Raw *dI/dV* spectra taken on the Cu(111) background (grey) and off centre position in the large rectangular corral (red) as well as, scaled Cu(111) background (black). **(b)** Normalized **dI/dV** spectrum of off-centre position in the large rectangular quantum corral divided by the scaled Cu(111) background. The integration boundaries are shown as grey dotted lines at the base of the 1s–peak.
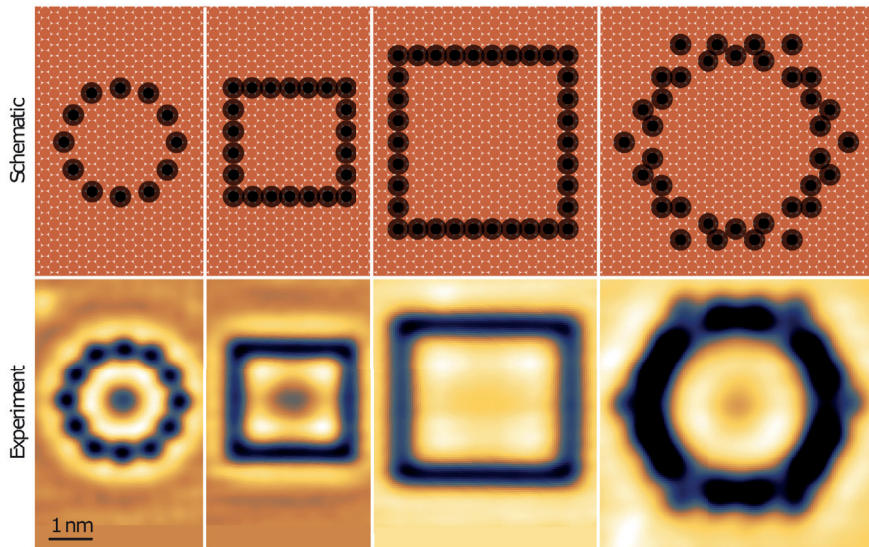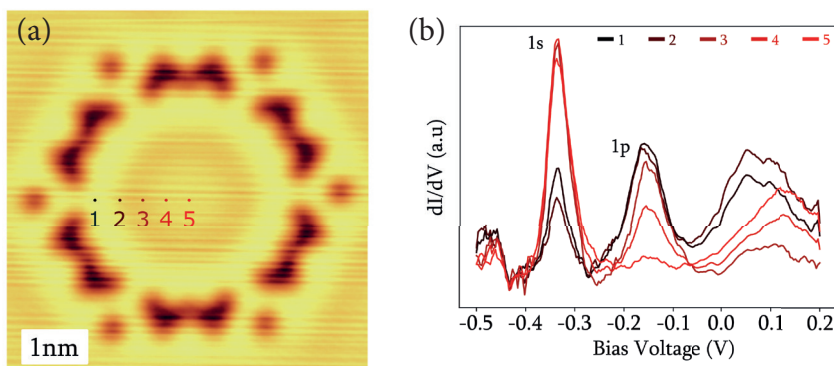
Figure S5.2   Designs and experimental realization of a small circular, small rectangular, large rectangular and large circular (double wall) quantum corral by Thomas Gardenier.[11]

Ch.
5

Figure S5.3: **Characterization of s- and p-orbital in circular quantum corral.**

(a) Constant current topographic image of circular quantum corral displaying the location of the acquired spectra. **(b)** *dI/dV* spectra showing a higher intensity peak in the centre of the corral at -0.35V in energy depicting the s-orbital and a high intensity peak off-centre at -0.15V in energy depicting the p-orbital.

Bibliography

1. Crommie, M. F., Lutz, C. P. & Eigler, D. M. Confinement of electrons to quantum corrals on a metal surface. *Science* **262**, 218–220 (1993).

2. Feynman, R. P. There's plenty of room at the bottom. *Eng. Sci.* **23**, (1960).

3. Gomes, K. K., Mar, W., Ko, W., Guinea, F. & Manoharan, H. C. Designer Dirac fermions and topological phases in molecular graphene. *Nature* **483**, 306–310 (2012).

4. Slot, M. R. *et al.* Experimental realization and characterization of an electronic Lieb lattice. *Nat. Phys.* **13**, 672–676 (2017).

5. Gardenier, T. S. *et al.* p orbital flat band and Dirac cone in the electronic honeycomb lattice. *ACS Nano* **14**, 13638–13644 (2020).

6. Freeney, S. E., van den Broeke, J. J., Harsveld van der Veen, A. J. J., Swart, I. & Morais Smith, C. Edge-dependent topology in Kekulé lattices. *Phys. Rev. Lett.* **124**, 236404 (2020).

7. Slot, M. R. *et al.* p -Band engineering in artificial electronic lattices. *Phys. Rev. X* **9**, 011009 (2019).

8. Freeney, S., Borman, S. T. P., Harteveld, J. W. & Swart, I. Coupling quantum corrals to form artificial molecules. *SciPost Phys.* **9**, 085 (2020).

9. Kiraly, B., Knol, E. J., Rudenko, A. N., Katsnelson, M. I. & Khajetoorians, A. A. Orbital memory from individual Fe atoms on black phosphorus. *Phys. Rev. Res.* **4**, 033047 (2022).

10. Khajetoorians, A. A., Wegner, D., Otte, A. F. & Swart, I. Creating designer quantum states of matter atom-by-atom. *Nat. Rev. Phys.* **1**, 703–715 (2019).

11. Gardenier, T. S. Experiments and simulations for artificial lattices. (Utrecht University, 2022).

12. van den Broeke, Jette. J. Topology, flat bands and magnetic fields in artificial electronic lattices. (Utrecht University, 2021).

13. Ishi, S. & Ohno, Y. An overview on the electronic and vibrational properties of adsorbed CO. *Surface Science* **161**, 349–372 (1985).

14. Ünal, A. A. *et al.* Hybridization between the unoccupied Shockley surface state and bulk electronic states on Cu(111). *Phys. Rev. B* **84,** 073107 (2011).

15. Bartels, L., Meyer, G. & Rieder, K.-H. Basic steps involved in the lateral manipulation of single CO molecules and rows of CO molecules. *Chem. Phys. Lett.* **273,** 371–375 (1997).

16. Bartels, L., Meyer, G. & Rieder, K.-H. Controlled vertical manipulation of single CO molecules with the scanning tunneling microscope: A route to chemical contrast. *Appl. Phys. Lett.* **71**, 213–215 (1997).

17. Fölsch, S., Martínez-Blanco, J., Yang, J., Kanisawa, K. & Erwin, S. C. Quantum dots with single-atom precision. *Nat. Nanotechnol.* **9**, 505–508 (2014).

18. Heinrich, A. J., Lutz, C. P., Gupta, J. A. & Eigler, D. M. Molecule cascades. *Science* **298**, 1381–1387 (2002).

19. Park, C.-H. & Louie, S. G. Making massless Dirac fermions from a patterned two-dimensional electron gas. *Nano Lett.* **9**, 1793–1797 (2009).

20. Klein, J., Léger, A., Belin, M., Défourneau, D. & Sangster, M. J. L. Inelastic-electron-tunneling spectroscopy of metal-insulator-metal junctions. *Phys. Rev. B* **7**, 2336–2348 (1973).

21. Morgenstern, M., Haude, D., Meyer, Chr. & Wiesendanger, R. Experimental evidence for edge-like states in three-dimensional electron systems. *Phys. Rev. B* **64**, 205104 (2001).

22. Kliewer, J. *et al.* Dimensionality effects in the lifetime of surface states. *Science* **288**, 1399–1402 (2000).

Chapter 6:
Dopants in Gallium Arsenide

The semiconductor industry is critical for our current need for information processing. With electronic devices becoming ever smaller, the effect of single dopants in semiconductors becomes increasingly important. In this chapter, we use cross-sectional STM to investigate the electronic properties of different single dopants in a GaAs wafer, the possibility to manipulate Zn dopants in the first layer of GaAs and lastly the effect of tunnelling probability through the GaAs during the ramp of a perpendicular magnetic field. In agreement with previous work, we observe different topographic features as well as distinct electronic features for Si dopants, located in different layers of the substrate, and B dopants in GaAs. Zn dopants incorporated in the surface atomic layer were laterally moved to neighbouring sites, exchanging the Ga atom at the site. Lateral manipulation was achieved by decreasing the tip-sample distance i.e. by increasing the current setpoint from 10pA to 50pA. During lateral manipulation attempts the Zn atom was transferred to the tip about 35% of the time. After picking up the Zn atoms they be deposited back into the surface by scanning over the void with a current setpoint of 20pA. Tunnel probability measurements were performed by sweeping different magnetic fields while in tunnel contact. Changes were observed in the tunnel probability by changes in the tip-sample distance during the magnetic field sweeps. All of these changes were attributed to experimental artifacts as the same changes were observed during magnetic field sweeps on a clean Cu(111) surface.

"Most test subjects do experience some cognitive deterioration after a few months in suspension. Now you've been under for… quite a lot longer, and it's not out of the question that you might have a very minor case of serious brain damage. But don't be alarmed, alright? Although, if you do feel alarmed, try to hold onto that feeling because that is the proper reaction to being told you have brain damage."

–GlaDOS, Portal (2007)

6.1: Introduction

In the past decades the semiconductor industry has experienced immense growth. With applications in computer chips, solar panels, lighting and more, it is not surprising that semiconductors have been the focus of significant scientific interest. At the heart of every mobile phone the group IV semiconductors are dominantly present. Materials such as silicon (Si) and germanium (Ge) have been used to create computer chips, transistors and many more electrical related components. The second group of semiconductors which are widely used in, amongst others, infrared detectors and solar cells, are the III-V semiconductors. These semiconductors contain a group III element, such as Gallium (Ga) or Indium (In), and a group V element, such as arsenic (As) or Phosphor (P). The functionality of semiconductors in electrical components comes from their (small) band gap, in combination with free charge carriers. The number of free charge carriers can be controlled by adding dopant atoms, atoms with either more or less valence electrons compared to the atoms of the host lattice. An example is a Si atom replacing a Ga atom in GaAs. Si, a group IV element, has one more electron in its valence shell than Ga (group III). This additional electron is donated to the conduction band. Si is however an amphoteric dopant and would be able to replace an As atom (group V) in the lattice as well, leading to an additional hole. Semiconductors, where the electrical properties are determined by free electrons in the conduction band, are referred to as n-type semiconductors. Conversely, semiconductors whose conductivity is governed by mobile holes, are known as p-type. With the present day devices reaching the nanometre scale, the number of dopants becomes critical for the functionality of the device. Research shows that in some cases an individual impurity can dominate the transport properties.[1–3] Gaining knowledge on the properties of single dopants is therefore important. Scanning Tunnelling Microscopy (STM) with its atomic scale precision is an ideal technique to study these systems.

Additionally, the STM has the ability to manipulate adsorbates and dopants in different systems.[4–6] By creating structures via atomic manipulation, on a semiconductor surface, it is possible to change the properties of the material which could give rise to interesting physics. It has been shown that this is possible for semiconductors like InAs, InSb and Mn:GaAs.[6–8]

6.2: Cross-sectional STM

The GaAs wafers used here are commercial n-type wafer with a dopant concentration of ~2×10^{18}cm^{-3}. To investigate the dopants, the wafer needs to be cleaved in ultrahigh vacuum (UHV) conditions to ensure the surface is contaminant-free and atomically flat on large scales. The wafer is first thinned down to ~100µm and a scratch is applied along the wafer, it is then mounted vertically in a sample holder. In vacuum the wafer is annealed to remove contaminants before it is mechanically cleaved by applying a force to the front of the wafer,

at the top, cleaving the GaAs along the applied scratch. The exposed plane is a (110) plane of the zinc-blende crystal which presents a cross-sectional surface of the sample, this method is therefore referred to as cross-sectional STM.[9,10]

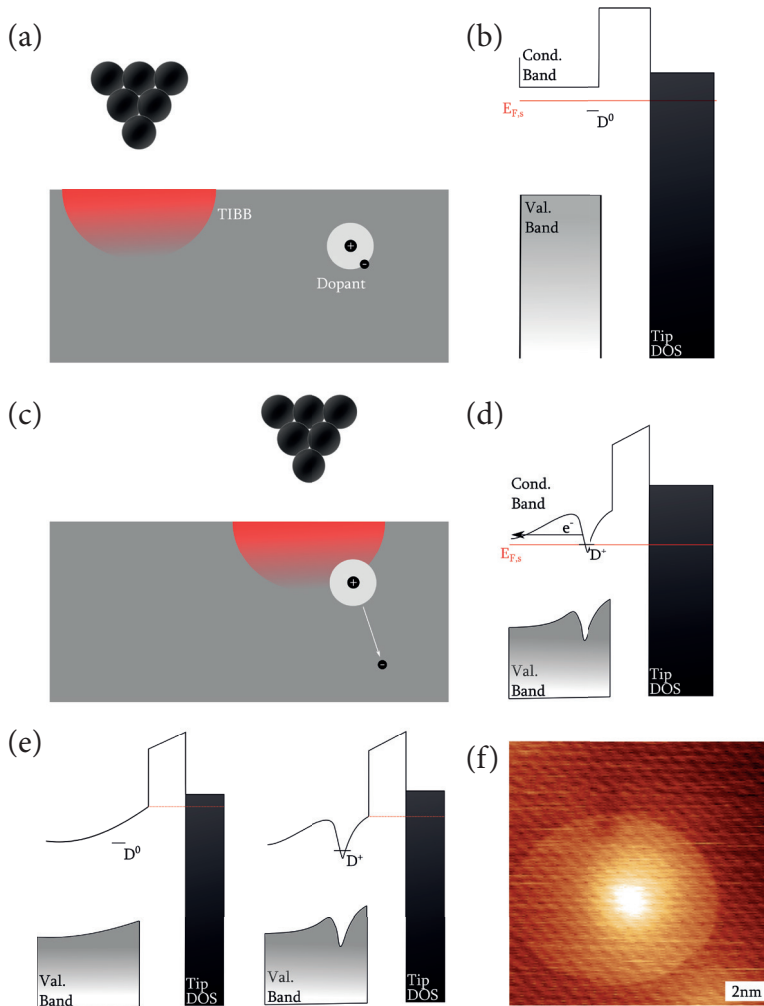## 6.3: Tip induced band bending

Tip induced band bending (TIBB) is the effect the tip has on the band structure of a semiconductor, this effect originates from the electric field present due to the applied bias between tip and sample.[2,11] Figure 6.1 shows a schematic representation of the TIBB effect. When the STM tip is above the semiconductor but laterally far away from a dopant, the dopant is (usually) neutral.[12] In figure 6.1b the Fermi level (red line, $E_{f,s}$) can be seen and the energy level of the neutral dopant (black line, D^0) in between the valence and conduction band which are pulled slightly upwards. When the STM is close to a neutral impurity atom, the donor can be ionized (see figure 6.1c). For this to happen, the TIBB needs to pull the donor state above the Fermi energy (D^+) (see figure 6.1d). In turn, due to the Coulomb potential of the positively charged donor the bands are lowered locally increasing the tunnelling probability (see figure 6.1e). This results in a disc around the dopant with slightly larger apparent height in STM topography images (see figure 6.1f). This is called an ionization ring or charge ring. It has been shown that the diameter and intensity of the ionization rings are dependent on tip shape, tip-sample work function and, more importantly, the depth of the donor dopant.[2] For dopants close to the surface a small ionization ring is observed while larger diameter rings, with lower intensity are seen for donors deeper in the host material. Therefore, the depth and charge state of a dopant can be determined by analysing the size and intensity of the charge rings.

6.4: Results and discussion

6.4.1: Spectroscopic data on different dopants

Two different GaAs wafers were investigated using STM and STS, one wafer with Si and B dopants and the second wafer with Zn dopants. Figure 6.2 shows topography images and *dI/dV* spectra on two Si dopants, a B dopant and GaAs background as well as topography images of a Zn dopant at two different bias voltages. The spectra taken on the bare GaAs, shown in 6.2b,d and f, display a bandgap of ~1.5V which matches previously reported values.[13,14] The constant current topographic images of the different dopants shown in figures 6.2a,c and e display different size and shapes at a bias voltage of -2.5V which is characteristic for dopants in semiconductors.[14–17] The apparant shape of a dopant is dependent on which site the dopant is located, the binding energy, as well as the distance between the surface and the atomic layer in which the dopant is incorporated. For example, Si dopants substitute a Ga atom. At odd layers in the crystal the dopant will be situated in between the surface Ga sites, whereas,

Ch.

6

Figure 6.1: **Tip induced band bending on a donor dopant in a semiconductor sample**

(a) Schematic representation of an STM tip far away (laterally) from a donor dopant. **(b)** Band structure depicting the energy state of the donor in the gap between valence **and** conduction band and the Fermi energy in red ($E_{f,s}$). **(c)** Schematic representation of the STM tip close to the donor dopant (at positive sample bias), ionizing the dopant. **(d)** The donor is ionized when the donor level is pulled above the Fermi level. The additional Coulomb potential of the ionized donor locally lowers the bands. **(e)** When the donor is ionized, the tunnelling probability is enhanced, leading to a retraction of the tip. **(f)** STM topographic image at 2V displaying the ionization ring around a Si donor dopant in GaAs.

in even layers the dopant will be directly underneath the surface Ga sites. The second parameter affecting the shape imaged by the STM is the bias voltage at which the substrate is being imaged. At large negative voltages, < -3V, the tunnelling pathway goes through the A_4 and A_5 surface states which are coming from the As atoms in the lattice, whereas the corrugation at positive voltages comes from the C_3 and C_4 surface states originating from the Ga sublattice.[18,19]

Figure 6.2b shows two distinguisable features when compared to the GaAs background. First, an increase in intensity at the edge of the conduction band between 0.5V and 1.5V is observed. As mentioned, these are the C_3 and C_4 surface states of the GaAs substrate. The TIBB effect will shift these features to lower voltages making them visible in the *dI/dV* spectrum on the dopant. The second feature is a small peak around -1.1V, which has been documented to be a feature present in Si dopants in odd layers of the semiconductor, however in literature the feature at this energy is quite pronounced which is not the case in this measurement.[2] It was suggested that this is a filled–state wave-function for a second electron bound to the donor the donor. These spectroscopic features in combination with the shape were compared to literature,[17] leading to the conclusion that this is a Si dopant in the first GaAs layer.

The STM image at a bias voltage of -2.5V of the second dopant (figure 6.2c) shows a different shape and a lower apparent height than the image on the Si dopant in the first layer. Literature shows that this is likely to be an Si dopant in the second layer.[2,17] Lastly, the STM image at the same bias voltage on a third type of dopant (figure 6.2e) shows a different shape with three lower intensity 'legs' on one side and two higher intensity 'legs' on the opposite side. This is characteristic for a B dopant in the first layer of the GaAs, as shown by Krammel *et al.*[14]

In the *dI/dV* measurements on the Si dopant in the second layer and the B dopant in the first layer (figures 6.2d and 6.2f, respectively), a sharp peak is visible between -0.5V and -1V, which is in the bandgap of the semiconductor. This is attributed to a dopant state of the Si and the B respectively, creating a strong tunnel path between dopant and tip. For the Si dopant this state is close to the conduction band, in agreement with it being an electron-donor.[20] The electronic state of the B dopant is closer to the valence band, however it has been shown that this state is still an electron–donor state.[21] Due to the TIBB effect the state around –0.7V is related to the conduction band and not to the valence band. Furthermore, for the dI/dV spectrum on the B dopant a relatively broad peak is observed around -1.5V (see figure 6.2f), which can be attributed to the TIBB. The downward bending of the band causes the B dopant state to drop below the Fermi level. However since the B impurity state is always occupied there is a strong tunnelling pathway to the tip.[2,14]

In a second GaAs wafer, Zn dopants were identified by the shape of the dop-

Ch. 6

ants in constant current topographic images at different bias voltages, shown in figure 6.2g and h, rather than their electronic signature. At a bias voltage of 1.6V the Zn dopant has a very characteristic shape, whereas at a bias voltage of 2V the apparent shape of the dopant is a circular protrusion with a slight dark depression around it. The differences in apparent shape of the Zn dopants in different layers of the GaAs host lattice are well documented, as a 50mV difference in the bias voltage can result in a significantly different appearance of the Zn dopant.[15,22] By comparing figures 6.2g and h with literature it was concluded that these are Zn dopants in the first layer of the GaAs host lattice.

To conclude, using STM, the nature of dopant atoms in GaAs can be determined from its shape in topographic STM images, combined with its differential conductance signature.

6.4.2: Atomic manipulation of Zn dopants in GaAs

Being able to manipulate dopants with the STM tip offers the possibility to use GaAs as a system for creating artificial lattices. Furthermore, being able to manipulate the dopants in a semiconductor could be used to determine if certain configurations of dopants can influence the electronic properties of the semiconductor. Zinc (Zn) dopants in the first layer of a GaAs wafer were investigated to see if these dopants could be used for vertical or lateral manipulation.

Figure 6.3a shows two first-layer Zn dopants. It was attempted to move the left dopant by placing the STM on the edge of the dopant (noted as a red x in the image) and increasing the current setpoint. By increasing the current setpoint the tip-sample distance is decreased and therefore the tip exerts more force on the dopant. Figure 6.3b shows a typical Z(t) height trace taken during the manipulation attempt (a more negative Z(t) value means closer to the surface). It is noted where the current was increased from 10 pA to 50 pA (with $V = 2$V) leading to a tip height decrease of ~60pm. After 10-15 seconds, a spontaneous decrease in tip height is observed, we assume that this corresponds to the Zn dopant hopping to the next crystallographic site. The second panel of figure 6.3a shows the result after the manipulation attempt. Indeed, the Zn dopant moved to the north-east of its starting position. By using the Zn atom located on the right hand side of the image as a reference, we can determine by how much the Zn atom moved. First, by counting the number of atomic rows in the image, it is clear that the atom has moved one atomic row to the right. Furthermore, by comparing the vertical distance between the atoms before and after the manipulation, we find that it has moved up by ~0.75 nm. Hence, the total distance the Zn atom has moved is ~0.90 nm, corresponding to a next-next-nearest neighbour Ga atom in an adjacent dimer row (depicted as a red arrow in figure 6.4a).[23] This confirms the finding that Zn atom substitutes a Ga atom in the surface. Note that this manipulation corresponds to an *interchange* of two atoms in the surface, not merely the displacement of a single atom as is the case in most lateral manipulation experiments.
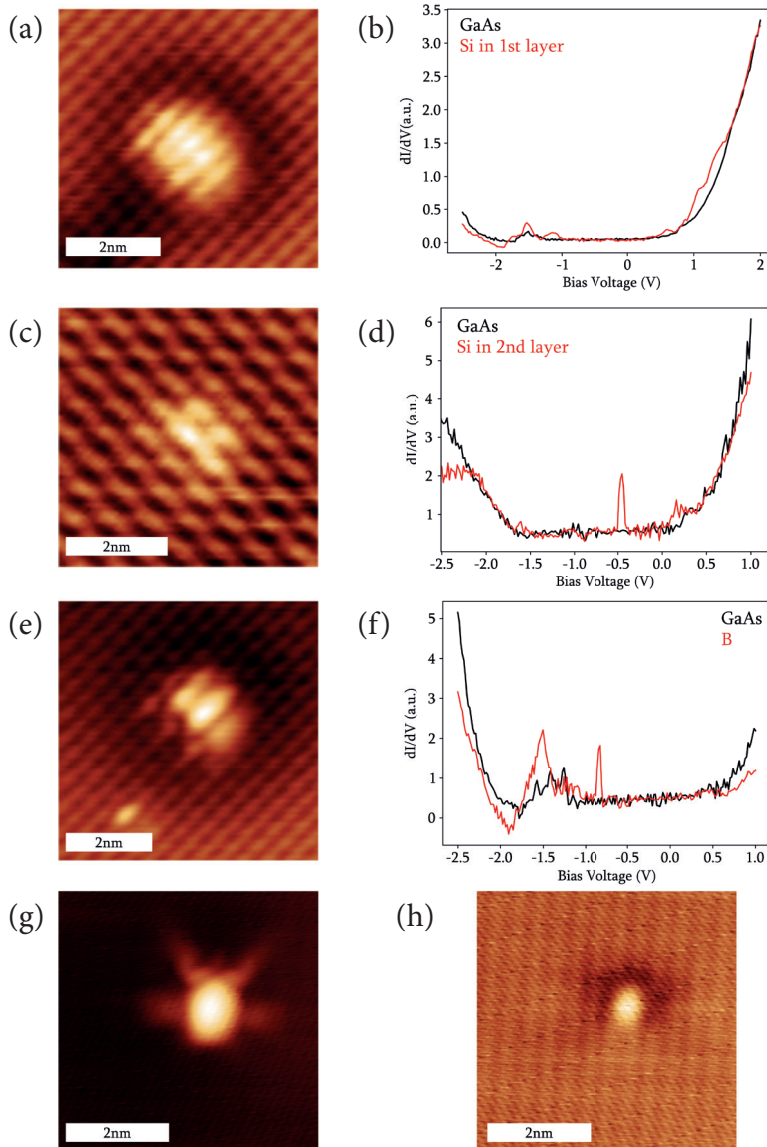
Figure 6.2: **Characterization of different dopants in GaAs using STS and STM.**

(a,c,e) Constant current topography images at a bias voltage of –2.5V on a Si dopant in the first layer, a Si dopant in the second GaAs layer and a B dopant, respectively. (b,d,f) *dI/dV* measurements on top of the dopants shown in (a, c and e respectively) and GaAs background. (g,h) Constant current STM images of a Zn dopant in the first GaAs layer at a bias voltage of 1.6V (g) and 2.0V (h).

Figure 6.4a shows a schematic top view and side view of a Zn dopant in the first layer of a GaAs host lattice including the observed successful manipulations to a nearest neighbour (green arrow), next-nearest neighbour (blue arrow) and next-next-nearest neighbour (red arrow) Ga site. Interestingly, all successful manipulations were to the next dimer row, no manipulations in the same row were observed. When the Zn dopant is not laterally manipulated to the closest Ga site in the lattice (green arrow) but to a different Ga site in the same row (blue and red arrow) it can be seen that the Zn atom has to move over or around the As atom when substituting a Ga atom. In the side view however it can be seen that the top layer of the GaAs lattice is buckled i.e. the As atoms are pushed slightly up creating an extra obstacle for the substituted Ga atom to reorder when replaced with a Zn atom.[19]

During several manipulation attempts the Zn dopant disappeared leaving a high intensity void, shown in figure 6.3d. The high intensity of the void suggests that there is a vacancy, possibly with a state similar to states seen for chlorine vacancies in a sodium chloride surface.[24,25] A typical height trace corresponding to such an event is shown in figure 6.3e. In contrast to the trace in Fig. 6.3b, a sudden retraction of the tip is observed (upwards jump after, in this case, 50s). This is in agreement with the larger apparent height of the void. Hence, as the Zn atom is removed from the surface, the tip has to retract to maintain the same tunnelling current. By scanning over the hole left in the surface with a current setpoint of 20pA (at 2V bias voltage) the Zn dopant was transferred back from the tip to the surface into the atomic void, which can be seen in the bottom panel of figure 6.3d. The fact that the Zn atom can be manipulated laterally and be picked up, in combination with the fact that a Zn and Ga atom must switch positions, suggests that during a successful manipulation attempt, the Zn atom is partially pulled out of the substrate and moves over the As and Ga atoms (as opposed to an in-plane reordering of the atoms).

Out of 20 manipulation attempts, the Zn dopant was laterally manipulated 10 times, however the directional control was limited as can be seen in figure 6.4b, no manipulations of Zn atoms were observed in the same dimer row or to a further dimer row. Due to limited statistics, it cannot be concluded that these manipulations are not possible. Manipulation attempts resulted in one of three substitutions, with the distances schematically drawn in figure 6.4a. Almost all manipulation attempts were conducted with the same atomically configured tip. The shape of the tip could heavily influence the possibility to manipulate atoms in certain directions and with atomic precision, therefore a more statistical approach is needed to gain control over the lateral atomic manipulation of Zn dopants in the first layer of GaAs. Furthermore, during the lateral manipulation attempts the Zn atom was transferred to the tip 7 times and 3 times no change in configuration was observed. In order to build artificial lattices, more control over the process is required, i.e. the success rate for lateral

manipulations must be increased. more experiments are required to establish the influence of e.g. current and bias voltage setpoints, as well as different tip placements. The latter may be used to control the direction in which manipulation occurs.[26] A second focus of research could be to investigate whether the picked up Zn atoms can be placed on the surface of GaAs rather than placed back in the hole leading to the possibility of vertical atom manipulation. Finally, it should be investigated if the manipulation is unique for Zn dopants, or if it is also applicable to other types of atoms.

Ch. 6
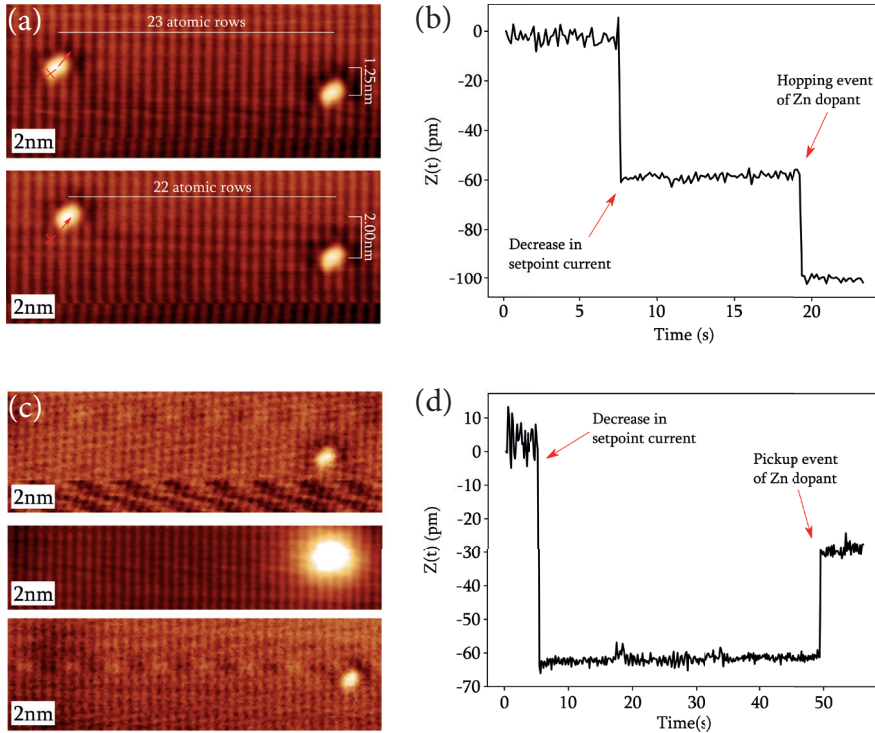
Figure 6.3:   **Manipulation of Zn dopants in GaAs**

(a) Constant current topographic image before and after moving of Zn dopant including tip location (denoted as an x in the image taken before hopping of the dopant). **(b)** Height trace of the STM tip during a lateral manipulation event of Zn dopant, including the moment of the increase of tunnel current from 10pA to 50pA and the hopping event of the Zn dopant. **(c)** From top to bottom: Constant current topographic image before and after picking up a Zn dopant, as well as after redeposition. All topographic images were taken a $V = 2V$. **(d)** Height trace of the STM tip during pick-up event of Zn dopant including the moment of the increase of tunnel current from 10pA to 50pA and the pickup event of the Zn dopant. Note, for the height traces, a more negative Z(t) value means closer to the surface.
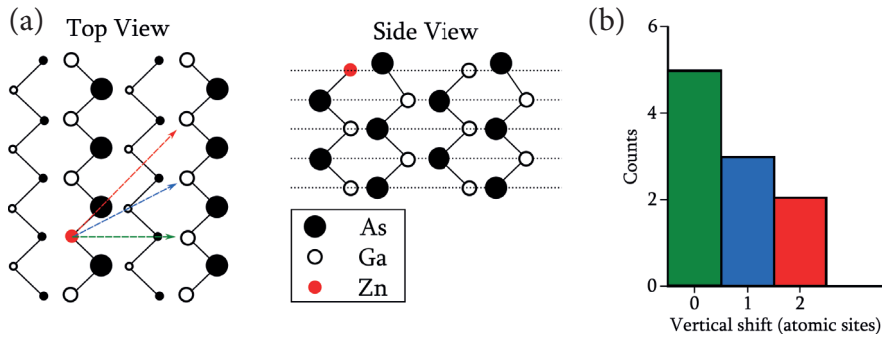
Figure 6.4: **Schematic representation of lateral manipulation pathways of Zn dopants in GaAs.**

(a) A schematic top and side view of zinc-blende (110) GaAs with Ga atoms as open circles, As atoms as black closed circles and a Zn dopant as red closed circle. The red, blue and green arrow depict the observed successful manipulations for one direction to a nearest neighbouring site (green arrow), next-nearest neighbouring site (blue arrow) and next-next-nearest neighbouring site (red arrow). **(b)** The amount of successful manipulations following the pathways depicted in (a)

6.4.3: Tunnelling probability through GaAs under influence of a perpendicular magnetic field

To gain more insight into the behaviour of doped GaAs under the influence of a perpendicular magnetic field, the tunnelling probability during different magnetic field ramps was measured. The STM tip was positioned over the GaAs substrate as well as on top of a Zn dopant. Tunnelling feedback was maintained while perpendicular magnetic field ramps were performed of different field strengths. As the feedback loop regulates the height of the tip at a current setpoint, changes in the tip height reflect a change in tunnelling probability. If the tip retracts the tunnelling probability is increased and vice versa.

In figure 6.5a tip height traces can be seen, while in tunnel contact (at a current setpoint of 0.1nA at a bias voltage of 1.6V), on GaAs during a perpendicular magnetic field ramp. With the blue trace measured during a field ramp from $B = 0$T to $B = 0.5$T, subsequently the red trace was measured at a field ramp from $B = 0.5$T to $B = -0.5$T and lastly the black trace was measured at a field ramp from $B = -0.5$T to $B = 0.5$T. The first observation is a sudden increase in tip height while starting the ramp, and a sudden decrease can be seen at the end of the ramp of the magnetic field. Such events were always observed at the start and end of a magnetic field ramp, and for different materials such as Cu(111) and were therefore attributed to an artifact of the STM/electronics, see

figure 6.4b. Secondly, a U-shape profile can be seen for the height traces mean-
ing that there is lower tunnelling probability at lower magnetic fields with the
exception close to 0T where a slight increase is observed in the tip height. This
behaviour was also observed for tip height measurements on a clean Cu(111)
surface (see figure 6.5b). It can therefore be concluded that this behaviour is not
unique to semiconductors and might be originating from a magnetic field effect
on the tip, electronics or other STM components.

Upon an initial tip height measurement from $B = 0T$ to $B = 0.5T$ the tip first
gradually approaches the surface followed by a retraction following the U-shape
profile discussed before. When subsequently ramping the field from $B = 0.5T$
to $B = -0.5T$, the tip approaches the sample again following the same trend.
Interestingly, at $B = -0.25T$ the retraction of the tip shows an acceleration
meaning a quick increase in tunnelling probability until it reaches a plateau.
Upon a reverse of the magnetic field ramp back from $B = -0.5T$ to $B = 0.5T$ the
opposite is observed: the tip gradually approaches the surface but an accelerat-
ed increase in tunnelling probability is observed at $B = 0.25T$. This results in
a hysteresis in the Z(B) curves, symmetric around $B = 0T$. This behaviour was
observed for multiple tip configurations (including with a Zn atom at the tip
apex) and locations on the GaAs (including on top of a Zn dopant). Additional
examples are shown in figure S6.1. This behaviour was however not observed
for magnetic field ramps from $B = 0T$ to $B = 1T$ as shown in figure 6.5b. This
suggests that the history of the magnetization is important for the hysteresis
effect.

Ch.
6

To investigate whether the hysteresis effect is originating from the GaAs wafer
or from an experimental artefact, similar measurements were performed on a
Cu(111) crystal, shown in figure 6.5c. The initial approach of the tip from the B
$= 0.5T$ or $B = -0.5T$ to $B = 0T$ has now changed to an increase in tip height.
An explanation could be drift or creep of the scanner piezo (the experiments
were performed 30 minutes after approaching). Importantly, an accelerated in-
crease in tunnelling probability is again observed at $B = \pm0.25T$ after the
magnetization is flipped in both measurements. This observation suggests that
the hysteresis in Z(B) traces on GaAs originates from an artifact in the STM
system rather than a physical characteristic of the semiconductor. To confirm
this hypothesis, more measurements should be performed on Cu(111) and GaAs
at different bias voltages and after proper stabilization of the tip after approach.
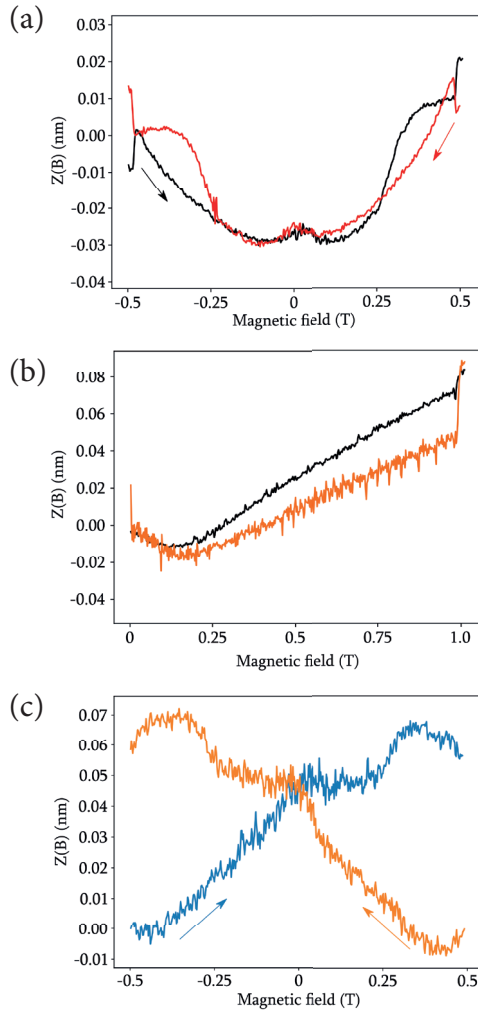
Figure 6.5: **Z(B) traces of the tip height on GaAs and Cu(111) surface while ramping a perpendicular magnetic field**

(a) Z(B) trace on GaAs from B = -0.5T to B = 0.5T (black) and subsequently from B = 0.5T to B = -0.5T (red). The black and red arrows display the direction of the magnetic field ramp. The traces were offset to mitigate the artifact (sudden jump) introduced at the beginning and end of the magnetic field ramp. Feedback setpoint: 0.1nA at 1.6V. (b) Z(B) trace on GaAs (black) and Cu(111) (orange) from B = 0T to B = 1T. Feedback setpoints: 0.1nA at 1.6V for GaAs and 0.1nA at 0.5V for Cu(111). (c) Z(B) trace on Cu(111) from B = 0.5T to B = -0.5T (orange) and subsequently from B = -0.5T to B = 0.5T (blue). The orange and blue arrows indicate the direction of the magnetic field ramps.

6.5: Conclusion and outlook

Gallium Arsenide wafers with different dopants have been investigated using STM and STS. Spectroscopy was performed on Boron and Silicon dopants in different layers of the GaAs. Atomic manipulation was used to move and pick up Zinc dopants in the first GaAs layer. Finally the tunnelling probability through GaAs under influence of a perpendicular magnetic field was investigated.

In agreement with literature, we observed that Si dopants showed differences in intensity and lateral dimension, depending on the depth at which the Si is located. B dopants show a distinct asymmetry with three lower intensity legs on one side of the dopant and two higher intensity legs on the other side. STS was used to further determine the differences in the electronic structure of the dopants. For Si, an in-gap electronic state relatively close to the onset of the conduction band was observed, in agreement with Si being an n-type dopant in GaAs. It was also observed how the imaged shape of a Zn dopant in the first layer of GaAs changes depending on the applied bias voltage, compliant with literature.

The STM tip was used to induce lateral movement of Zn dopants, located in the first layer of GaAs, to neighbouring lattice sites by placing the tip on the edge of the dopant and reducing the current setpoint from 10pA to 50pA (at a bias voltage of 2V). In this process, the Zn dopant substitutes a Ga atom in the host lattice which fills the void left by the Zn dopant. Additionally, it was observed that ~1/3 of the manipulation attempts resulted in a pick-up event. The Zn dopant could easily be transferred back from the tip apex to its original position in the GaAs lattice by scanning over the vacancy with a current setpoint of 20pA (at a bias voltage of 2V). This suggests that during the manipulation, Zn atoms are partially pulled out of the substrate, rather than an in-plane exchange of atoms.

A hysteresis was found when comparing tip height traces while in feedback on GaAs during magnetic field ramps between $B = -0.5T$ and $B = 0.5T$. After the change of direction of the magnetic field during the ramp an accelerated increase in tip height was observed, i.e. an accelerated increase in tunnelling probability. This increase was observed in both ramping directions but not observed in ramps from $B = 0T$ to $B = 1T$. Additional experiments were performed on a Cu(111) surface and a similar effect was found. This suggests that it is related to the STM setup rather than an intrinsic quality of the GaAs.

Additional experiments need to be performed to gain more insight in the physics at play in doped semiconductor samples. First, STS measurements on different dopants needs to be performed to gain full insight in the workings of dopants on the band structure of GaAs. Secondly, an extensive statistical research

Ch.
6

needs to be performed to determine how to controllably manipulate Zn (and possibly other dopants) in GaAs. The following parameters could be changed to determine how to move Zn dopants both laterally and vertically: current setpoint, bias voltage, tip positioning, tip termination. Especially the prospect of depositing Zn atoms by vertical manipulation could create a reliable system for the building of artificial lattices. Thirdly, the hysteresis found in the tip height during perpendicular magnetic field ramps could be examined further by performing $Z(B)$ experiments Cu(111) and GaAs with different parameters and after proper relaxation after the tip approach.

6.6 Acknowledgements

## Chapter 6: Supplementary information

S6.1 Methods:

STM/STS measurements were obtained in a Scienta Omicron POLAR SPM Lab at a base temperature of 4.5K which hosts a 5T perpendicular magnet. The base pressure during all experiments was in the 10^{-10} mbar range.

STS spectra were obtained using the following parameters, a 0.1nA current at -2.5V was applied before turning off the feedback loop. A 20mV bias modulation was applied at 973Hz for the lock-in amplifier and 401 points were obtained at 100ms acquisition time per point.

Z(t) traces were obtained at 0.1nA current at 1.6V bias voltage on GaAs and 0.1nA at 0.5V on Cu(111). The external magnetic field was ramped during the Z(t) measurements with 0.005A/s ramp rate.

The **GaAs wafers** were grown using MBE. For the Zn doped GaAs with Mn doped GaAs layers the following wafer was grown.

- Zn doped (p-type) GaAs
- 200nm 2e17 GaAs:Mn
- 1ML AlAs
- 5nm 2e19 undoped GaAs
- 1ML AlAs
- 50nm 2e18 GaAs:Mn
- 1ML AlAs
- 50nm 2e19 GaAs:Mn
- 1ML AlAs
- 50nm 2e20 GaAs:Mn

Ch.
6
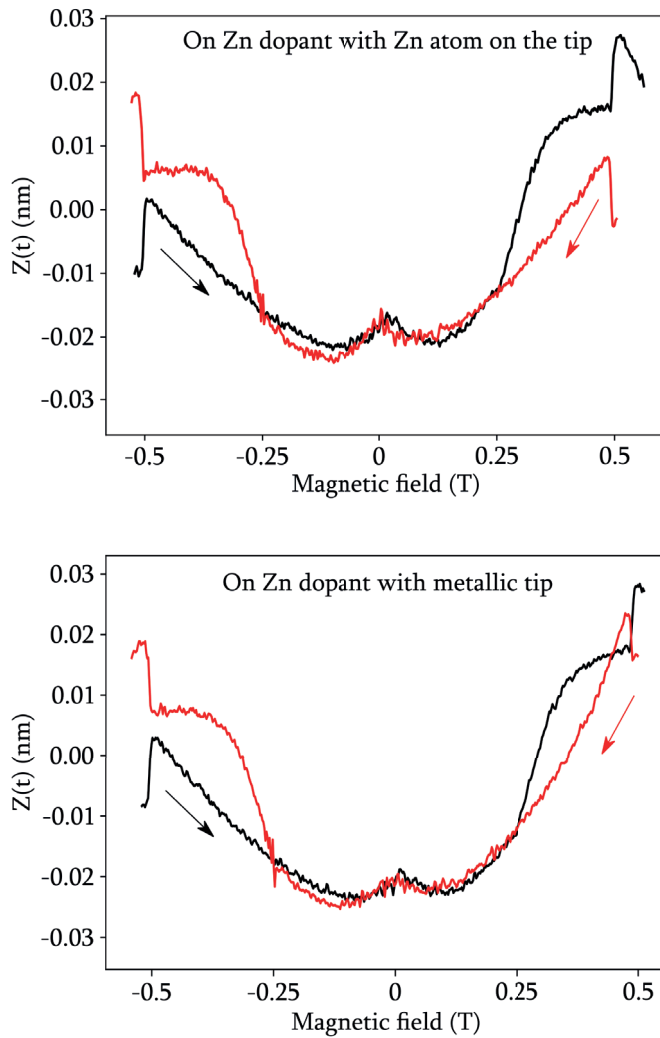
Figure S6.1:   **Z(t) traces of the tip height on a Zn dopant in GaAs**
Z(t) trace on a Zn dopant in GaAs with a mettalic tip and after picking up a Zn atom
from the surface. The magnetic field ramps are from $B = -0.5$T to $B = 0.5$T (black) and
subsequently from $B = 0.5$T to $B = -0.5$T (red). The black and red arrows display the
direction of the magnetic field ramp. The traces were offset to overlap the traces after
the artifact introduced at the beginning and end of the magnetic field ramp. Feedback
setpoint: 0.1nA at 1.6V.

Bibliography

1. Sellier, H. *et al.* Transport spectroscopy of a single dopant in a gated silicon nanowire. *Phys. Rev. Lett.* **97**, 206805 (2006).

2. Wijnheijmer, A. P. *et al.* Single Si dopants in GaAs studied by scanning tunneling microscopy and spectroscopy. *Phys. Rev. B* **84**, 125310 (2011).

3. Lansbergen, G. P. *et al.* Gate-induced quantum-confinement transition of a single dopant atom in a silicon FinFET. *Nat. Phys.* **4**, 656–661 (2008).

4. Gomes, K. K., Mar, W., Ko, W., Guinea, F. & Manoharan, H. C. Designer Dirac fermions and topological phases in molecular graphene. *Nature* **483**, 306–310 (2012).

5. Eigler, D. M. & Schweizer, E. K. Positioning single atoms with a scanning tunnelling microscope. *Nature* **344**, 524–526 (1990).

6. Fölsch, S., Martínez-Blanco, J., Yang, J., Kanisawa, K. & Erwin, S. C. Quantum dots with single-atom precision. *Nat. Nanotechnol.* **9**, 505–508 (2014).

7. Sierda, E. *et al.* Quantum simulator to emulate lower-dimensional molecular structure. *Science* **380**, 1048–1052 (2023).

8. Kitchen, D., Richardella, A., Tang, J.-M., Flatté, M. E. & Yazdani, A. Atom-by-atom substitution of Mn in GaAs and visualization of their hole-mediated interactions. *Nature* **442**, 436–439 (2006).

9. Kato, T. & Tanaka, I. A scanning tunneling microscopy/spectroscopy system for crosssectional observations of epitaxial layers of semiconductors. *Rev. Sci. Instrum.* **61,** 1664-1667 (1990).

10. Mikkelsen, A. & Lundgren, E. Cross-sectional scanning tunneling microscopy studies of novel III–V semiconductor structures. *Prog. Surf. Sci.* **80**, 1–25 (2005).

11. Teichmann, K. *et al.* Controlled Charge switching on a single donor with a scanning tunneling microscope. *Phys. Rev. Lett.* **101**, 076103 (2008).

12. Giorgi, G. *et al.* Doping of III–V arsenide and phosphide wurtzite semiconductors. *J. Phys. Chem. C* **124,** 27203–27212 (2020).

13. Schlesinger, T. E. *Gallium Arsenide. in Encyclopedia of Materials: Science and Technology* (eds. Buschow, K. H. J. *et al.)* 3431–3435 (Elsevier, Oxford, 2001).

14. Krammel, C. M., Nattermann, L., Sterzer, E., Volz, K. & Koenraad, P. M.

Ch.
6

Structural and electronic properties of isovalent boron atoms in GaAs. *J. Appl. Phys.* **123**, 161589 (2018).

15. de Kort, R., *et al.* Zn- and Cd-induced features at the GaAs(110) and InP(110) surfaces studied by low-temperature scanning tunneling microscopy. *Phys. Rev. B* **63**, 125336 (2001).

16. Verstijnen, T. J. F., Tjeertes, D., Banfi, E. G., Zhuang, Q. & Koenraad, P. M. Atomic scale analysis of N dopants in InAs. *Phys. Rev. B* **108**, 045302 (2023).

17. Tjeertes, D. *et al.* Atomic-scale study of Si-doped AlAs by cross-sectional scanning tunneling microscopy and density functional theory. *Phys. Rev. B* **104**, 125433 (2021).

18. Chelikowsky, J. R. & Cohen, M. L. Self-consistent pseudopotential calculation for the relaxed (110) surface of GaAs. *Phys. Rev. B* **20**, 4150–4159 (1979).

19. de Raad, G. J., Bruls, D. M., Koenraad, P. M. & Wolter, J. H. Interplay between tip-induced band bending and voltage-dependent surface corrugation on GaAs(110) surfaces. *Phys. Rev. B* **66**, 195306 (2002).

20. Northrup, J. E. & Zhang, S. B. Dopant and defect energetics: Si in GaAs. *Phys. Rev. B* **47**, 6791–6794 (1993).

21. Pätzold, O., Gärtner, G. & Irmer, G. Boron site distribution in doped GaAs. *Phys. Status Solidi B* **232**, 314–322 (2002).

22. Wijnheijmer, A. P., Garleff, J. K., v. d. Heijden, M. A. & Koenraad, P. M. Influence of the tip work function on scanning tunneling microscopy and spectroscopy on zinc doped GaAs. *J. Vac. Sci. Technol. B Nanotechnol. Microelectron. Mater. Process. Meas. Phenom.* **28**, 1086–1092 (2010).

23. de Raad, G. J., Bruls, D. M., Koenraad, P. M. & Wolter, J. H. STM observations of GaAs(110) showing the top and bottom zig-zag rows of the surface. *Phys. Rev. B* **64,** 075314 (2001).

24. Repp, J., Meyer, G., Paavilainen, S., Olsson, F. E. & Persson, M. Scanning tunneling spectroscopy of Cl vacancies in NaCl films: strong electron-phonon coupling in double-barrier tunneling junctions. *Phys. Rev. Lett.* **95**, 225503 (2005).

25. Tahini, H. A., Chroneos, A., Murphy, S. T., Schwingenschlögl, U. & Grimes, R. W. Vacancies and defect levels in III–V semiconductors. J. *Appl. Phys.* **114**, 063517 (2013).

26. Swart, I., Sonnleitner, T., Niedenführ, J. & Repp, J. Controlled lateral manipulation of molecules on insulating films by STM. *Nano Lett.* **12**, 1070–1074 (2012).

Ch.
6

Chapter 7: Summaries and Appendix

English summary

The invention and development of the Scanning Tunnelling Microscope (STM) enables scientists to study systems as small as single atoms. The functionality of these microscopes have extended and diversified in the last three decades. For instance, it is now possible to study the topography and electronic structure of single dopants in the first atomic layers of a semiconductor, investigate chemical changes in a single molecule and even manually reposition single atoms on an atomically flat surface. In this thesis, I have studied the relation between the atomic and electronic structure of three very different systems, my study includes if and how the electronic structure is affected by an external magnetic field. First the electronic properties of nanoscale platelets made from bismuth selenide (Bi_2Se_3) are investigated. Next, circular and square artificial atoms are created by manually creating corrals out of carbon monoxide molecules. Then their electronic properties are investigated with and without an external magnetic field. Finally, individual dopants in a semiconductor are examined for their electronic properties and their potential as a building block for artificial lattices. We also examined how the tunnelling current varied under the influence of a perpendicular magnetic field.

Scanning tunnelling microscopy

The word microscope finds its origin in the Greek words for "small" (mikros) and "to look at" (skopein). For most people, the word microscope will be associated with the high school biology classes of looking at cells and other organic material with an optical microscope. The scanning tunnelling microscope (STM) gives a new meaning to the words "Mikros" and "Skopein". First of all, an STM does not use light to "look" at small systems but rather employs an atomically sharp needle or tip. This needle is brought in close proximity (about 0.000000001 metres) to a conducting surface and when a bias voltage is applied, electrons can jump from the needle to the conductive sample through the vacuum, closing the loop, and creating a current. Classically this is inconceivable, this is however a quantum mechanical effect called tunnelling. The current due to the tunnelling effect is exponentially dependent on the distance between the tip and the surface. By moving the tip across the surface, very small height differences on the sample can be measured due to changes in the current. It is even possible to "look at"/"feel" the atoms in the sample surface or even single atoms adsorbed on top of the surface. One can think of the needle in the STM similar to the needle of a record playing moving over the surface of a record. Figure 7.1a shows a surface of Lead atoms with every yellow circle being one Lead atom in the crystallographic surface. On the right side, a drop in intensity can be seen indicating that, there, the surface goes one atomic step "down".

A second function of the STM is measuring the electronic properties of the sample in the area directly below the tip. By keeping the tip stationary above a location on the surface, the tunnelling current can be measured as a function of the applied bias voltage, this is called spectroscopy. When there are energy states available at a bias, it is easier for the electrons to tunnel, resulting in a step in the current. The combination of imaging the sample surface with atomic resolution and measurement of the electronic properties of the area underneath the tip is very useful for fundamental scientific research. In this thesis, three different systems are investigated in the STM, ranging from single atoms in a semiconductor to platelets synthesized in a lab with a thickness of only a few nanometres. For most of the experiments the effect of a magnetic field on these small systems is probed.

The height of the tip above the surface can also be used as a tool for scientific research. For example, it is possible to use the needle to move individual atoms with extreme precision. Normally, the needle will be too far away from the atoms on top of the surface to have an effect on them. However, if the distance between the tip and sample is reduced, the tip will interact with the atom on top of the surface. In such a way, one is able to push or pull an adsorbed atom over the surface, this is called atomic manipulation, which can be used to build all kinds of artificial structures, and study their physical properties. Research-ers at IBM showed that atomic manipulation can also be used for fun and ad-vertisement by creating a stop-motion video named "a boy and his atom". The tip height itself can also be a tool to gain information about the possibility for the electrons to transfer between the tip to the sample. When it is easier for the electrons to transfer the tip-sample distance can be larger to have the same current flow. All the just presented techniques have been used in the different projects covered in this thesis, this will be explained below.

In **chapter 3** the energy states of Bismuth Selenide (Bi_2Se_3) nanoplatelets were investigated in the STM. The nanoplatelets were synthesized in the laboratory in such a way that they are only a few nanometres in thickness. It was shown that the states at the top and the bottom of the material cancel each other out when the platelets are thin enough. Using the location specific techniques of the STM, it was shown that only a single state remains at the edge of the platelet, which could be visualized as a bright ring around the entire platelet as shown in figure 7.1b. Two different theoretical models were then used to model the electronic structure of the platelets and explain the experimental findings.

The robustness of these edge states in Bi_2Se_3 nanoplatelets against disorder, an applied magnetic field, and magnetic adsorbents was investigated in **chapter 4**. By looking at nanoplatelets with defects and structural irregularities it was shown that the edge state is very robust against disorder. Moreover, even a 5 Tesla magnetic field doesn't break the state. However, when Mn atoms are deposited on the platelets, the state can be broken.
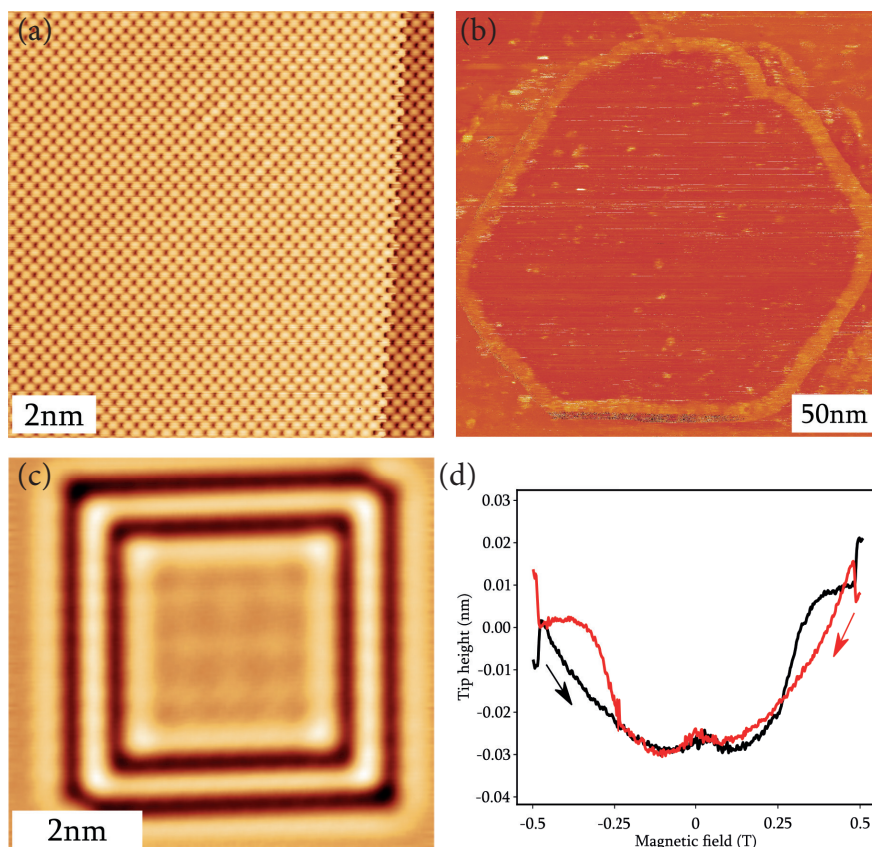
(a) An STM image of an atomically flat surface of Lead with the individual atoms shown as yellow dots neatly arranged. On the right hand side an atomic step is seen as a change in intensity. **(b)** An STM image at the specific energy of the state at the edge of the nanoplatelet which therefore shows in the image as a bright ring along the circumference of the platelet. **(c)** A square quantum corral build from carbon monoxide molecules (black) on a copper crystal (yellow). **(d)** Two traces of the tip height during magnetic field ramps showing an unexpected behaviour. The direction of the magnetic field ramp is shown with the black and red arrows.

Chapter 5 describes the creation of quantum corrals by manually position-ing Carbon Monoxide (CO) molecules on a copper surface. When placed in a circle or a square these electron-repelling molecules confine the electrons of the copper surface. As a result, an artificial atom is created, a square artificial atom can be seen in figure 7.1c. Such artificial atoms are then subjected to a

magnetic field, and it is investigated in how far this affects the electronic states. Theoretically it is shown that there are two effects that split the energy states: the Zeeman effect and the Lorentz force. Experimentally it was impossible to replicate these results

The last project is described in **chapter 6** of this thesis and focusses on dopant atoms in a semiconductor, Gallium Arsenide (GaAs). It is shown how the STM can be used to determine the electronic properties of single dopants. Moreover, we investigated to what extent such dopants can be used to build artificial structures (like the ones in chapter 5) and how the height of the tip can be used to research the effect of a magnetic field on the tunnelling probability through the GaAs surface. Especially the last part of the research shows an unexpected result with the STM tip behaving differently depending on the direction of the magnetic field ramps between -0.5T and 0.5T, as shown in figure 7.1d. This difference couldn't be explained with the measurements in this work but shows how there will always remain scientific questions to be answered.

Ch.
7

Nederlandse samenvatting

De uitvinding en ontwikkeling van de eerste rastertunnelmicroscoop (RTM, STM in het Engels) is het mogelijk om de kleinste systemen te bestuderen; zelfs een enkel atoom of molecuul kan worden onderzocht. In de loop der jaren zijn de mogelijkheden van de microscoop flink uitgebreid. Zo is het tegenwoordig mogelijk om de topografische en elektronische structuur te bekijken van doteringmoleculen in halfgeleiders, het verloop van syntheses te bekijken in enkele moleculen en zelfs, handmatig, moleculen één voor één te positioneren met atomaire precisie. In dit proefschrift wordt een drietal verschillende systemen bekeken met de RTM en wordt vooral gekeken naar het effect van een extern magneetveld op deze systemen. Allereerst wordt gekeken naar de elektronische eigenschappen van bismut selenide (Bi_2Se_3) nanoplaatjes. Als tweede worden ronde en rechthoekige artificiële atomen gecreëerd door handmatig ronde en rechthoekige koralen te bouwen uit enkele koolstofmonoxide moleculen. Vervolgens worden de elektronische karakteristieken van deze gebouwde structuren bekeken met en zonder extern aangelegd magneetveld. In het laatste project wordt gekeken naar individuele doteringsatomen in een halfgeleider, hun potentie om artificiële structuren mee te bouwen, hun elektronische karaktereigenschappen en de geleiding door de gedoteerde halfgeleider onder invloed van een magneetveld.

Rastertunnelmicroscoop

Het woord microscoop komt vanuit de Griekse woorden mikros (klein) en skopein (bekijken). Veelal wordt de associatie gelegd met de vroegere biologie lessen waarbij optische microscopen worden gebruikt om te kijken naar cellen en ander organisch materiaal. De rastertunnelmicroscoop geeft de woorden mikros en skopein een nieuwe dimensie. Om te beginnen gebruikt een RTM geen licht om te "kijken" naar kleine systemen. Er wordt gebruikt gemaakt van een atomair scherpe naald, deze naald wordt dichtbij (ongeveer 0.000000001 meter) een geleidend oppervlak gebracht. Door het aanleggen van een spanning op de naald kunnen elektronen tunnelen tussen de naald en het oppervlak en ontstaat een tunnelstroom die exponentieel afhangt van de afstand. Klassiek gezien zou dit niet mogelijk zijn, echter is dit een kwantummechanisch fenomeen genaamd "elektron tunnelen". Door de naald over het oppervlak te bewegen kunnen hoogteverschillen van enkele picometers worden gedetecteerd als een verandering van de tunnelstroom. Atomen zijn gemiddeld 100 picometer in diameter dus is het mogelijk om te "voelen"/"bekijken" waar individuele atomen zich bevinden op een oppervlak. Zelfs atomen in het oppervlak kunnen zichtbaar worden gemaakt met deze techniek. In figuur 7.2a is een oppervlakte te zien van lood waarbij de loodatomen geordend zijn in een mooi kristal oppervlak, de lood atomen zijn te zien als gele bolletjes. Aan de rechterkant is een lagere intensiteit waar te nemen en dit komt omdat hier een atomaire stap naar "beneden" wordt genomen.

Een tweede functie van de RTM is de elektronische eigenschappen bepalen van de (atomaire) locatie direct onder de naald. Door de naald stil te zetten boven een bepaalde locatie en de spanning te variëren is het mogelijk om te bepalen waar er zich energietoestanden bevinden waarbij elektronen makkelijker van de tip naar het oppervlak kunnen 'springen', dit springen van de elektronen tussen de naald en het oppervlak heet tunnelen. Door de geleiding te bekijken als functie van het aangelegde voltage kan een grafiek worden gemaakt van de energietoestanden, deze techniek heet spectroscopie. De combinatie van het kunnen bekijken en vervolgens vastleggen van de elektronische eigenschappen van atomair kleine systemen is een zeer waardevolle techniek voor de wetenschap. Deze techniek is gebruikt voor drie verschillende systemen in deze thesis van enkele atomen in een halfgeleider tot nanoplaatjes gesynthetiseerd in het laboratorium met een dikte van enkele nanometers. Voor het grootste gedeelte van de projecten wordt gekeken naar de uitwerking van een extern magneet veld op de verschillende systemen.

De hoogte van de RTM naald ten opzichte van het oppervlak kan ook gebruikt worden om wetenschappelijke informatie te vergaren. Het is bijvoorbeeld, mogelijk om de naald te gebruiken om individuele atomen te verplaatsen met atomaire precisie. Normaal gesproken is de naald te ver verwijderd van het oppervlak om invloed uit te oefenen op de atomen op het oppervlak. Echter door de afstand te verkleinen kan de naald de atomen wegdrukken of wegtrekken over het oppervlak, deze techniek is genaamd, atomaire manipulatie. Dit kan gebruikt worden om structuren te bouwen op het oppervlak en zodoende onderzoek te doen naar verschillende fysische eigenschappen. Onderzoekers van IBM hebben echter laten zien dat atomaire manipulatie ook gebruikt kan worden als ludieke advertentie met een "stop-motion" video genaamd "a boy and his atom". De hoogte van de naald kan zelf ook een informatie bevatten over de geleiding van het oppervlak. Als het tunnelen van de elektronen tussen het oppervlak en de naald makkelijker gaat dan zal de naald zich terugtrekken. Al deze verschillende technieken zijn gebruikt in de verschillende projecten beschreven in deze thesis en zullen hieronder beschreven worden.

In **hoofdstuk 3** worden de energietoestanden bekeken van Bismut Selenide (Bi_2Se_3) nanoplaatjes d.m.v de RTM. De nanoplaatjes zijn gesynthetiseerd in het lab op zo'n manier dat ze slechts een paar nanometer dik zijn. Het is namelijk bewezen dat de toestanden op de boven en onderkant van het nanoplaatje elkaar opheffen als het plaatje dun genoeg is. Door de locatie specifieke technieken te gebruiken in de RTM kunnen we laten zien dat er inderdaad slechts een enkele toestand aan de rand blijft bestaan in een beperkt energiegebied. In figuur 7.2b is te zien hoe deze geleidende toestand aan de rand zichtbaar gemaakt kan worden als een ring met verhoogde intensiteit langs de gehele rand. Twee verschillende theoretische modellen zijn vervolgens gebruikt om de experimentele bevindingen te verklaren.

Ch. 7
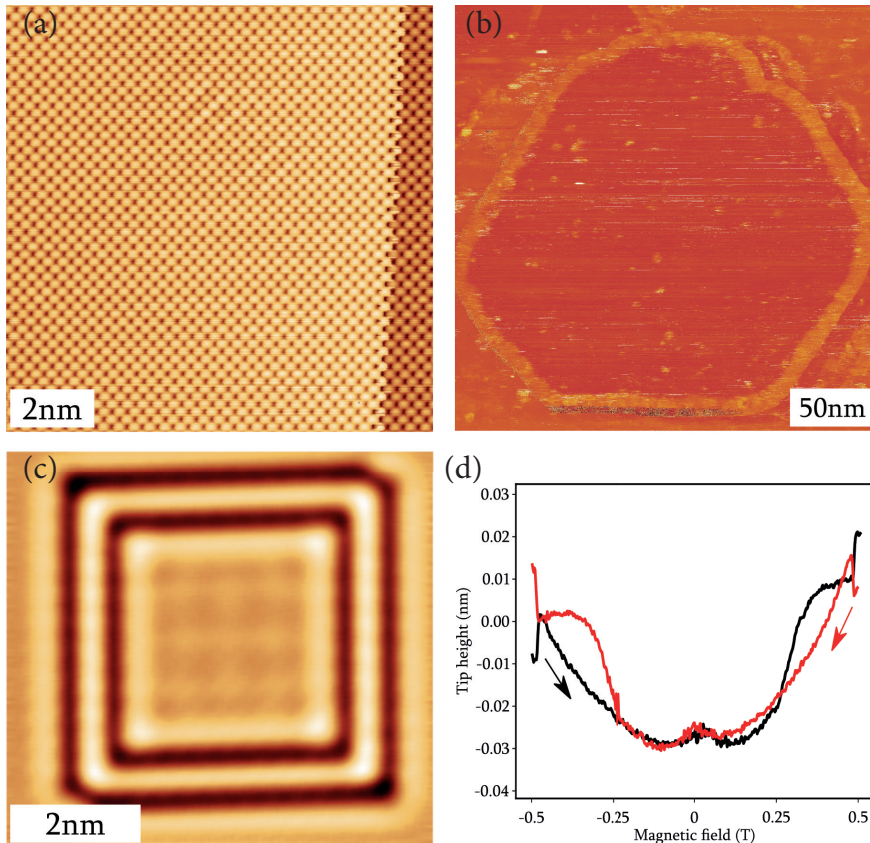
Figuur 7.2:

(a) Een RTM plaatje van een atomair plat oppervlak van lood. De individuele atomen zijn te zien netjes geordend als gele puntjes in het rooster. Aan de rechterkant een verlaging van de intensiteit is te zien wat een stap naar beneden betekend in het kristal. **(b)** Een RTM meting bij een specifieke energie waar de randtoestand van een Bi_2Se_3 nanoplaatje te zien is over de hele rand van het plaatje. **(c)** Een vierkante kwantum koraal gebouwd van koolstofmonoxide moleculen (zwart) op een koper kristal (geel). **(d)** Twee tip hoogte metingen tijdens het veranderen van een extern magneetveld. De richting van de verandering in het veld is te zien als rode en zwarte pijl.

De robuustheid van deze toestand aan de randen van de Bi_2Se_3 nanoplaatjes is verder onderzocht in **hoofdstuk 4**. Door nanoplaatjes met defecten en structurele instabiliteit te bekijken kunnen we bewijzen dat deze toestand zeer robuust is. Zelfs het aanleggen van een magneetveld van 5 Tesla is niet genoeg om de randtoestand te breken. Als er echter magnetische atomen op het opper-

vlak worden opgedampt kan de toestand wel gebroken worden in verschillende maten.

Hoofdstuk 5 beschrijft het creëren en meten van kwantum koralen door koolstofmonoxide moleculen (CO) te verplaatsten over het koper oppervlak met de RTM naald. Als de CO moleculen gepositioneerd worden in een cirkel of rechthoek kunnen de elektronen van het oppervlak worden opgesloten en dit kan worden vergeleken met een artificieel atoom, een rechthoekig kwantum koraal is te zien in figuur 7.2c. De artificiële atomen worden dan blootgesteld aan een magneetveld om onderzoek te doen naar de opsplitsing van de energietoestanden van het artificieel atoom. Theoretisch is bewezen dat er splitsing in de energietoestanden door het Zeeman effect (werkende op de spin van de elektronen) en de Lorentz kracht (een zijdelingse kracht). Experimenteel waren de effecten te klein om deze theorieën te bevestigen.

Het laatste project is beschreven in **hoofdstuk 6** van deze thesis en richt zich op dotering atomen in een halfgeleider, Gallium Arsenide (GaAs). We kunnen met de RTM de elektronische eigenschappen van deze dotering atomen bekijken. Ook kijken we of het mogelijk is om deze atomen te gebruiken voor het bouwen van artificiële structuren zoals gebruikt in hoofdstuk 5. Als laatste wordt gekeken naar waarschijnlijkheid van het tunnelen van elektronen door de hoogte van de naald onder invloed van een extern magneetveld te onderzoeken. Vooral het laatste deel van dit hoofdstuk laat een onverwacht resultaat zien. Zoals te zien is in figuur 7.2d gedraagt de RTM naald zich anders afhankelijk van de richting van de verandering van het magneetveld. Dit resultaat kon echter niet worden verklaart met de kennis opgedaan tijdens dit project en dit laat zien hoe er altijd wetenschappelijke vragen zullen blijven om te beantwoorden.

Ch. 7

Maialalalalen, not only do you have the most musical name I have ever come across, but you also brought a lot of new insight into our research. You have a knack for asking excellent questions which makes you think differently about things, and this really has helped me to dive deeper into science.

Maaike, er is bijna geen enkel onderwerp te bedenken waar we het niet over hebben gehad. Jouw input hebben mijn tijd bij cmi en mijn thesis heel veel beter gemaakt. Helaas werk jij aan andere onderwerpen dus de rest van je dankwoord is out of scope van deze thesis.

Raimonkey, I have said it before but without you I would not be able to climb half the boulders I do now. Your way of giving feedback, as well as your ability to absorb feedback is truly inspiring. I try to learn from this in my professional career as well as my sporting life as much as possible. Let's keep climbing and playing board games together and I hope you can show me around Spain someday.

Jara, ik ben ontzettend trots op onze prachtige hoofdstukken over de nanoplatelets, dit is voor mij waarom ik een PhD wilde doen en zonder jouw kwaliteiten als scheikundige en wetenschapster was dit niet gelukt. Verder is het gelukkig niet alleen bij een collegiale samenwerking gebleven maar ben je een waardevolle vriendin geworden met als (voorlopige) hoogtepunten het spelen van Feed the Kraken en het bekijken van Les Mis in Carré.

Jurretje, het begon allemaal vele jaren geleden bij natuurkunde op de UU. Ondanks dat deze studie ons beide niet gelukkig gezind bleek hebben we via een omweg onze wetenschappelijke carrière toch nog samen kunnen vormgeven bij CMI. Het was altijd fijn om even binnen te lopen bij je en de zaken rond CMI te bespreken en ik weet zeker dat je een uiterst succesvolle verdediging tegemoet gaat binnenkort.

Real **Thomas**, mijn mentor en collega. Jij hebt me tijdens mijn master thesis alles geleerd over STMs en onderzoek doen op de atomaire schaal. Daarna hebben we samen de Gauss, al dan niet vrijwillig, uitgeplozen en dit heeft ertoe geleid dat mijn interesse in de technische kant van de wetenschap is begonnen. Niet alleen hiervoor en al je begeleiding wil ik je hartelijk bedanken maar ook voor je steun tijdens mijn eerste jaren van mijn wetenschappelijke carrière, want het was niet altijd even makkelijk.

Christiaan, het maakt niet uit of we aan het poolen, boulderen of pokeren zijn, jij zorgt altijd voor dat extra zetje in de rug. Helaas heeft onze meettijd samen op de STM niet de resultaten opgeleverd die we wilden maar de positieve energie die jij tijdens het meten meebracht heb ik sindsdien altijd mee proberen te nemen tijdens elk experiment.

Saoirsé, working together with you in the basement was always amazing. The discussions, the chats, the music, and the laughter. It's something I will never forget, especially during the Covid lockdowns, as we were tasked with maintaining the microscopes. Your smile and our conversations made this difficult period a lot more bearable!

Mister muscleman **Pierre**, we have had many incredible highlights during your time in Team Kelder. Physics@Veldhoven, Gent and of course getting that blasted bolt from the Fermi Ion Pump! Thank you so much for all the games, laughter and discussions about science and life.

Jette, je kwam wat later in je PhD terecht in het kantoor bij mij en Thomas maar vanaf dag 1 was je een fantastische kamergenoot. Je hebt mij veel geleerd van de theorie achter je muffin tin berekeningen en daar wil ik je voor bedanken maar ook vooral voor de gezelligheid op 't Ornstein maar ook in de Bisschoppen samen met Lis, Bouncing Hail en de katten. Met als prachtige eer dat ik je paranimf mocht zijn bij jou verdediging.

Marlou, jouw oneindige honger naar kennis gecombineerd met jouw passie voor lesgeven heeft ervoor gezorgd dat ik ontzettend veel over wetenschap heb geleerd door jou. Dank je wel!

PJ, jij doet alles op je eigen manier en dit heeft mij laten zien hoe belangrijk het is in de wetenschap en in het leven om je eigen plan te durven trekken, hiervoor wil ik je hartelijk bedanken. Maar natuurlijk ook voor de prachtige tour die je me hebt gegeven in en rond jouw San Francisco.

Ella, je was mijn eerste student en samen hebben we veel van de experimenten gedaan die uiteindelijk mijn hoofdstuk 3 zijn geworden. Zonder jou hadden deze meetsessies absoluut minder opgeleverd en ook zeker minder leuk geweest. Onze discussies over de metingen hebben gezorgd dat we alles eruit hebben kunnen halen en uiteindelijk er een mooi paper is gekomen. Heel veel succes met de financiële richting die je bent ingeslagen!

Eva, toen je binnenkwam hadden we veel zin om aan de slag te gaan maar helaas werkten de STMs totaal niet mee. Je hebt deze down time uitstekend gebruikt om een hele sterke theorie sectie te schrijven. Uiteindelijk hebben we in de allerlaatste periode van je thesis toch alle experimenten kunnen doen wat soms betekende tot 's avonds laat meten. Ondanks al deze uitdagingen heb je een hele mooie thesis geschreven en heb ik de resultaten kunnen gebruiken voor H5. Dank je wel voor al je harde werk.

Hester, als Bachelor student was ik maar kort je begeleider maar in die paar maanden heb je een grote invloed gehad op het nanoplatelet project. Je pakte alles erg snel op en was al snel meer een collega dan een student. Ik ben blij dat je bij Jara verder bent gegaan met het project want je bent een uitstekende

wetenschapster.

Judith en Midas, jullie hebben ook aan de NPLs gewerkt en hebben allerlei soorten manieren uitgeprobeerd om de platelets mooi verspreid te krijgen op het substraat. Met als prachtig resultaat een stage die gebruikt kan worden om STM-samples op te spincoaten. Dank jullie wel hiervoor deze heb ik nog vaker gebruikt en zal hopelijk in de toekomst ook nog mooie samples opleveren.

There are so many more colleagues and students that I had the privilege to work with in the past 5 years at **CMI**, too many to acknowledge here. Without all of you my time at CMI wouldn't have been as fantastic as it has been. Thank you all for sharing you passion for science with me and I wish you all the best of luck wherever you will end up. Natuurlijk wil ik vooral ook **Andries** hiervoor bedanken die als groepsleider van CMI een prachtige groep heeft neergezet waar iedereen gelijk is en iedereen de kan krijgt om zichzelf te ontwikkelen tot wetenschapper. **Celso and Zeila**, you both always bring unique and valuable insights to the group meetings. **Machteld**, ondanks dat je pas recentelijk bij CMI bent aangesloten hebben we veel goede gesprekken en discussies gehad. Ik hoop dat iets van jou open, eerlijke, no-nonsense houding op mij is uitgestraald en ik hoop dat je de aankomende jaren prachtige wetenschap zal bedrijven aan de UU.

Niet alleen CMI heeft mijn tijd in 't Ornstein zo mooi gemaakt maar **SCMB** heeft daar ook een grote bijdrage aan geleverd! **Marjolein**, jij bent in korte tijd een zeer goeie vriendin geworden. Ik kan met jou altijd over alles praten en vind het heerlijk om samen met jou te klimmen, bordspellen te doen of naar je handbal wedstrijden te kijken. **Rinske**, ondanks dat ik niet altijd jouw tips kan toepassen op de klimmuur, leer ik ontzettend veel van je tijdens het boulderen en daarnaast maken jouw lach en prachtige zangstem de dag altijd wat vrolijker. **Kelly**, al sinds onze tijd als masterstudenten heb ik het gevoel dat we op dezelfde lijn zitten en elkaar toch altijd verder kunnen helpen. Dank je wel voor onze goede gesprekken en de gezelligheid. **Caro** it's always so nice to start the day with a coffee with you and to discuss about the things happening in your lab. Luckily they are now actually happening and I know you will do great research now that most of the woes are over. **The Ornstein** is host to so many more wonderful people, too many to mention here. Thank you all for making this place my home away from home.

Douwe en Tom, onze samenwerking op jullie gallium arsenide samples was er een van hoge toppen en diepe dalen. De eerste sessie samen was uiterst succesvol. Jullie tartten de wetten van de wereld door met het OV de samples heelhuids naar Utrecht te transporteren. Daarna wisten we te landen en de eerste metingen te doen. Jullie beide hebben me veel geleerd van een kant van STM-onderzoek waar ik niks van af wist. Tom, daarna was het aan ons om het theoretische werk van Michael te bewijzen. Helaas was daar eerst mijn

coronabesmetting waardoor ik jou moest aansturen in een vreemd lab en vervolgens waren er talloze mechanische problemen. Zelfs de uitstekende ideeën en sturing van Paul konden er niet voor zorgen dat we de metingen konden voltooien. Gelukkig hadden we altijd LoL, Magic en muziek om ons erdoor te slaan en ik ben blij dat we er alles aan hebben gedaan om het tot een goed einde te brengen!

Of course, there are a few more people, outside of academia, without whom I would not have been able to achieve this.

Ronald, het begon jaren geleden in de trein naar de UvA en nu sta je als beste vriend naast me in een pinguïnpak. In al die jaren heb je me vaak genoeg door moeilijke periodes heen geholpen, soms met een lach, geregeld met een goeie whisky en heel af en toe met een dansje inclusief stok en top hat. Dank je wel voor alles.

Olya, thank you for always being by my side, thank you for worrying about my PhD in my stead and thank you for improving my life every single day. Our lives have been shaken up quite a few times in the past 6 years but with you next to me, I know it will always be fine. I love you and I am grateful I can share the next chapter in my career and our lives with you.

Niels, ik weet dat ik niet altijd goed over mijn gevoelens praat maar ik ben hou van je en ik ben trots op je. De afgelopen paar jaar zijn niet altijd even makkelijk geweest maar we hebben ons erdoorheen geslagen en dat heeft me kracht gegeven om me ook hier doorheen te slaan. Ik hoop dat de aankomende jaren rustiger zijn zodat we vooral leuke dingen kunnen doen zoals toeren met de motor.

Pap, ondanks dat je niet altijd begreep waar ik mee bezig was voor mijn studie of mijn PhD, je was altijd geïnteresseerd, steunde me volledig en liet zien dat je trots bent op het pad wat ik heb belopen. Dit doet me altijd erg veel. Dank je wel voor alles, ik hou van je.

Mam, dank je wel voor al je steun tijdens mijn studies. Het maakte niet uit of het nu plannen waren om naar Amerika te gaan, meerdere keren van studie te veranderen of een periode naar Denemarken te gaan, jij was er altijd om me te helpen dit te realiseren. Zonder jou had ik dit nooit kunnen halen, ik hou van je, dank je wel!

Curriculum Vitae

Jesper René Moes was born on the 15th of November 1991 in Zaandam (North-Holland, Netherlands). He graduated (VWO) from St. Michael College in 2009. After two unsuccessful attempts studying Physics and Astronomy at the UvA and the UU, he finished his bachelor's degree in Chemistry at Utrecht University, including a bachelor thesis at the Condensed Matter and Interfaces group under supervision of Daniel Vanmaekelbergh and Jaco Geuchies.

In 2016 he started the master: "Nanoscience" at the University of Copenhagen. In 2018 he returned to Utrecht and to the Condensed Matter and Interfaces group to perform the Master's thesis and finish the degree: "Nanomaterial Science". During this thesis the objective was to make a prototype STM, (build by SigmaSurface Science) operational for science. This project was supervised by Ingmar Swart, Daniel Vanmaekelbergh and Thomas Gardenier.

In February 2019 Jesper started as a PhD candidate under supervision of Ingmar Swart and Daniël Vanmaekelbergh on a grant of NWO to conduct scientific research on different topics using the same STM. The main results of the research have been presented at (inter)national conferences and are/will be published in peer-reviewed journals. During the PhD, Jesper was a teaching assistant for the theoretical courses: 'Quantum chemistry' and 'Solids and Surfaces' as well as the experimental courses: 'Analyse practicum' and 'Experimental Design'. He supervised one Master student: Eva Stein and four bachelor students: Midas Waakop Reijers, Judith Deen, Hester Noordmans and Ella van Brenk. Lastly during his PhD he followed courses on 'The Art of Scientific Writing' and 'Applied Vacuum Technology'.

Besides his PhD research, Jesper has many interests including: Tennis, Bouldering with friends, listening to music on vinyl, tasting whisky and playing poker with friends.

Ch.
7